Dissertation
submitted to the
Combined Faculties for the Natural Sciences and for Mathematics
of the Ruperto-Carola University of Heidelberg, Germany
for the degree of
Doctor of Natural Sciences

presented by

MSc Mohamed Lotfi Benabderrahmane
born in Mila, Algeria

Oral examination: 18th April, 2007

Measurement of the K^0 Inclusive Cross Section in Pion-Induced Reactions at $1.15\,\mathrm{GeV/c}$

Referees: Prof. Dr. Norbert Herrmann
Prof. Dr. Johanna Stachel

The K^0 production cross section and the phase-space distributions were measured in the reaction π^- + nucleus at an incident momentum of 1.15 GeV/c for C, Al, Cu, Sn and Pb. For the first time the system-size (A) dependence of the K^0 production cross section has been measured and shows an $A^{2/3}$ dependence. The experimental ratio of the K^0 momentum distribution produced in Lead to that in Carbon shows a suppression at low momenta. A comparison to the corresponding ratio of K^+ measured in proton-induced reactions shows a good agreement, which indicates the sensitivity of this observable to the K^0N potential. Comparisons to HSD transport model calculations show that this model is not able to describe momentum and rapidity distributions of the K^0 as well as the behaviour of the inclusive cross section as a function of A. Microscopic calculations of the K^0 cross section in nuclear matter including the KN potential in the final state interaction are in good agreement with the measurements.

Der Wirkungsquerschnitt der K^0-Produktion und dessen Phasenraumverteilungen wurden in π^--Kern-Reaktionen bei einem Pion-Impuls von 1.15 GeV/c für C-, Al-, Cu-, Sn- und Pb-Kerne untersucht. Die Abhängigkeit des K^0-Produktionswirkungsquerschnitts von der Systemgröße A wurde zum ersten Mal gemessen und eine $A^{2/3}$-Abhängigkeit wurde beobachtet. Das experimentell bestimmte Verhältnis der K^0-Impulsverteilungen in Blei zu denen in Kohlenstoff ist für niedrige Impulse stark unterdrückt. Ein Vergleich mit dem entsprechenden Verhältnis für K^+ aus Proton-Kern-Reaktionen zeigt eine gute Übereinstimmung, daher ist diese Observable geeignet zur Untersuchung des KN-Potentials. Vergleiche mit Berechnungen des HSD-Transportmodells verdeutlichen, dass dieses Modell bisher noch nicht in der Lage ist, Impuls- und Rapiditätsverteilungen des K^0, sowie die Abhängigkeit der Inklusiven K^0-Produktion von der Systemgröße zu beschreiben. Berechnungen des K^0-Produktionswirkungsquerschnitts im Rahmen eines mikroskopischen Modells, welches ein KN-Potential für die Wechselwirkungen in Endzustand beeinhaltet, stimmen gut mit den Messergebnissen überein.

Contents

List of Figures

List of Tables

Overview

This thesis presents measurements of neutral kaon production using a pion beam. The measurements were performed in 2004 with the FOPI detector at the GSI facility.

The work is organized in the following way: In chapter one, a general introduction about the physics of heavy-ion collisions and elementary reactions is discussed. An introduction of proton and pion-induced reactions for studying kaon properties in normal nuclear matter is presented, also observables which are sensitive to the in-medium effects are discussed.

Chapter two is describing and explaining the FOPI experimental setup as it was used in the pion-beam experiment. A detailed description of the Central Drift Chamber (CDC) as well as the calibration method are presented.

Techniques used for the event selection and methods for the reconstruction of strange particles are explained in chapter three. In addition, a new method for finding strange particles in the forward part of the FOPI detector is explained.

In chapter four, the evaluation of efficiencies for correcting the measured yields is described. A detailed characterization of the CDC digitizer used in the simulation as well as corrections and the fine tuning of parameters which govern resolutions are outlined.

Chapter five presents the results obtained in this work. Phase-space, yields and production cross section of kaons are discussed. Furthermore, the evaluation of the systematic errors is described.

A comparison to available results from proton-induced reactions is presented in chapter six. For the first time the sensitivity of neutral kaons to the nuclear potential was measured. A comparison of the measured kaon properties with transport model and microscopic calculations are discussed.

The summary of the results and the conclusions are given in the last chapter of the thesis. Future perspectives of experiments with pion beam are discussed there also.

Chapter 1

Introduction

Nuclear matter properties can be investigated using heavy-ion collisions as a tool. Due to high temperatures and pressures, new degrees of freedom are excited. At SIS energies (1-2 GeV per nucleon), mesons like π, K, ρ, ϕ and baryons like Λ^0, Σ, Δ N^* are produced during the collision. According to various model calculations hadron properties might change in such dense and hot phase of the nuclear matter.

Hadron properties can also be investigated by means of elementary reactions (pion-induced, proton-induced and γ-induced reactions). The advantage of elementary reactions is that, hadrons are produced in a well defined state of the nuclear medium: $\rho = \rho_0$ and $T = 0$.

In this chapter, the phase diagram of the nuclear matter and its equation of state is presented. Properties of hadrons produced in heavy-ion and proton-nucleus collisions are explained. At the end, the motivation of using pion-induced reactions is presented.

1.1 Properties of Nuclear Matter

The Nucleon-Nucleon interaction inside a nucleus is attractive at distances of about $1-2\,\mathrm{fm}$ and becomes repulsive at distances below $0.5\,\mathrm{fm}$. As a consequence, most stable nuclei show the same nuclear matter density $\rho_0 \sim 0.17\,fm^{-3}$ ($2.7 \cdot 10^{14}\,\mathrm{g/cm^3}$).

To study properties of nuclear matter and how it will behave under variation of pressure and temperature one needs to know a set of thermodynamic variables (e.g. pressure p, temperature T and density ρ) which characterizes the system. The relation between these variables is described in terms of the equation of state (EOS). The evolution of the system is explained by the variation of the macroscopic variables.

1.1.1 The Phase Diagram

As for ordinary matter, there exists a phase diagram for nuclear matter which describes its various states under different pressure and temperature conditions. The availability of different accelerators running at different beam energies allows to explore different regions of the phase-diagram. The diagram of the state of nuclear matter in the plane of the temperature T and the baryonic chemical potential μ_B is illustrated in figure 1.1 [1, 2, 3]. At moderate beam energies ranging

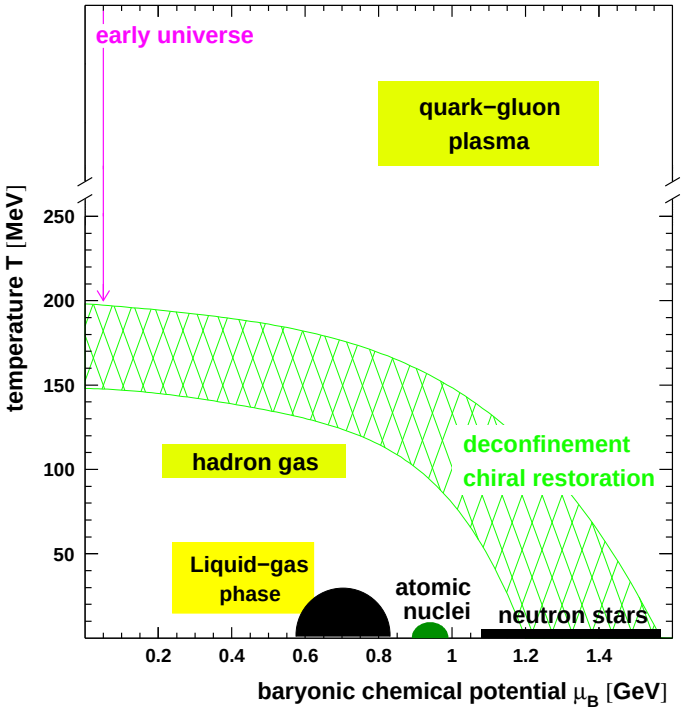

Figure 1.1: Phase diagram in $\mu - T$ plane of strongly interacting matter [1, 2].

from 10 MeV to several hundred MeV per nucleon (the corresponding accelerators at these energy regime are GANIL and UNILAC), the temperature reached in nucleus-nucleus collisions is of the order of a few MeV and densities are below or close to the ground state nuclear matter density $\rho_0 \sim 0.17 fm^{-3}$. In these regions, two phases of nuclear matter coexist, the Fermi liquid and a cold gas of nucleons and light nuclei [4, 5].

The energy regime from 1 GeV up to 10 GeV per nucleon (these energies can be reached at the SIS18 facility (GSI) and the AGS) corresponds to temperatures ranging from 70 MeV to 150 MeV and baryon chemical potentials below 1 GeV. At these temperatures and densities, the nuclear matter is essentially a gas of hadrons: nucleons, pions and hadronic resonances. Theoreticians expect a phase-transition with increasing density towards pion and kaon-condensates [6, 7, 8]. This scenario is expected to happen in compact stars called Neutron Stars, origi-

nating from core collapse of type II supernovae [9].

At energies of 20 GeV per nucleon and above, temperatures above 150 MeV and baryon chemical potentials close to zero are reached using the SPS and RHIC accelerators. A new state of matter is claimed to be created which is the *Quark-Gluon Plasma* [10]. Due to high temperatures, the hadrons are dissolved and their constituent quarks and gluons are deconfined.

1.1.2 The Equation of State (EOS)

One of the motivations of accelerating heavy-ion beams to relativistic energies is to study the properties and behaviour of nuclear matter at densities greater than those that are found in atomic nuclei. At bombarding energies of $1-2\,\mathrm{GeV}$ per nucleon, the densities reached in the fire ball are about 2-3 times normal nuclear matter density. Unfortunately, the fire-ball has a life time of about $10-15\,\mathrm{fm/c}$ ($\sim 10^{-22}$ s) [11]. Thus our observations are limited to the products after the fire ball expansion.

It is questionable whether a thermal equilibrium has been reached or not. Experimentally, it has been demonstrated that a global chemical equilibrium can be excluded [12]. However, a local equilibrium can be present at smaller time scales which allows for a description of the nuclear matter by an equation of state (EOS) [11].

The expression of the EOS is a relation between the energy per baryon E, the temperature T and the density ρ. Usually E can be decomposed into a thermal part E_{th} and a compressional part E_c [11]

$$E(\rho,T) = E_c(\rho,T=0) + E_{th}(\rho,T) + E_0 \quad , \tag{1.1}$$

where E_0 is the binding-energy of infinite nuclear matter $E_0 = E(\rho=\rho_0,\ T=0)$. The nuclear matter has a pressure given by

$$p = -\left(\frac{\partial E}{\partial v}\right)_s = \rho^2 \left(\frac{\partial E}{\partial \rho}\right)_s \quad , \tag{1.2}$$

where v and s are the volume and the entropy per nucleon respectively. The equation of state of infinite nuclear matter is characterized by three fundamental constraints:

1. The condition of stability for ordinary nuclei (i.e. E should have a minimum at $\rho=\rho_0$).

2. At this minimum the Bethe-Weizsäcker binding energy E_0 in the absence of coulomb interaction is about $-16\,\mathrm{MeV}$.

3. The incompressibility κ is defined as follows

$$\kappa = 9\rho_0^2 \left(\frac{\partial^2 E}{\partial \rho^2} \right)_{\rho=\rho_0} \quad . \tag{1.3}$$

The κ factor measures the incompressibility of the nuclear matter. If κ is low ($\kappa \sim 200\,\mathrm{MeV}$), the EOS is called "soft" because one needs relatively small energies to reach higher densities. If κ is high ($\kappa \geq 250\,\mathrm{MeV}$) EOS "hard", because higher compressional energies are needed to reach the same densities.

The main unknown in the EOS is the actual value of κ. Frequency measurements of Giant Monopole Resonance (GMR) show that κ is in the range $200 - 300\,\mathrm{MeV}$ [13, 14]. However, in these measurements the change in nuclear density is less than 10%. Clearly, it is very far away from what can be obtained in heavy-ion collisions. Therfore, extrapolating the EOS to higher densities is not straight forward.

At densities more than twice the nuclear matter density, where full equilibrium is not achieved, the resulting pressure (which is translated into driving force for the observed flow of particles) influences the motion of particles and thus can be related directly to the EOS in terms of model comparisons [11, 15, 16].
Based on measurements of transverse and elliptic flow at AGS energies ($1-2\,\mathrm{GeV}$ per nucleon in Au+Au collisions at densities of $2-5\,\rho_0$), Danielewicz et al. [17] demonstrated that there is no single value of κ (i.e. no single EOS) for a simultaneous description of both types of flow. From the transverse flow, a lower limit of $167\,\mathrm{MeV}$ and from the elliptic flow an upper limit of $380\,\mathrm{MeV}$ were derived for κ. Using the elliptic flow of charged particles (Z=1) produced in Au+Au collisions at SIS energies (i.e. between 0.09 and $1.49\,\mathrm{GeV}$ per nucleon) Andronic et al [18] show that the EOS is "soft" with $\kappa = 230$ MeV based on non-equilibrium situation of the nucleus-nucleus collision modeled by Gaitanos et al. [19].

Studies of K^+ production in heavy-ion collisions at energies above the threshold [20] showed that the K^+ have an apparent temperature bigger than the one of protons and pions. The explanation for such an observation was done in terms of the mean free paths of the produced particles [21]. Since particles with a long mean free path would escape more easily from the system, they would reflect the earlier hot stage of the collision [22].
Aichelin and Ko [23] had the idea to propose subthreshold K^+ production as probe for the EOS. Using BUU (Boltzmann-Uheling-Uhlenbeck) calculations, they showed that the production probability of the K^+ assuming a "soft" EOS differs by a factor of three from the one under the assumptions that the EOS is "stiff" at energies below threshold.
Recently, the KaoS collaboration [24] measured the ratio of the K^+ production in Au+Au and C+C collisions at different beam energies near threshold. The

kaon ratio was found to be increasing by a factor of almost three with decreasing beam energy. Recent Quantum Molecular Dynamics calculations [25] (where a repulsive kaon-nucleon potential is taken into account) could reproduce the ratio measured by KaoS if a value of $\kappa = 200$ MeV is assumed.

1.2 Hadrons in Nuclear Matter

The hatched area in figure 1.1 demonstrates the phase-diagram region where the chiral symmetry is expected be restored [26, 27, 28]. Chiral symmetry is a symmetry of QCD in the limit of vanishing quark masses. The symmetry is also expected to be restored at zero temperature once the density of baryons becomes high enough. This may occur in the cores of neutron stars, converting them to quark stars [29].

At low temperatures the QCD running coupling constant α_s becomes large, quarks and gluons interact non-perturbatively and as a result the QCD vacuum acquires a non-trivial structure, the quark and gluon condensate [30].

In the limit of massless quarks (where $m_s = m_u = m_d = 0$), QCD with three flavors has an exact symmetry [31]. It is explicitly broken by the quark mass term in the QCD Lagrangian (where the quarks have their bare masses $(m_u + m_d) \sim 12$ MeV and $m_s \sim 150$ MeV [32]). The smallness of $m_{u,d}$ as compared to typical hadron masses, e.g. the nucleon mass $m_N \sim 1$ GeV, suggests that the mass term in the QCD Lagrangian can be treated perturbatively [32]. This is the starting point of chiral perturbation theory.

There is evidence both from low energy hadron phenomenology and from lattice QCD that chiral symmetry is also spontaneously broken [33]. Properties of light hadrons, such as masses and couplings are controlled by chiral symmetry [34, 35]. Non-zero u and d quark masses shift the mass of the Goldstone boson (pion) from zero to its observed value. The connection between m_π and u and d quark masses is given by the Gell-Mann-Oakes-Renner (GOR) relation in lowest order [36]

$$m_\pi^2 = -\frac{1}{f_\pi^2}(m_u + m_d) < \overline{q}q > + O(m_{u,d}^2) \quad , \tag{1.4}$$

here $< \overline{q}q >$ is called the chiral (or quark) condensate and f_π is the pion decay constant which is about 92.4 MeV [37]. It is the result of the spontaneous breaking of the chiral symmetry where its vacuum is not empty but populated by scalar $\overline{q}\,q$ pairs. The corresponding ground state expectation value is $< 0|\overline{\psi}\psi|0 > \equiv < \overline{q}q >$. A QCD phase transition from hadron matter to quark matter at high temperature corresponds to vanishing value of $< \overline{q}q >$. Therefore, this condensate is an order parameter of the spontaneous chiral symmetry breaking. It is of great importance to know the behaviour of the $< \overline{q}q >$ under different pressures and temperatures

of nuclear matter. Assuming a homogeneous medium where the relevant degrees of freedom are hadrons, the derivative of the pressure p (pressure of the medium related to the partition function Z) with respect to a quark mass, produces the in-medium $\overline{q}q$ condensate [38]. The thermal expectation of value $<\overline{q}q>_{T,\rho}$ is given by

$$\frac{<\overline{q}q>_{T,\rho}}{<\overline{q}q>_0} = 1 + \frac{1}{f_\pi^2}\frac{dp(T,\mu)}{dm_\pi^2} \quad , \tag{1.5}$$

where $<\overline{q}q>_0$ is the quark condensate at $T=0$ and $\rho=0$, and has a value of $-(240\ MeV)^3$. $p(T,\mu)$ is the pressure for a given temperature T and baryonic chemical potential μ. The results of the calculation of $<\overline{q}q>_{T,\rho}$ in (1.5) is shown in figure 1.2.

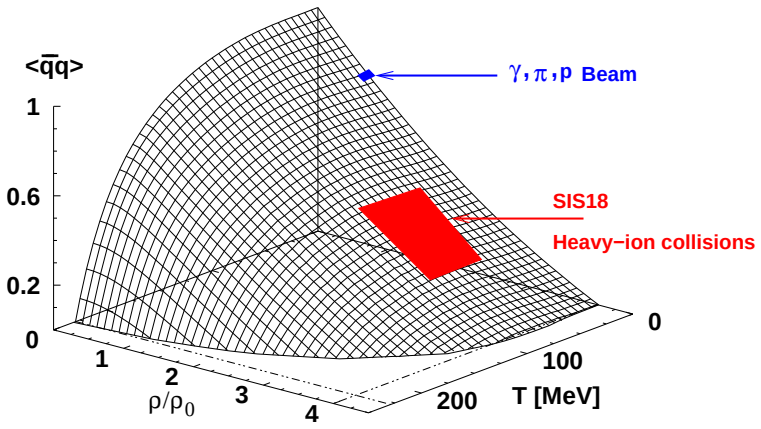

Figure 1.2: Behaviour of the quark condensate $<\overline{q}q>_{T,\rho}$ normalized to $<\overline{q}q>_0$ as a function of temperature T and density ρ [38].

Densities of 2-3ρ_0 and temperatures of $70-150$ MeV are reached in heavy-ion collisions at energies $1-2$ GeV per nucleon. The magnitude of $<\overline{q}q>$ at these energies can be reduced by 80% roughly. However, at normal nuclear matter density the $<\overline{q}q>$ magnitude is expected to be already reduced by about 30% [38, 28] with respect to its vacuum value.
Since the pion is a Goldstone boson, its mass can not change in the nuclear medium, therfore the change of $<\overline{q}q>_{T,\rho}$ is linked to the in-medium pion decay constant f_π^*. At a given temperature T and density ρ, the Gell-Mann-Oakes-Renner relation holds [39] and the in-medium f_π^* is given by

$$f_\pi^*(T,\rho)^2 \cdot m_\pi^*(T,\rho)^2 = -(m_u+m_d)\cdot <\overline{u}u>_{T,\rho} + \ldots \quad , \tag{1.6}$$

under the assumption that $<\overline{u}u> = <\overline{d}d>$ (the asterisk denotes the observables inside the nuclear medium). Suzuki et al. [40] measured the $f_\pi(\rho)^2/f_\pi^2$ ratio using

deeply bound 1s states of π^- in Sn. They investigated the iso-vector parameter of the s-wave pion-nucleus potential. The comparison the potential of πN scattering. gives a value of 0.64 for the $f_\pi(\rho)^2/f_\pi^2$ ratio. This is a clear evidence for the partial restoration of chiral symmetry probed at normal nuclear matter density.

The kaon masses are somewhat higher than the pion mass. Thus those particles are further away from being approximate Goldstone bosons [34, 28]. Effects of the explicit chiral symmetry breaking are considerably bigger since their mass is already half of the nucleon mass (i.e. the nucleon mass is used at low energy as a mass scale). Kaons carry strangeness, their behaviour in non-strange symmetric nuclear matter differs from that of the pion. Nevertheless, its mass in the vacuum is related to the quark condensate via the GOR formula

$$m_K^2 = -\frac{m_u + m_s}{2 f_K^2} < \bar{u}u + \bar{s}s > + O(m_s^2) \quad , \tag{1.7}$$

and it vanishes in the limit of exact chiral symmetry ($m_q \to 0$). The constant f_K is the pseudo-scalar decay constant ($f_K \sim 114$ MeV).

Kaplan and Nelson [8] used an effective chiral Lagrangian to show the possibility of charged kaon condensation which may occur at densities around 2-3 times normal nuclear matter density. They conclude, that the strongly attractive interaction between kaons and baryons causes the effective kaon mass to drop in dense baryonic matter. This work triggered ideas of studying kaon properties in baryonic matter from both sides, experimentally and theoretically.

At SIS energies, kaons are produced close to or even below the threshold. The threshold energy needed for K^+ production in a NN collision is about 1.58 GeV ($NN \to K^+\Lambda N$) and about 2.49 GeV for the K^- ($NN \to K^+K^-NN$), respectively.

The production of kaons at subthreshold energies in heavy-ion collisions is influenced by the surrounding nuclear medium . Medium effects on the kaon production mechanism include [41]:

1. The Fermi momentum of nucleons. It adds to the incident momentum of the projectile nucleons and increases the available energy for kaon production.

2. Two-step processes like the excitation of a nucleon to a resonance and the subsequent production of kaons via the interaction of the resonance with other baryons ($\Delta N \to K^+\Lambda N$ or $N^*N \to K^+\Lambda N$).

3. The medium modification of kaon properties, i.e. the K-N potential which has two terms, an attractive scalar potential (for both K^-N and K^+N interactions) and a repulsive vector potential for K^+N and an attractive for K^-N [31].

Consequently, the K^- feel a strong attractive potential, whereas the K^+ feel a weakly repulsive one. Figure 1.3 sketches the effective mass of K^+ and K^- as a function of the nuclear density. Due to the effect of the potential, the K^- effective mass drops by roughly 25% at $\rho \sim \rho_0$ and the K^+ effective mass increases by about 10% at $\rho \sim \rho_0$.

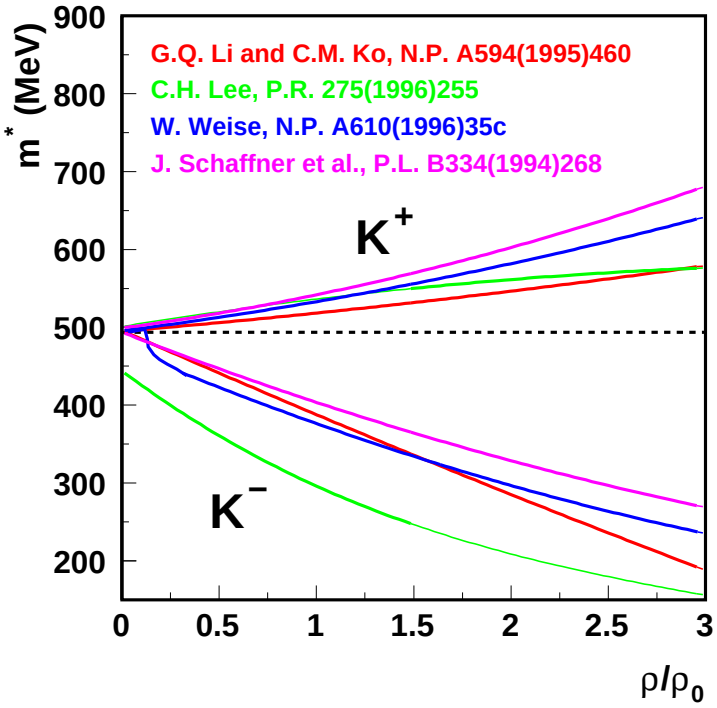

Figure 1.3: The effective mass of kaons and antikaons as function of the nuclear density obtained from different theoretical calculations.

Experimentally it is still a challenge to understand the behaviour of kaons in nuclear medium. There are two ways to explore the kaon properties, using either heavy-ion collisions or elementary reactions.

1.3 Kaon Properties in Heavy-Ion Collisions

The K^+ production rate (i.e. cross section) was measured as a function of the centrality in the Au+Au system at 1 AGeV by the KaoS collaboration [42, 43]. Figure 1.4 shows the number of K^+ (in red) and π^+ (in blue) normalized to the number of participants (A_{part}) as a function of (A_{part}) (A_{part} is the number of

nucleons in the overlay region of the colliding nuclei). In this representation, the production rate of π^+ is constant as function of the centrality whereas the rate M/A_{part} for the K^+ increases. It has an $(A_{part})^{\alpha}$ dependence where $\alpha \sim 1.8$ [43]. This dependence can be explained as follows: It is possible to produce a Δ or N^* resonance ($NN \rightarrow \Delta(N^*)N$) in NN reactions which acts as an energy reservoir and lowers the threshold for the creation of the K^+ via $N\Delta \rightarrow NYK^+$ or $\pi\Delta \rightarrow YK^+$ (Y=Σ, Λ). If the probability of each step is roughly proportional to A_{part}, the

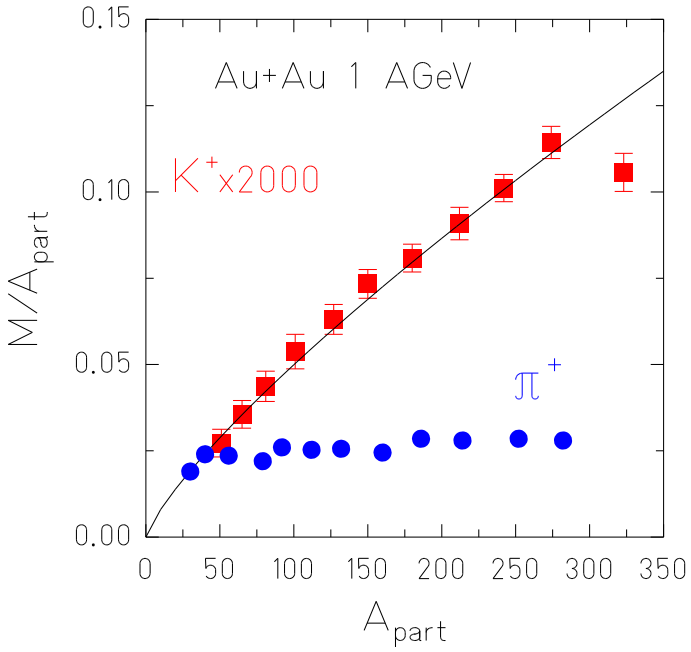

Figure 1.4: Multiplicity of K^+ and π^+ per participating nucleon as a function of A_{part} for Au+Au collisions at 1 AGeV [42, 43]. The line corresponds to a parameterization according to $M \propto (A_{part})^{1.8}$.

probability for both process to happen in a cascade will be proportional to A^2_{part}. This is considered as an evidence for a multi-step process responsible for K^+ production below the threshold.

According to the fact that the $K^-(K^+)$ effective mass drops (rises) inside nuclear matter, the K^-/K^+ ratio is a sensitive quantity for in-medium effects. The KaoS collaboration has measured the multiplicity of K^+ and K^- in C+C and Ni+Ni reactions at different energies. Figure 1.5 [43, 44, 45] shows the multiplicity of K^+ and K^- per average number of participating nucleons as function of the energy above threshold (i.e. defined as the Q-value, where $Q = \sqrt{s} - \sqrt{s_{th}}$) in the NN system. The full and dashed lines are calculations for proton-proton collisions [46, 47]. At the same Q value, the yield of K^+ exceeds the K^- yield by

1-2 orders of magnitudes. In contrast to proton-proton collisions, the K^- and K^+ multiplicities in nucleus-nucleus collisions are nearly the same. This measurement demonstrates that compared to NN reactions the K^- production yield grows much stronger than the one of K^+.

Hartnack et al. [48] performed calculations in order to explain those measurements. They showed that in A+A collisions almost all K^- are produced via the pionic channel $\pi^-\Lambda \rightarrow K^-N$ which is not available in proton-proton collisions. Because the Λ is produced simultaneously with the K^+, the K^- and K^+ pro-

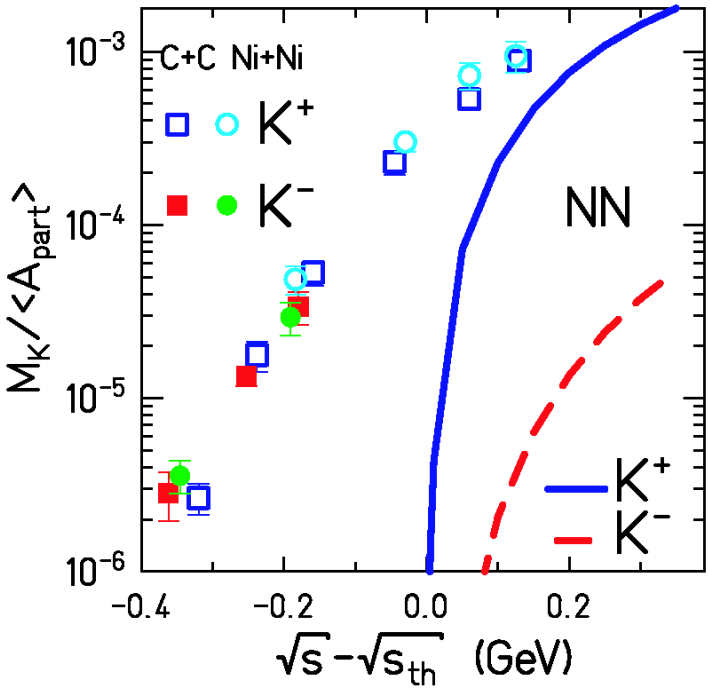

Figure 1.5: Scaled K^+ (open symbols in blue) and K^- (full symbols in green and red) multiplicity as a function of the Q-value calculated with the free masses [44, 45, 43]. Open symbols (closed symbols) represent multiplicity of K^+ (K^-) in C+C and Ni+Ni systems. The solid and dashed lines correspond to model calculations of K^+ and K^- multiplicities in NN collisions.

duction yields are strongly correlated. The final K^- yield depends on the K^+N potential but does not depend on the K^-N potential because the observed K^- are produced at very late stage of the reaction at low densities where K^-N potential is small [48].

At SIS energies the kaon flow is suggested to be a sensitive observable to the KN potential. Based on relativistic transport calculations, Li and al. [49] showed that under different assumptions for the KN potential, the slope of the sideward

flow at mid-rapidity shows a different behaviour. The FOPI collaboration investigated the K^+ flow pattern in the Ni+Ni (1.93 GeV per nucleon) and Ru+Ru (1.69 GeV per nucleon) systems [50, 51]. Figure 1.6 shows the measurement of the proton and K^+ sideward flow v_1 (where $v_1 = < p_x/p_t >$) as function of transverse momentum p_t around target rapidity. For all p_t, protons have a negative v_1 while the K^+ show a positive v_1 for low p_t, at high p_t v_1 vanishes or can be negative. The dashed line is a result of an RBUU calculations [46, 52], obviously the model without in-medium K^+ potential fails to describe data. If a KN potential strength of 20 MeV is included in the model, a quantitative agreement between data and model can be seen. The repulsive nature of kaon with respect to nucleon tends to push the K^+ away, thus resulting in anti-correlation between the K^+ and proton flow.

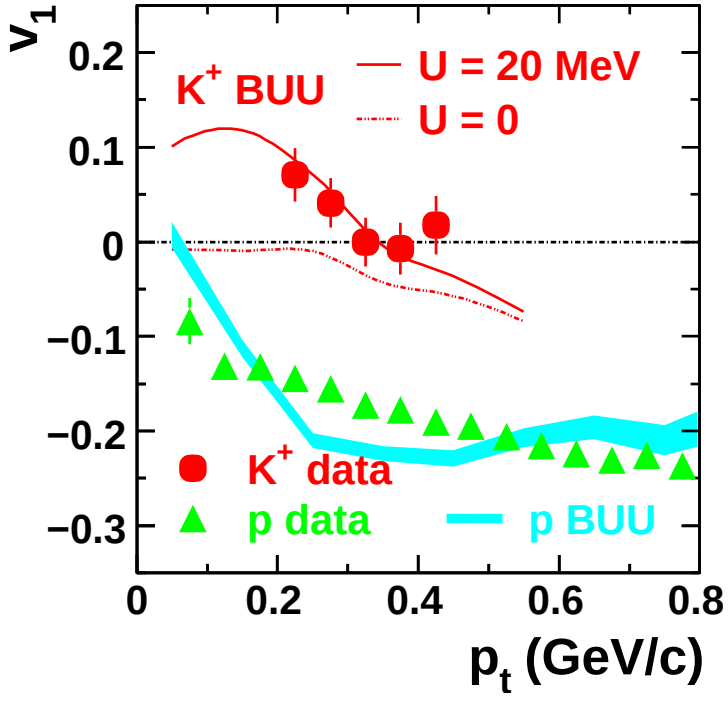

Figure 1.6: Transverse momentum dependence of the sideward flow of K^+ (circles) and protons (triangles) measured in Ni+Ni at 1.93 AGeV in the rapidity range $-1.2 < y^{(0)} < -0.65$ [50]. The shaded area is an RBUU prediction for protons. The lines, are model predictions for different K^+N potentials.

The KaoS collaboration also investigated the flow to study its sensitivity with respect to the K^+N potential [53]. They measured the elliptic flow v_2 (where $v_2 = < (p_x^2 - p_y^2) \ / \ (p_t^2) >$) of K^+ at mid-rapidity in Au+Au system at 1 AGeV. Figure 1.7 illustrates a preferentially perpendicular emission of K^+ with respect to

the reaction plane, this trend is well described by RBUU [54] only if the potential is taken into account which has approximately a value of 20 MeV.

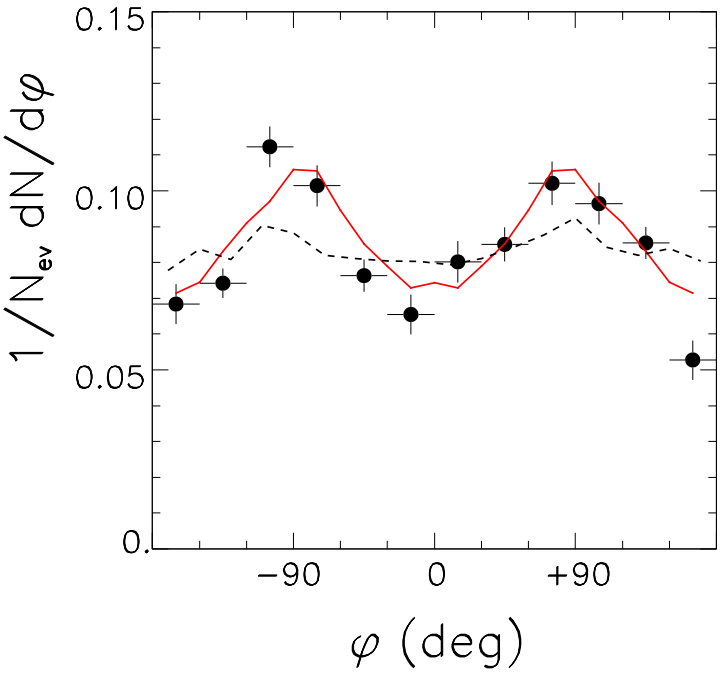

Figure 1.7: Azimuthal distribution of the K^+ measured in Ni+Ni reactions at 1.93 AGeV at rapidities $0.4 < y/y_{proj} < 0.6$ [53]. The lines represent results of RBUU calculations. Dashed lines: without in-medium KN potential. Solid lines: with in-medium KN potential.

1.4 Kaon Production in proton-induced Reactions

As it was mentioned before, the KN potentials depend on the nuclear density, which varies strongly with the time evolution of the nucleus-nucleus reaction. It is possible to avoid such a complication by producing kaons in proton-induced reactions where the nuclear density of the medium is well defined. Kaons produced below the threshold for the free NN collisions are a good probe for studying multi-step processes and cooperative effects of the nucleons inside the target nucleus. Koptev et al. [55] measured total inclusive K^+ cross sections ($p+A \rightarrow K^+ + X$) for targets between Be and Pb and proton energies from 0.8 to 1. GeV. Those results were discussed in terms of different models [56, 57, 58] where it was concluded that

- the K^+ production in a first collision of the incident proton with the nucleon is negligible at incident energies below 1 GeV.

- the two-step reaction mechanism with K^+-production in the collision of secondary pions ($p + N \rightarrow \pi + X$) with the nucleons ($\pi + N \rightarrow K^+ + Y$) dominates at subthreshold energies.

The set of data collected in [55] did not show any evidence for cooperative phenomena, therefore additional experimental data were needed for an unambiguous determination of the reaction mechanism.

At Saturne, Debowski et al. [59] measured double differential K^+ cross sections in $p+C$ and $p+Pb$ collisions at 1.2, 1.5 and 2.5 GeV. Below threshold, based on the binary collision model, these data show an evidence for two-step processes dominance.

At ANKE, Koptev et al. [60] measured double differential cross sections for K^+ production in $p+C$ interactions at a projectile energy of 1 GeV and polar angles $\theta \leq 12^\circ$. To explain the K^+ invariant cross section, a high degree of collectivity is needed in the target nucleus. Alternatively, high intrinsic momenta of the participating target nucleons are required to supply the missing energy for subthreshold kaon production [60]. The K^+ invariant cross section ($p + (lN) \rightarrow (lN) + \Lambda + K^+$, l is the number of target nucleons involved in the K^+ production) was described within a phase-space approximation. These data show that kaon production at an incident energy of 1 GeV can be understood only in terms of cooperative effects with the effective number of nucleons involved in the interaction being $\simeq 5-6$. Such cooperative effects have been explained [57, 58, 61] in terms of multi-step mechanisms or high momentum components in the nuclear wave function.

Nekipelov et al. [62] measured the ratio R(Au/C) of the kaon (K^+) production cross section for a given momentum at a proton incident energies of 2.3, 1.75 and 1.5 GeV. Figure 1.8 shows the measured ratio R(Au/C) at proton energy of 2.3 GeV. The data points show a rising ratio for decreasing K^+ momenta passing a maximum at 245 MeV/c and falling steeply at low momenta. This shape has also been observed for the other two incident energies (1.75 and 1.5 GeV), which indicates that the suppression of the ratio R(Au/C) at low K^+ momentum is largely independent of the beam energy. This observation suggests that the phenomenon is principally due to the interaction of the K^+ with the residual nucleus [62]. The full line in figure 1.8 represents a model calculation based on a coupled channel transport model [63, 52] where Coulomb and nuclear potentials are included as hadron rescattering effects. The position of the maximum of R(Au/C) can be reproduced as in data if a value of the kaon potential of 20 MeV is used in the model.

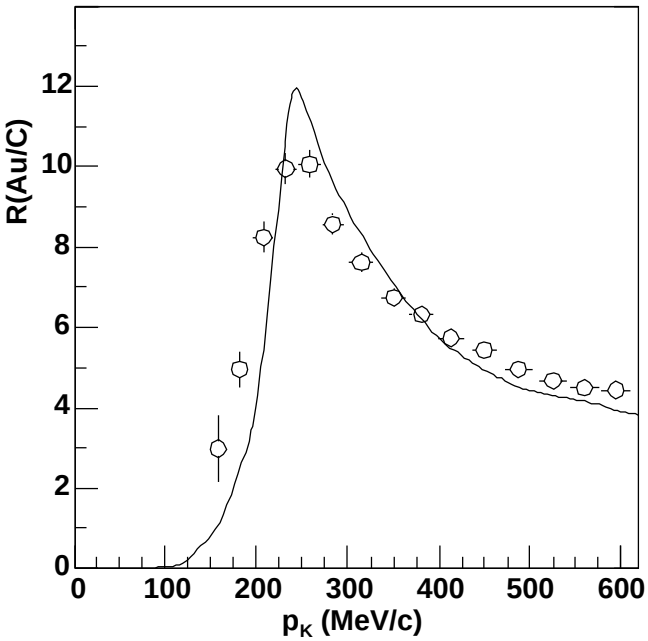

Figure 1.8: Ratio of the K^+ production cross section between Au and C at a proton energy of 2.3 GeV as a function of the kaon momentum [62]. The line shows the result of transport calculations taking into account Coulomb interaction and a KN nuclear potential of 20 MeV.

1.5 Kaon Production in pion-induced Reactions

In heavy-ion collisions At SIS energies kaons can be produced via multi-step processes, where mainly two channels are involved: $B_1 + B_2 \rightarrow B_3 + Y + K$ (B stands for either a nucleon or the $\Delta(1232)$) and $\pi + N \rightarrow YK$ (Y stands for Σ or Λ). Up to now not many studies have been performed for these elementary processes [64, 65, 66].

To understand kaon production in heavy-ion reactions in terms of cross sections, Tsushima et al [67] investigate the production channel $\pi + N \rightarrow K + Y$ inside the nuclear matter in details. They used the quark-meson coupling (QMC) model [68] to calculate vector and scalar potentials for mesons and baryons in nuclear matter. The resonance model [66, 69] was also used to evaluate the kaon production cross dependence on nuclear density.

Based on the QMC model, effective hadron masses m_h^* and mean-field potentials are calculated self-consistently [67, 70]. The scalar potential (U_S^h) felt by the hadron "h" in nuclear matter is given by

$$U_S^h \equiv U_s = m_h^* - m_h \quad . \tag{1.8}$$

The vector potential U_v^h has a linear dependence on the mean-field potentials as follows

$$U_v^h = (n_q - n_{\bar{q}}) \cdot V_\omega^q - I_3 \cdot V_\rho^q \quad , \tag{1.9}$$

where $n_q(n_{\bar{q}})$ are the lowest mode light quark (antiquark) numbers in the hadron "h". V_ω^q and V_ρ^q are the mean field potentials and I_3 is the third component of

the isospin projection of the hadron "h". This leads to a change in the hadron four momentum from $p_h = \left(\sqrt{\vec{p}^2 + m^2}, \vec{p}\right)$ to $p_h = \left(\sqrt{\vec{p}^2 + m_h^{*2}} + U_v^h, \vec{p}\right)$, which modifies not only kinematical factors (i.e. phase space and threshold) but also the reaction amplitudes [67] (see appendix B).

Resonances like Δ and N^* are assumed to be responsible for the kaon productions in πN reactions on the basis of the resonance model [66, 69, 71, 72]. Tsushima et al. [67] made the assumption that those resonances change their masses in the nuclear medium. The final step of the calculations is to include hadron properties (in the initial, final and intermediate mesonic and baryonic state) in the reaction amplitudes. The final result of this microscopic calcula-

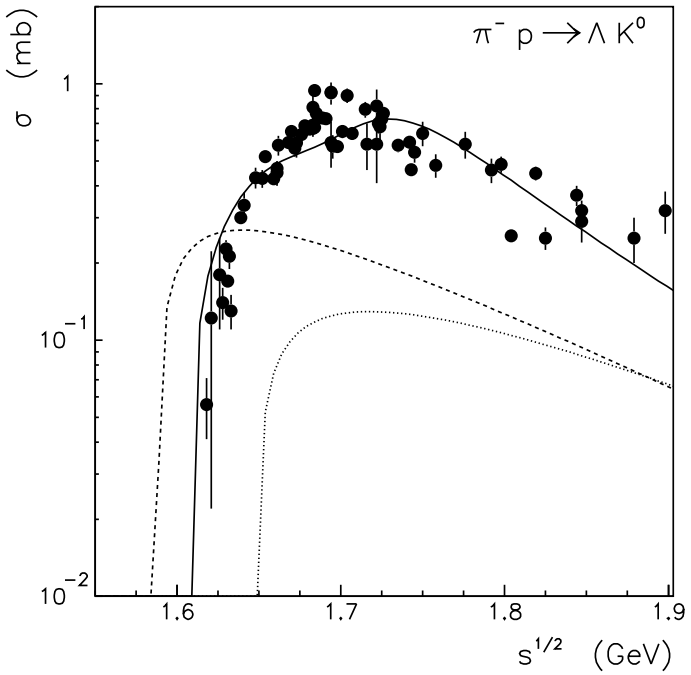

Figure 1.9: The cross section of the reaction $\pi^- + p \rightarrow K^0 + \Lambda$ as a function of the invariant incident energy $\sqrt{s}$ [67]. The circles are data measured in free space adapted from [73]. The line represents model calculations in free space (solid) and for nuclear matter at baryon density $\rho_B = \rho_0$ (dashed) and $\rho_B = 2 \cdot \rho_0$ (dotted).

tion is shown in figure 1.9. It demonstrates variations of the reaction cross section of $\pi^- + p \rightarrow K^0 + \Lambda$ as a function of the invariant collision energy $\sqrt{s}$ for three different densities: Free space $\rho_B = 0$, normal nuclear matter density $\rho_B = \rho_0$ ($\rho_0 = 0.17\ fm^{-3}$) and twice normal nuclear matter density $\rho_B = 2 \cdot \rho_0$. The experimental data points are from $\pi^- p$ reactions which were measured in bubble chambers in the beginning of 1960 [73].

The full line in figure 1.9 is the result of the model obtained in free space. The model calculations show a reasonable agreement with the data for all incident energies (i.e. all $\sqrt{s}$). The dashed line represents the result of the calculation at $\rho_B = \rho_0$. It can be seen that the reaction threshold is shifted downwards with respect to the threshold in free space (i.e. $\sqrt{s} = 1.63$ GeV). The reaction cross

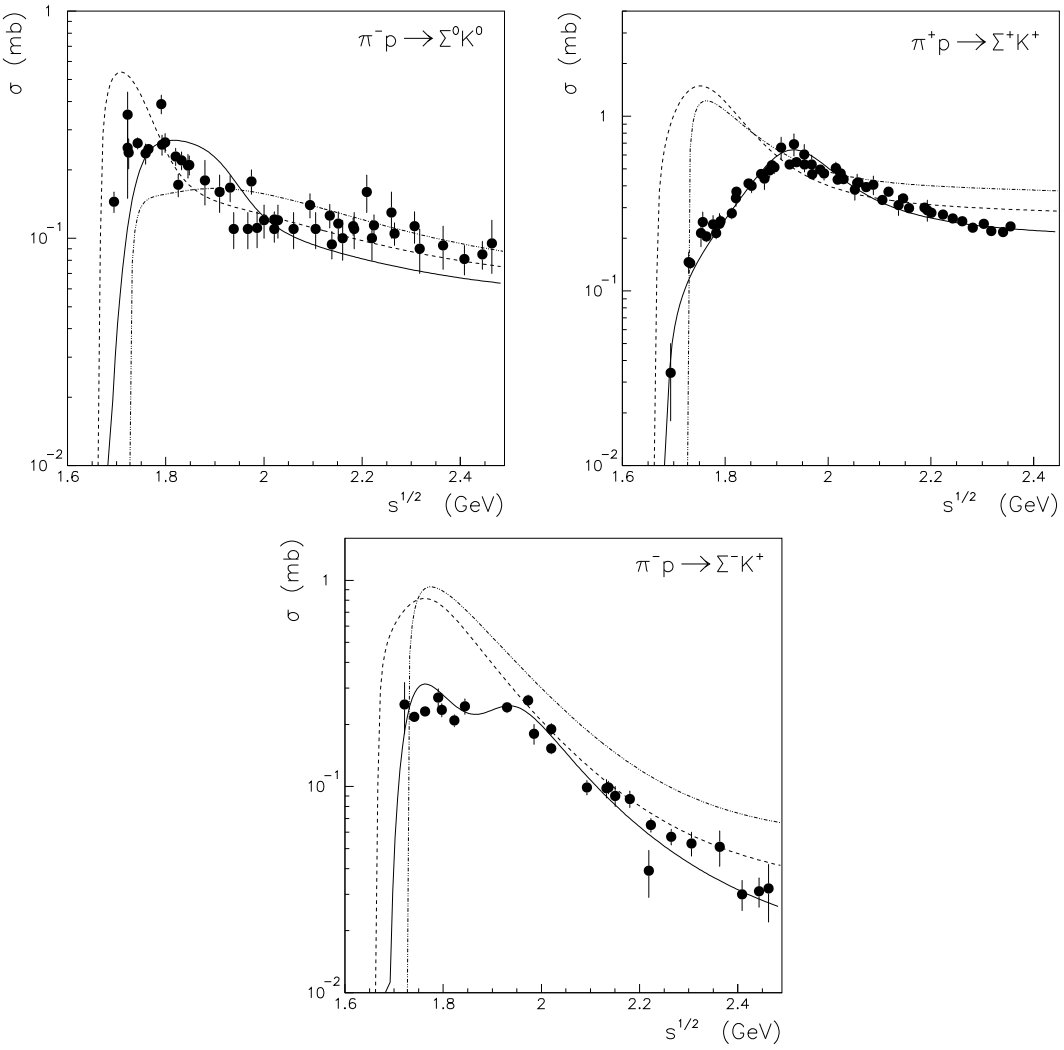

Figure 1.10: Upper left panel: Energy dependence of the total cross section of the $\pi^- + p \to K^0 + \Sigma^0$ reaction as a function of the invariant collision energy $\sqrt{s}$, calculated for different baryon densities. The lines indicate the calculations for free space (solid) and for normal nuclear matter density (dashed) and for $\rho_B = 2 \cdot \rho_0$ (dotted). The Data points were measured in free space. Upper right panel: Energy dependence of the total cross section of $\pi^+ + p \to K^+ + \Sigma^+$ reaction as a function of the invariant collision energy $\sqrt{s}$. Labels in the figure are the same as for the first plot. Lower panel: Energy dependence of the total cross section of $\pi^- + p \to K^+ + \Sigma^-$ reaction as a function of the invariant collision energy $\sqrt{s}$. Labels in the figure are the same as for the first plot. Figures are adapted from [67].

sections in this case is lower than the one obtained at $\rho_B = 0$ by more than a factor 2 at energies below 1.8 GeV. The dotted line is the result obtained at $\rho_B = 2 \cdot \rho_0$.

The reaction threshold is shifted upwards in this case with respect to $\rho_B = 0$ case and the cross section is suppressed by at least a factor 4 for energies up to 1.8 GeV. Other elementary reaction cross sections are evaluated on the basis of this model like $\pi^- + p \rightarrow K^0 + \Sigma^0$, $\pi^+ + p \rightarrow K^+ + \Sigma^+$ (i.e. which is the isospin partner of $\pi^- + n \rightarrow K^0 + \Sigma^-$), and $\pi^- + p \rightarrow K^+ + \Sigma^-$ at $\rho_B = 0$, $\rho_B = \rho_0$, and $\rho_B = 2 \cdot \rho_0$. The upper left panel of figure 1.10 shows the energy dependence of the total cross section of the channel $\pi^- + p \rightarrow K^0 + \Sigma^0$ in comparison to available data in free space. The variations of the cross section as a function of $\sqrt{s}$ from the data are reproduced by the model. At $\rho_B = \rho_0$ the calculation of the cross section shows an enhancement at threshold (i.e. $\sqrt{s} = 1.63$ GeV). At $\sqrt{s} \geq 1.8$ GeV, the cross section is reduced with respect to the one at $\rho_B = 2 \cdot \rho_0$. The same behaviour of the calculated cross section is seen for the isospin partner of the channel $\pi^- + n \rightarrow K^0 + \Sigma^-$ which is shown in the upper right panel of figure 1.10. The measured data are again reproduced nicely by model calculations. For this channel it can be seen that the calculated cross section at $\sqrt{s} \sim 1.63$ GeV and $\rho_B = \rho_0$ is roughly ten times bigger that the measured cross section in free space. The lower left panel of figure 1.10 depicts the energy dependence of the total cross section of $\pi^- + p \rightarrow K^+ + \Sigma^-$. The calculation of the cross section in free space nicely fits to the data.

To be able to measure the K^0 exclusive cross section with a Λ in the final state (i.e. $\pi^- + p \rightarrow K^0 + \Lambda$) at normal nuclear matter density, measurements of K^0 and Λ in coincidence are needed. Since the existing data are only for the case $\rho_B = 0$, the model calculations show a reasonable agreement with the data for all channels [67].

For SIS energies, this is the only microscopic calculation aiming at kaon production cross section calculation in πN reactions at different nuclear matter densities. Up to today, no data on kaon production in πN reactions in nuclear matter exits.

In 2004, for the first time at the GSI facility, a pion beam with a reasonable intensity of 5000 pions per second was provided to the experimental area where the FOPI detector is located. The FOPI collaboration used the pion beam on five different targets (C, Al, Cu, Sn and Pb) at a momentum of 1.15 GeV/c which corresponds to $\sqrt{s} = 1.75$ GeV. The goal of that experiment is to study the kaon production at a well defined nuclear matter density (i.e. $\rho_B = \rho_0$) as function of the system size as well as kaon properties inside nuclear matter. As mentioned above, the production of kaons is influenced by their interaction with the surrounding nucleons. Therfore, measuring their production cross section is a key point for understanding the in-medium kaon properties which are connected to the chiral symmetry of QCD.

Chapter 2

The FOPI Detector and the S273 Experiment

2.1 Introduction

FOPI is a fixed-target heavy ion experiment. The different components of the 4π detector system were assembled at the "Schwerionensynchrotron" SIS at the GSI facility [74]. It has been designed to study the properties of compressed nuclear matter formed by collisions of heavy ions at energies from 0.1 AGeV to 2.0 AGeV. The detector consists of sub-detector systems which nearly have a complete azimuthal symmetry [75] as it is depicted in figure 2.1. This nearly 4π coverage of the solid angle, allows for an almost complete event characterization. FOPI is able to identify light charged particles (pions, kaons, protons ...) [76, 77, 78, 79] and intermediate mass fragments [80]. Hadronic resonances and neutral hadrons can also be reconstructed from their decay products [81, 82, 83, 84, 85, 86].

2.2 The secondary Pion Beam at GSI

To broaden the current research program of the GSI facility in the field of relativistic heavy-ion collisions, a pion beam has been established at the heavy-ion synchrotron SIS [87]. The goal of such beam is to study the hadron properties at normal nuclear matter density. As sketched in figure 2.2, pions can be delivered to all major experimental areas of the SIS target hall. The pion production target is a Beryllium target located in the main beam line coming from the synchrotron.

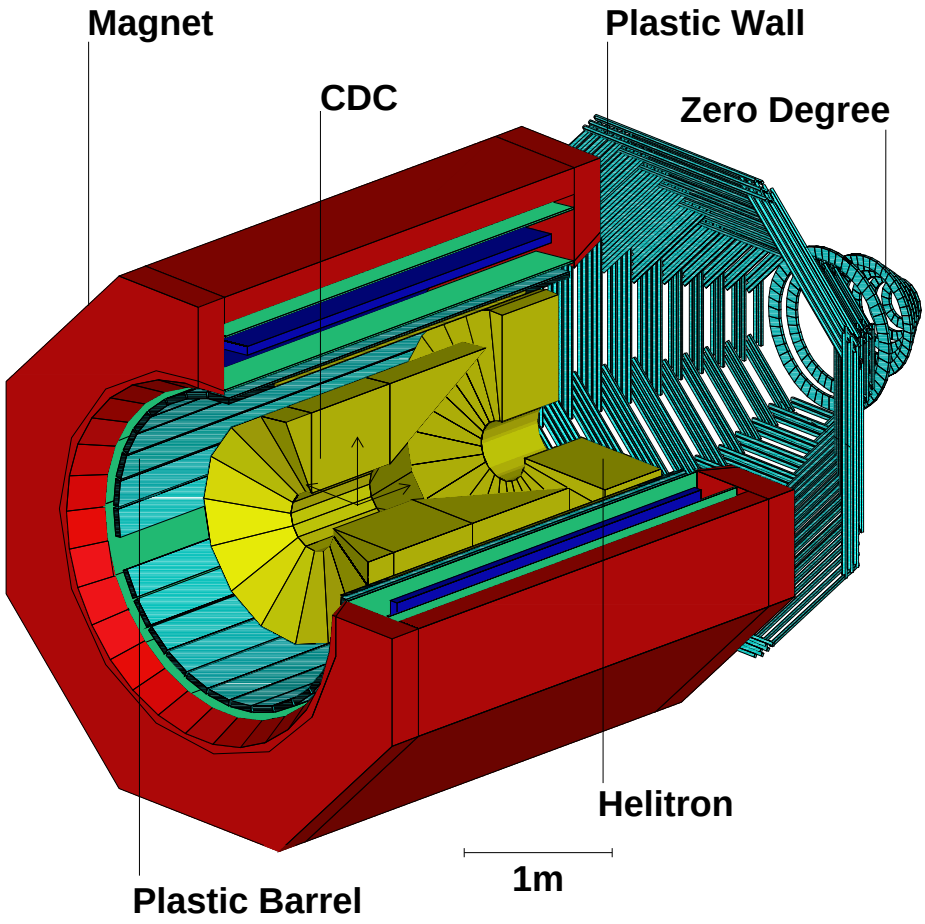

Figure 2.1: FOPI detector with its sub-detectors component

2.2.1 The Pion Beam Experiment with FOPI

In August 2004 the FOPI collaboration ran a secondary pion beam for 14 days in the cave B under the name S273 experiment. The pion production was performed with a primary beam of Carbon at the maximum incident energy available at SIS which is 2.0 AGeV. The advantage of using such a primary beam is that it has maximum intensity of produced pions, which is about $10^{11}\pi^-$ per spill at a momentum of 1.0 GeV/c with a resolution of 0.5% [88]. In this momentum range the electron contamination of the beam is at the lowest level (i.e. the e^-/π^- ratio is about 3/95). Due to the beam line acceptance and the transport of the beam over 89 m to cave B, the resulting pions intensity at the FOPI target was about $2.0 \cdot 10^4\pi^-$ per spill with a total cycle length of approximately 4 to 6 seconds.

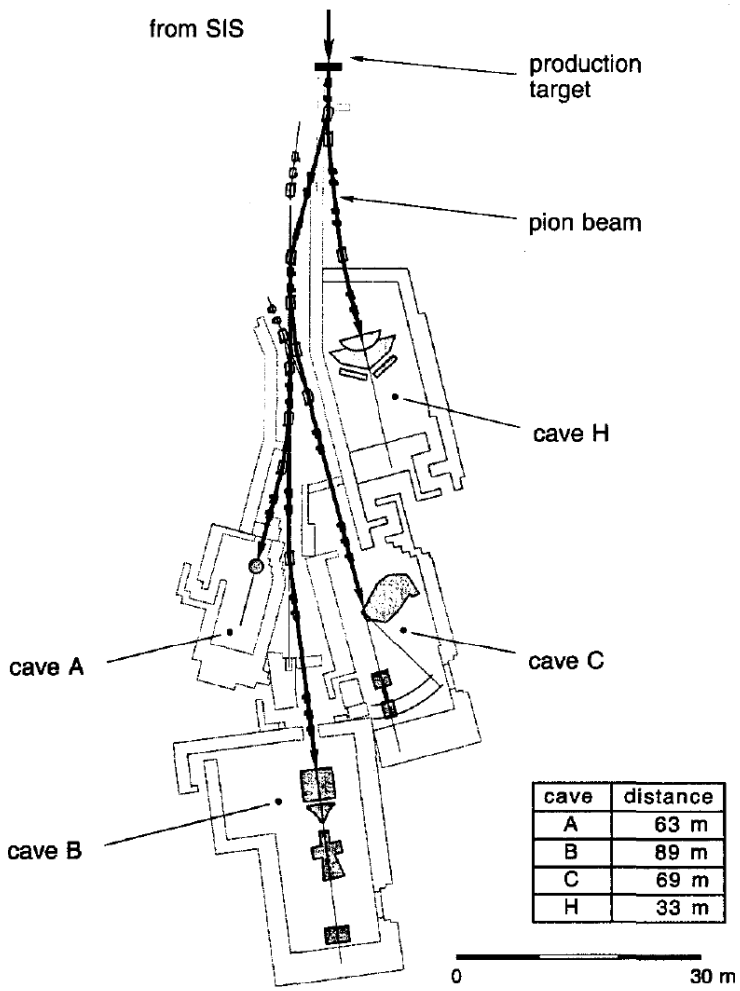

Figure 2.2: A schematic view of the pion production target and beam-lines to transport the pion beam to different experiment. The FOPI detector is located in the cave B [87]

2.3 Target Properties of the S273 Experiment

In order to have a complete systematic of the production probability and phase-space distribution of secondary and primary particles in pion induced reactions, five different targets were used in the S273 experiment. The target masses lie between $A = 12$ for Carbon and $A = 208$ for Lead. The properties of each target are given in table 2.1. Since the pion beam is a secondary beam, the size of the beam spot was roughly $2 \times 2\,\mathrm{cm}^2$. Hence it was necessary to use targets which have a size bigger than the beam spot, all targets have a size of $4.5 \times 4.5\,\mathrm{cm}^2$.

Target	$\rho \cdot d\,(\mathrm{g/cm^2})$	$\sigma_R\,(\mathrm{mb})$	$P(\%)$
C	1.87	264 ± 1	2.48
Al	1.56	454 ± 3	1.58
Cu	4.41	825 ± 25	3.44
Sn	2.83	1249 ± 6	1.80
Pb	5.76	1808 ± 6	3.03

Table 2.1: The thickness ($\rho \cdot d$) and interaction probability $P(\%)$ for each target. σ_R is the total cross section of π^- A reactions for each target, taken from [89].

The interaction probability P for each target is given by

$$P = (\rho \cdot d) \cdot \frac{N_A}{M} \cdot \sigma_R \tag{2.1}$$

σ_R is the total cross section, N_A is the Avogadro number, M is the mass of the target, ρ the density and d its thickness.

The quantity ρd for each target is given in table 2.1. The reaction cross section in pion induced reactions at a momentum of $1\,\mathrm{GeV/c}$ was taken from [89], for the Copper target there are no measurement for the reaction cross section, therefore the existing data points were fitted with a power law function [89] given by the formula

$$\sigma_R = C \cdot A^n \quad , \tag{2.2}$$

where A is the mass number of the nucleus. At an incident momentum of $1\,\mathrm{GeV/c}$ the constants have the value: $C = 49.4 \pm 1.5\,\mathrm{mb}$ and $n = 0.677 \pm 0.107$. The calculated interaction probability P for each target is presented in table 2.1.

2.4 The Start Counter

The start counter provides the time reference for all sub-detectors. It is placed in front of the FOPI detector at about 2.5 m from the target and tilted by 45° around the vertical axis. It is made from plastic scintillator and it measures the arrival time of the beam particles with a time resolution of 150 ps and the energy deposited in the scintillator. The signal is read out by two photo multiplier tubes.

2.5 The Veto Detector (Halo)

This sub-detector has two parts, Halo 1 and Halo 2. They are 5 mm and 2 mm thick scintillator respectively. Halo 1 is placed in front of the start counter, it is a veto counter used to spot the size of the beam. Halo 2 has a cylindrical hole in the middle, it is an additional veto detector placed in front of the target. Halo 1 and Halo 2 are in anti-coincidence with the start counter to reject beam particles which are not focused on the target.

2.6 The Beam Scintillator Detector

Since the pion beam has a wide spot of the order of 2×2 cm, this detector was used for an additional trigger to control the focusing of the beam. It was placed 30 cm in front of the target, it has 35×35 mm surface and 2 mm thickness. Figure 2.3 shows a sketch of the FOPI setup used during the pion beam experiment in August 2004.

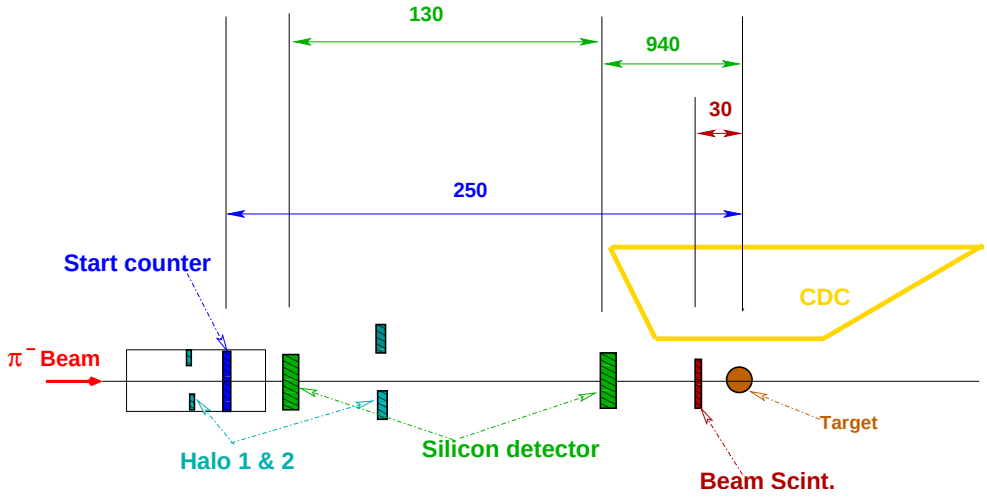

Figure 2.3: Positions of the beam scintillator and the silicon micro-strip detectors into the FOPI setup during the π^- beam experiment, (all distances are in cm).

2.7 The Central Drift Chamber (CDC)

The CDC is a jet chamber which has a cylindrical geometry. In this kind of chambers, the signal wires run in an axial direction forming the middle plane of a sector-

shaped cell with the electric drift field perpendicular to the beam axis. In the early 1980s this kind of chamber was constructed for the first time for the JADE detector at PETRA [90, 91]. Afterwards the OPAL experiment at LEP [92, 93] has built the same type of chamber, it had a different size and was more refined. The FOPI drift chamber has drift paths between 5 cm and 15 cm (correspond to a maximum drift time of 5 μs). This property helps the chamber to work in high event rates, it also gives the capability of recording events of high local track density with a good double track resolution and the possibility of particle identifications nearly in 4π.

2.7.1 The Mechanical Design

The active volume of the drift chamber is a cylinder with a length of about 2 m and 80 cm radius. The chamber is subdivided into 16 identical sectors. Each sector is delimited by 252 cathode wires (with 125 μm diameter) which produce the drift field. The middle plane of the sector consists of 61 potential wires (with 125 μm diameter) and 60 sense wires (with 20 μm diameter). The cathode, sense and potential wires are aligned parallel to the beam axis. The radial position of the innermost sense wire is at 20 cm and the outermost wire is at 80 cm. The length of each wire depends on its radial position, it varies between 86 cm and 196 cm [75] as it is sketched in figure 2.4. The applied voltage of -15 kV to the cathode through a voltage divider chain generates a homogeneous drift field of about 800 V/cm. A potential voltage of -1275 V is applied in each potential wire, this provide an electric field with a $1/r$ behavior around the sense wires (which are at zero potential) for the charge multiplication (avalanche).

The chamber is operated with 88% Argon, 10% Iso-butane and 2% Methane,the gas mixture was chosen such that it has a drift velocity v_D nearly independent of the drift electric field.

In each sector, the sense plane (made by the sense wires) is tilted by an angle at 8° (see figure 2.4), which helps to distinguish between real and mirror tracks (i.e. distinguish between left-right with respect to the sense wire). Another possibility to resolve the left-right ambiguity is the "staggering" of the sense wires by $\pm$ 200 μm with respect to the medium plane as defined by the potential wires.

2.7.2 Observables measured by the CDC

The identification of charged particles in the CDC is possible via the information about the momentum of the particle and its energy loss. The CDC is placed inside a magnet (superconducting solenoid) which produces a magnetic field of 0.6 T homogeneous to $\pm$1.5% in the central volume of the CDC. Due to the magnetic field, trajectories of charged particles emitted in a reaction (protons, pions, kaons,

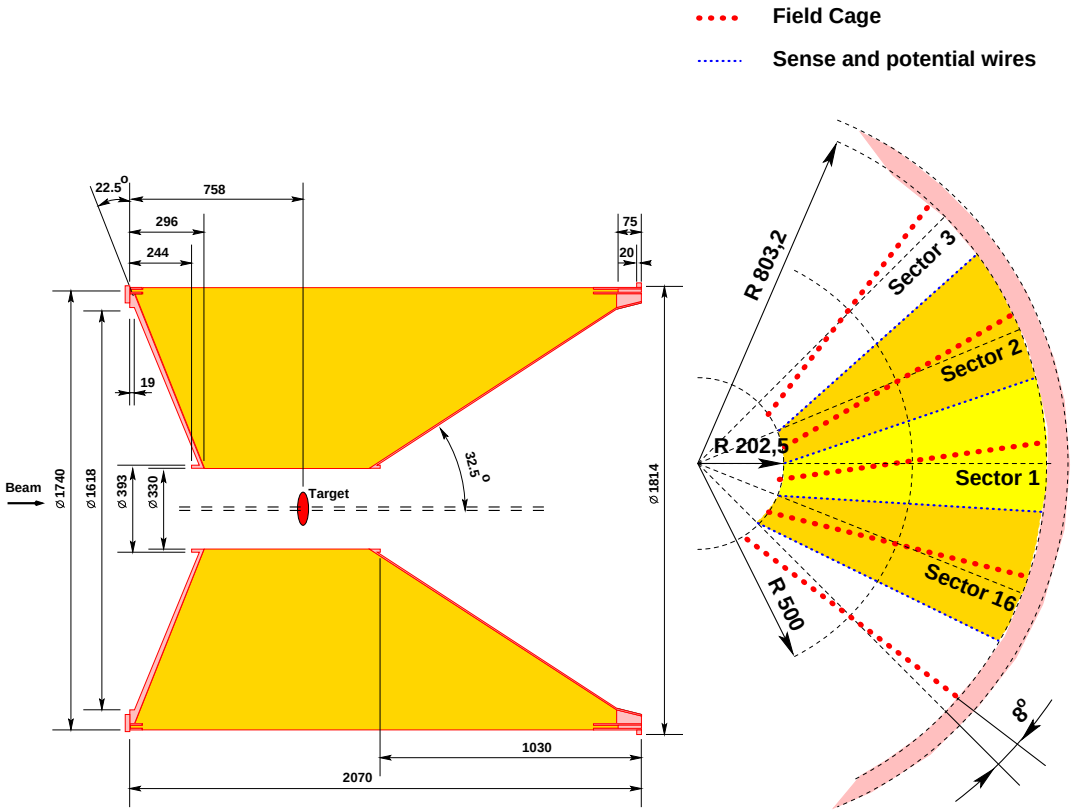

Figure 2.4: View of longitudinal and transverse cross section of the CDC. Left hand side: (r,z) view, the yellow color indicate the sensitive volume of the CDC. Right hand side: (x,y) view, blue dots in the middle of each sector are sense and potential wires. Red dots around each sector form the field cage (distances are in cm).

deuterons ....) inside the CDC are helices. To derive the momentum of the particle, the curvature of the track measured inside the gas volume of the CDC is needed. This can be done by reconstructing the positions of the hits (a hit is defined by the space coordinates of the collected charge on a sense wire) belonging to the track. The transverse momentum p_t and the momentum p are given by the following formulae :

$$\begin{aligned} p_t &= 0.3 \cdot |Z| \cdot B \cdot R \qquad \text{(GeV/c)} \\ p &= \frac{p_t}{\sin\theta} \qquad \text{(GeV/c)} \end{aligned} \tag{2.3}$$

Z: Charge number of the particle

B: Magnetic field in Tesla

R: Curvature of the charged particle

θ: Polar angle of the charged particle

The charged particles passing through the CDC ionize atoms in the gas volume, thus producing electrons which drift towards the sense wires. Close to the sense wires, electrons feel a strong field and the avalanches start. The collected charge of one track is proportional to the mean energy loss $\langle dE/dx \rangle$ of the particle.

After measurement of momentum and mean energy loss, one can identify the charged particles and their masses using the Beth-Bloch parameterization as shown in figure 2.5.

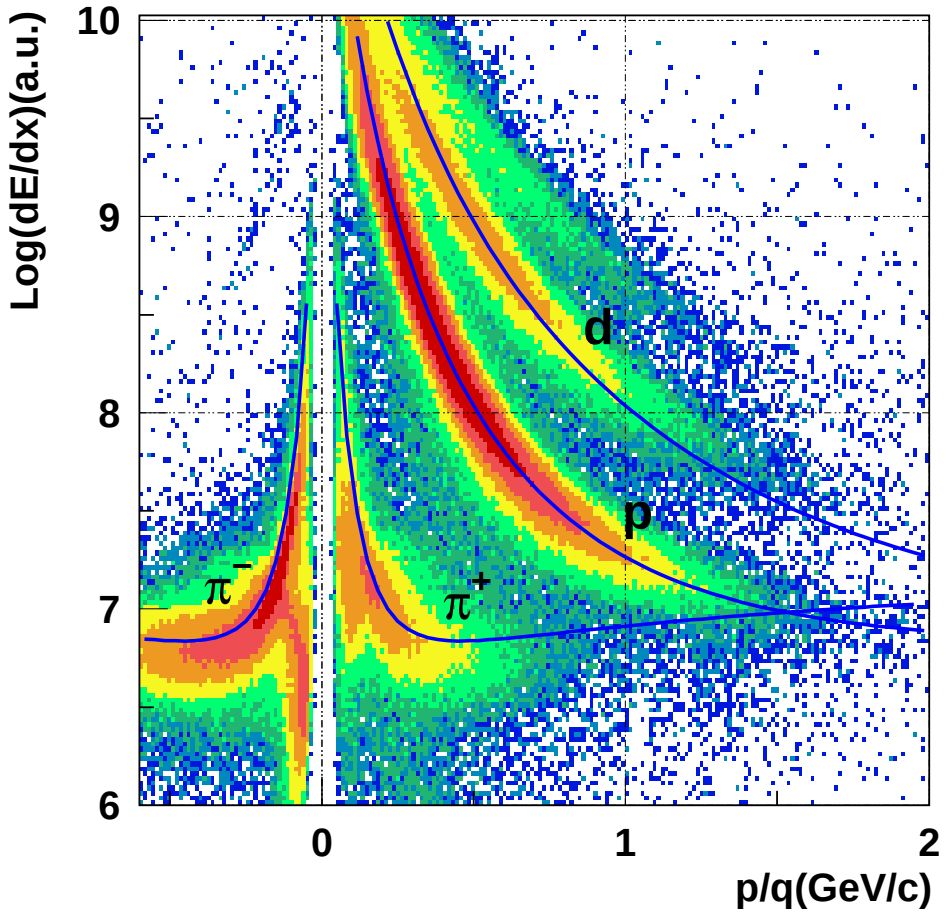

Figure 2.5: Particle identification with CDC: mean energy loss of particles in the CDC as function of their momenta. The lines are the Beth-Bloch parameterization of the energy loss, the color code indicates the particle number.

2.7.3 The Calibration of the CDC

In this section, the CDC calibration and how momentum and energy loss are obtained are discussed in general. In the S273 experiment on average three charged particles were registered per reaction. To identify tracks of particles inside the CDC, one needs to know the positions of the hits forming a possible track. In order to reconstruct the hit position in the (x,y) plane, one needs three parameters: the arrival time of the electrons at the sense wire (i.e. drift time) t, the Lorentz angle α_L and the drift velocity v_D. The CDC was built [94] in order to have a linear space-time response (i.e a uniform electric field, see formula (2.5)). In the presence of a magnetic field inside the CDC, the electrons change their drift properties due to the Lorentz force acting on moving electrons. In a constant electric and magnetic field, the electrons will drift along a straight line at an angle called Lorentz angle, with respect to the electric field lines as shown in figure 2.6. The relation between the drift velocity and the Lorentz angle is given by formula (2.4).

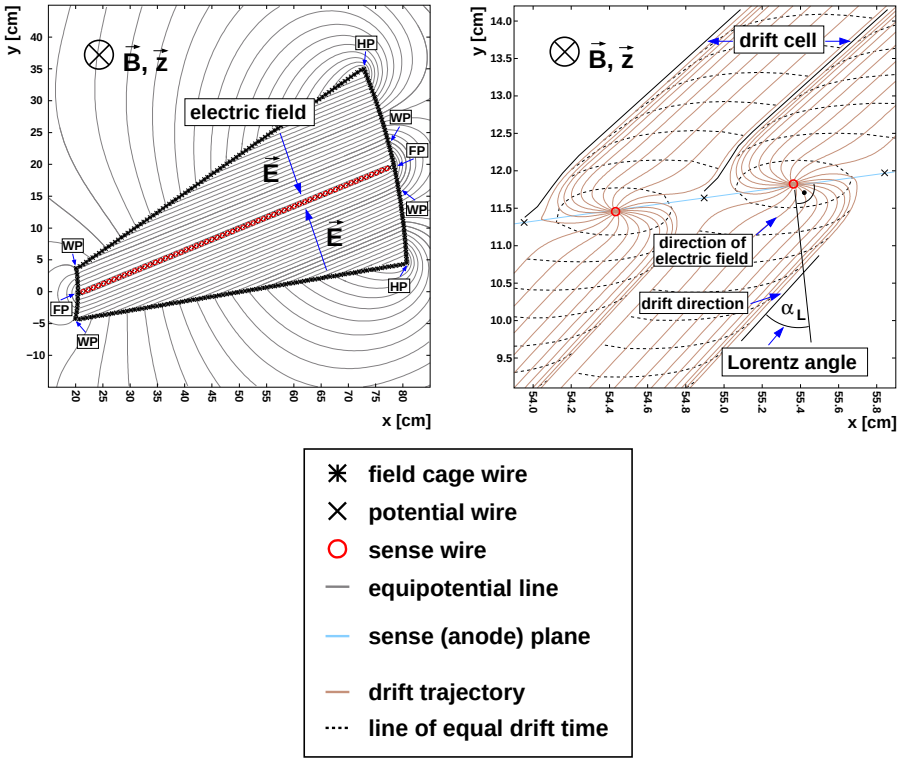

Figure 2.6: Illustration of the electric field (left plot) and the drift trajectories of electrons in (x,y) plane (right plot) [85].

$$v_D = \left(\frac{eE\tau}{2m_e}\right)\left(\sqrt{1+\left(\frac{eB\tau}{m_e}\right)^2}\right)^{-1}, \qquad \alpha_L = \arctan\left(\frac{eB\tau}{m_e}\right). \tag{2.4}$$

m_e: Electron mass

e: Electron charge

τ: Mean time between two collisions

B: Magnetic field strength

E: Electric field strength

The hit position in the (x,y) plane is linearly related to the drift velocity and is given by

$$\begin{pmatrix} x \\ y \end{pmatrix} = \begin{pmatrix} x_w \\ y_w \end{pmatrix} \pm \begin{pmatrix} cos(\alpha_L) \\ sin(\alpha_L) \end{pmatrix} \cdot v_D \cdot (t - t_w - t_0). \tag{2.5}$$

Here, (x,y) is the measured hit position and (x_w,y_w) is the position of the respective sense wire at which the charge was collected. t is the measured drift time of the electrons to the sense wires. t_w is the wire dependent time offset, it is the necessary time for the collected charge to travel from the wire to the Flash ADC. t_0 is the total time offset, it is the reference time in the clocks of the Flash ADCs. Formula (2.5) shows the importance of deducing the proper global parameters (t_0, α_L and v_D). The procedure used for their determination is based on a self-consistent method. The track finding algorithm used for this procedure is a local one [95, 96]. It reconstructs only tracks that have a high momentum (i.e. a very small curvature in the (x,y) plane). The calibration of the global parameters starts by first finding the right total time offset t_0. Panel (a) of figure 2.7 shows how a track with a wrong total time offset (before calibration) looks like. At the crossing border between two sectors of the CDC, the track is split. In panel b the same event is shown with the correct total time offset t_0 reached iteratively.

Once the total time offset is determined, the next step is to fix the Lorentz angle and the drift velocity. Those two parameters are correlated (see formula (2.4)), and thus can not be calibrated independently. Panel (a) of figure 2.8 shows a track arriving with a wrong drift velocity. The track is broken when crossing a sector border. The same event is shown in panel (b) with the right drift velocity, it becomes clear that the track is bent. The same holds for the Lorentz angle which is shown in panel (a) and (b) of figure 2.9 (v_D and α_L have the same effect on a track).

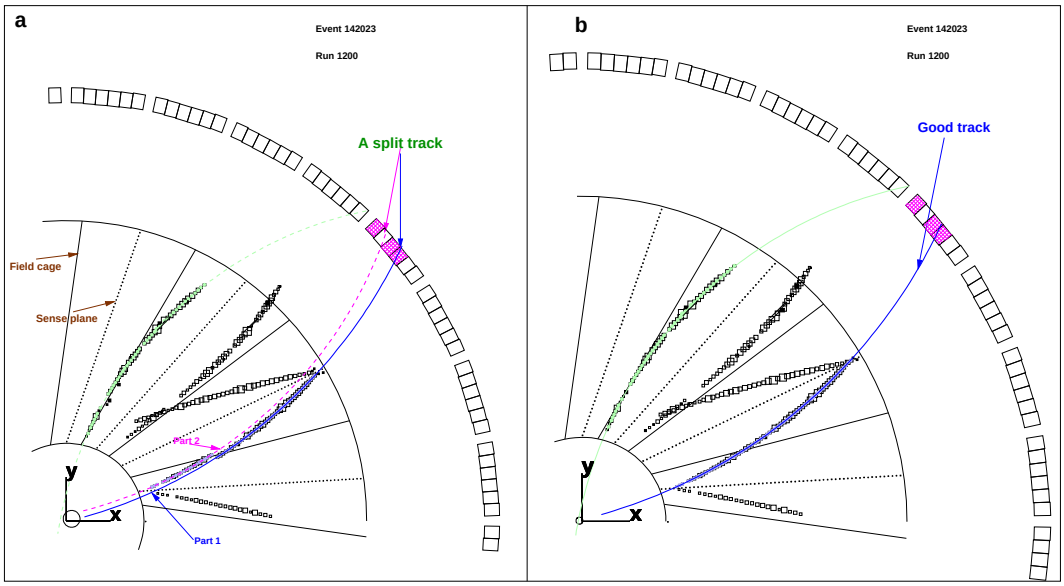

Figure 2.7: (a) An event with wrong total time offset the track is split into two parts. (b) The same event, now the two parts are joint together into one good track after calibrating the total time offset

2.7.4 The z Coordinate Calibration

After calibrating the global parameters which allow to have the coordinates of a hit in the (x,y) plane. The procedure of calibration to determine the z coordinate of a hit along a sense wire is presented in this section . We obtain that information via a charge division method [97, 98]. The ratio of the charges collected on the left and right ends of a wire is proportional to the ratio of the relative distances where the avalanche occurred and is given by

$$\frac{Q_L}{Q_R} = \frac{z}{L-z} \tag{2.6}$$

Where Q_L and Q_R are the collected charges on the left-hand side and right-hand side, respectively, z is the position along the sense wire from one end where the charge was collected and L is the length of the sense wire. Formula (2.6) shows the dependence of the collected charge ratio on the z position of the hit. It is mandatory to first calibrate the collected "charges" after the digitization by the Flash ADC module. The digitized numbers A_L and A_R are connected to the real electrical charges by constants g_L and g_R (i.e. the gain factors) as follows

$$\begin{aligned} A_L &= g_L Q_L, \\ A_R &= g_R Q_R. \end{aligned} \tag{2.7}$$

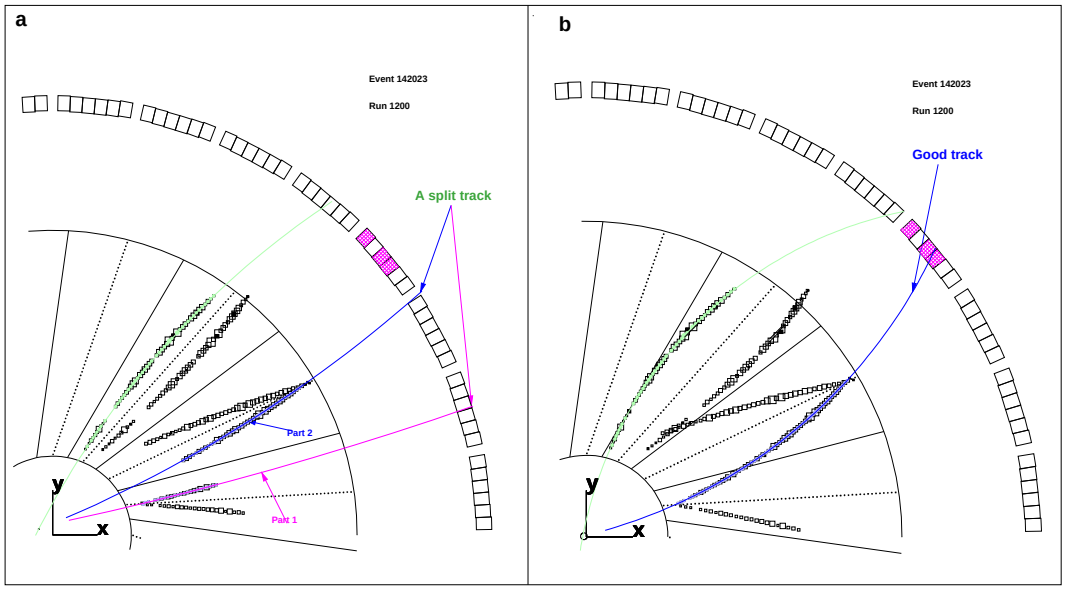

Figure 2.8: (a) Split track at the border line between two sectors of the CDC due to the wrong drift velocity. (b) After calibrating the drift velocity the two parts of the track fall together and form a single track (blue color).

The goal of the calibration is to have the ratio of digitized signals equal to the ratio of the real charges, $A_L/A_R = Q_L/Q_R$. This means that the ratio of g_L to g_R should be equal to unity after calibration and a good fit of the track finding in the (r,z) plane is required in addition. Figure (2.10) shows the ratio of the mean g_L to the mean g_R as function of the wire number. After calibration of the digitized signals at both ends of the sense wire, the proper z coordinate of the hit can be determined using

$$z_{\text{thit}} = z_0 + \frac{l_{\text{eff}}}{2}\frac{Q_R - Q_L}{Q_R + Q_L}. \tag{2.8}$$

Here, z_0 is the middle of the sense wire with respect to the target position. l_{eff} is the effective length of the sense wire defined as

$$l_{\text{eff}} = l_0\left(1 + \frac{2R_0}{R_w}\right). \tag{2.9}$$

Where, l_0 is the length of the sense wire, R_0 is the resistance of the preamplifier and R_w is the resistance of the sense wire.

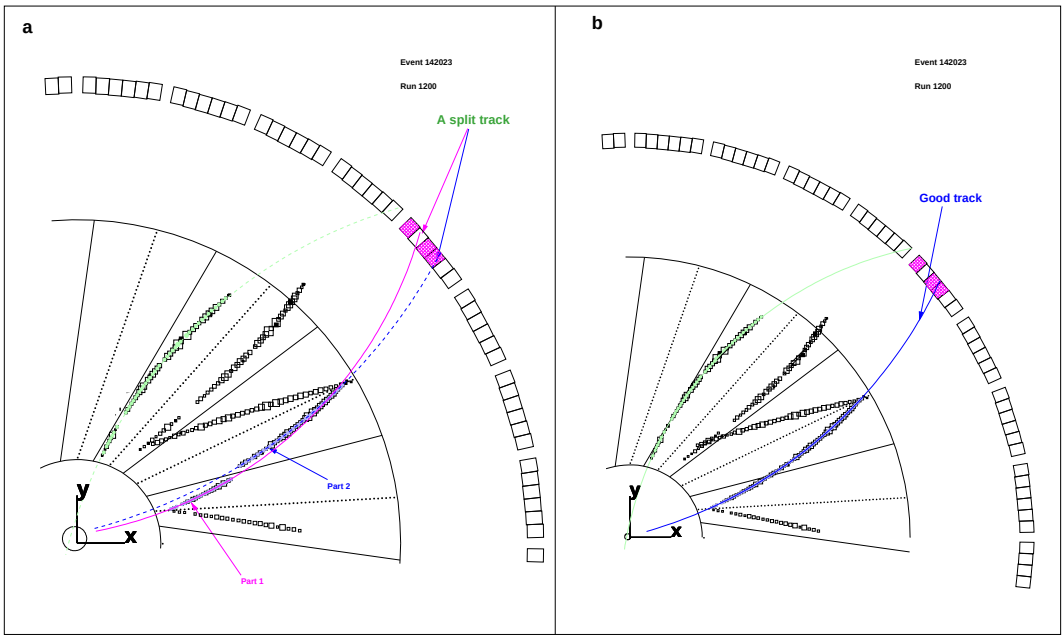

Figure 2.9: (a) Event with wrong Lorentz angle. The lower track is broken in two parts in the sector border. (b) The same event with the proper Lorentz angle.

2.7.5 The Energy-Loss Calibration

The total energy loss of a particle passing through the active volume of the CDC is proportional to the collected charge in each drift cell (see figure 2.6). The total energy loss for a hit is given by

$$\Delta E = f \cdot \left(A_R + \frac{g_R}{g_L} A_L \right). \tag{2.10}$$

f is a factor which takes into account the gas gain and the amplification factors of the preamplifiers at both ends of each wire. From the previous section it becomes clear now why one has to calibrate the collected charges first. The energy loss per unit path length for each track is derived using

$$\frac{\mathrm{d}E}{\mathrm{d}x} = \frac{\Delta E}{\Delta r} = f \cdot \left(A_R + \frac{g_R}{g_L} A_L \right) \frac{\sin\theta}{\Delta r_{xy}}. \tag{2.11}$$

Δr, Δr_{xy} are the lengths of a track in space and in the (x,y) plane, respectively and θ is the polar angle of the track. The calibration of the energy loss consists of the calibration of the parameter f, which for a good calibration has a constant mean value.

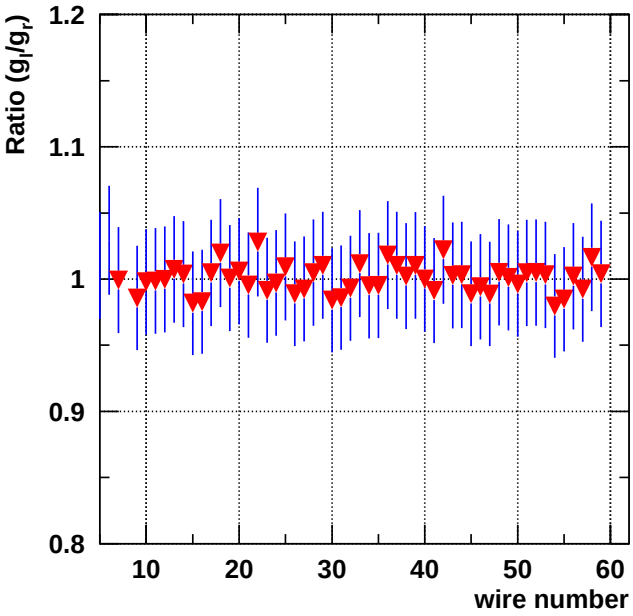

Figure 2.10: Ratio of gain factors g_L to g_R of the wires in sector one.

After the calibration of the energy loss, its statistical distribution looks like a Landau distribution. To have a precise measurement of the mean energy loss, the mean of the lowest 70% of the measured ionizations per track are used. This truncation reduces the fluctuations of the mean energy loss.

2.8 The Scintillator Barrel

The Plastic Barrel detector surrounds the CDC at a radius of 111 cm. It covers polar angles from 27 ° to 57 ° and around 85 % of the full azimuthal angle. It consists of 180 plastic scintillator strips, each has a rectangular cross section of $4 \times 3\,\mathrm{cm}^2$ and a length of 150 cm. The light produced by charged particles in a given strip is collected at both ends of the strip by a photo multiplier tube. This gives the time of flight and the hit position along the z-axis for a charged particle. The time resolution of the plastic barrel is about 300 ps and the position resolution about 7 cm. The combination of momentum from the CDC and the velocity from the Plastic Barrel allows for a better identification of charged particles. This is the

method to identify charged kaons with the FOPI detector as shown in figure 2.11.

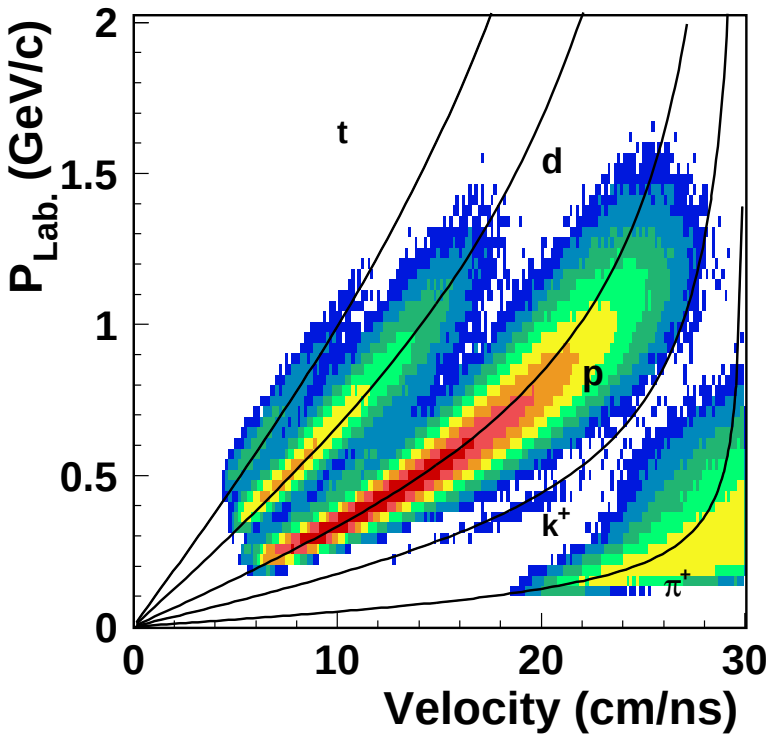

Figure 2.11: Momentum of charged particles from the CDC versus their velocity from the Barrel. Lines are the Beth-Bloch parameterization derived with nominal masses of particles with charge Z=1.

2.9 The Helitron

The Helitron is a a radial drift chamber filled with the same gas mixture as the CDC. The polar angle acceptance of this detector ranges from 7 ° to 30 ° This chamber is divided into 24 sectors. Each of them has 54 sense wires and 53 potential wires perpendicular to the beam axis. As in the case of the CDC, the charged particles are identified via their energy loss in the sensitive volume and their track curvature. At the position of the Helitron, the magnetic field is not homogenous. However, it has been measured and it is known with an accuracy of 0.5 % [99]. For this reason the azimuthal angle of the detected particles in the

transverse plane has to be corrected. The correction is given by the formula

$$\phi_{corr} = \phi + \frac{12^\circ}{p[\mathrm{GeV/c}]}, \tag{2.12}$$

where ϕ_{corr} is the corrected azimuthal angle due to the inhomogeneity of the magnetic field, ϕ is the measured azimuthal angle and p is the total momentum of the detected particle. As in the case of the CDC and the Barrel, one can combine the momentum from the Helitron and the velocity from the Plastic Wall (PLAWA) (see figure 2.11) to have a better identification of charged particles in the PLAWA. The momentum of charged particles passing through the Helitron as a function of their velocity from the PLAWA is plotted in figure 2.12.

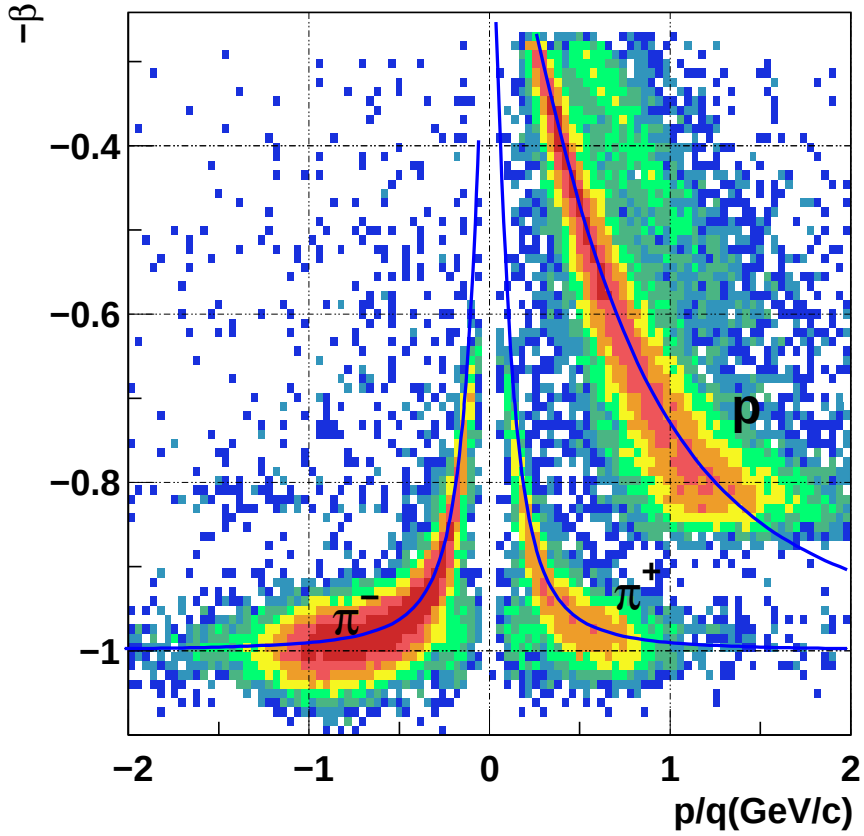

Figure 2.12: Matching between Helitron and PLAWA, plotted is the momentum of charged particles measured with the Helitron versus their velocity measured with the PLAWA. The differentiation between positively and negatively charged particles is due to their curvature measured in the Helitron. The color code indicates the number of particles.

2.10 The Forward Wall

The forward wall covers polar angles from 1.2 ° to 30 ° and the full azimuthal range. It consists of two parts: the outer wall called “Plastic Wall” (PLAWA) and the inner wall called “Zero Degree” (ZD).

2.10.1 The Plastic Wall (PLAWA)

Like the Plastic Barrel the Plastic Wall is made of 512 plastic scintillator strips divided into eight sectors. Each sector is composed of 64 strips. The light produced by a charged particle on a given strip is read out at both ends of the strip via photo multipliers. Each strip delivers four signals, two energies (E_L,E_R) and two times (t_L,t_R). The energy loss ΔE of a particle is proportional to $\sqrt{E_L \cdot E_R}$ and its time of flight is proportional to $\frac{1}{2} \cdot (t_L + t_R)$. The position of a particle hitting the PLAWA is given by the angular position of the strip which fired. The time resolution is linked to the active length of the scintillator strip, thus it varies from 80 ps for strips in the inner sector to 120 ps for strips in the outer sector. The resolution of the hit position varies from 1.2 cm to 2.0 cm [74, 75].

2.10.2 The Zero Degree Detector

This detector covers polar angles from 1.2 ° to 7.0 ° and consists of 252 plastic scintillator strips grouped into 7 concentric rings. Each module is read out by only one photo multiplier and delivers the energy loss (ΔE) and the time of flight of charged particles. The time resolution of this detector is about 200 ps.

2.11 The Silicon Strip Detector (SDD)

In the S273 experiment, two silicon micro-strip detectors were used. The aim of using them was mainly to ensure the π^- beam was focused on the target since the pion beam is a secondary beam [87]. Figure 2.3 shows a sketch how those two detectors were positioned with respect to the FOPI setup. The silicon micro-strip detectors have a size of $3.2 \times 3.2\text{cm}^2$ and a thickness of 300 μm with a resistivity of $6 - 10\,\text{k}\Omega\text{m}$. The operating voltage of each silicon strip detector is $50 - 60\,\text{V}$. Since they were used for focusing the beam, the *x* and *y* coordinates were needed. For this reason, both silicon micro-strip detectors are double sided (Strips of one side are perpendicular to the strips of the other side). Each side contains 1280 strips with a pitch of 25 μm. To reduce the number of readout channel only strips at 50 μm are read out [100, 101]. The position of the particle is obtained by com-

puting the center of gravity of the charges collected at several readout strips.

2.12 Determination of the Cross Section

The S273 experiment was devoted to the measurement of the strangeness production in π^- induced reactions. The reaction products are mainly reconstructed in the CDC acceptance. Therefore, one needs a minimum bias trigger for the CDC. Figure 2.13 shows the trigger system used in the pion beam experiment. It sketches how the number of beam particles used for the measurement of the cross section are counted.

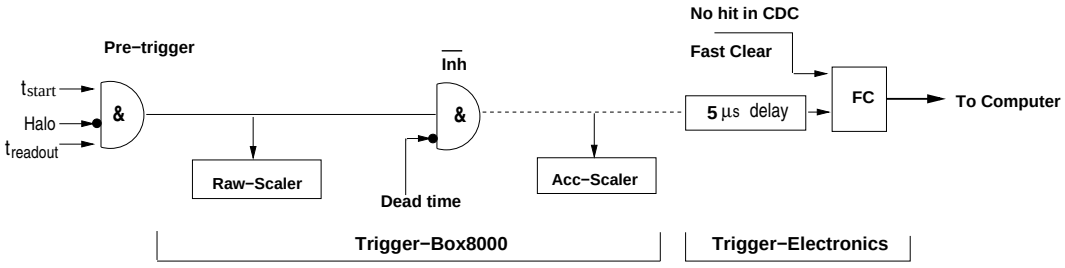

Figure 2.13: A sketch of the trigger system used in the pion beam experiment.

The number of strange particles $N_{\rm st}$ produced per unit time is given by

$$N_{st} = N_{\rm Beam} \cdot N_{\rm targ} \cdot \varepsilon_{\rm dead} \cdot \sigma_R \quad , \tag{2.13}$$

σ_R is the inclusive reaction cross section (i.e. of the reaction $\pi^- + N \rightarrow K + Y$, where K=$K^+$ or K^0 and Y=Σ or Λ). $N_{\rm Beam}$ is the number of π^- beam particles passing through the start counter without producing a signal in the Halo detector. $N_{\rm targ}$ is the number of target nuclei per cm^2 and $\varepsilon_{\rm dead}$ is a factor which takes into account the dead time of the detection system. This factor is given by

$$\varepsilon_{\rm dead} = \frac{N_{\rm acc}}{N_{\rm raw} \cdot L} \quad , \tag{2.14}$$

where $N_{\rm acc}$ is the number of beam particle fulfilling a trigger called “Fast Clear”. This trigger requires a certain number of hits in the CDC, otherwise the event will be rejected or cleared. $N_{\rm raw}$ is the number of beam particles which pass the trigger box. L is the life time fraction of the detector which can be written as $L = 1 - t_{\rm dead}$, where $t_{\rm dead}$ is the dead time fraction of the detector. The quantity $\varepsilon_{\rm dead} \cdot N_{Beam}$ in (2.14) is the called the inhibited number $\overline{N_{\rm inh}}$ of beam particles

which fulfill our trigger condition (this number is written in the List Mode Data files (LMD) as well as to the Data Summary Type (DST)). Therefore, the inclusive reaction cross section for a given strange particle is given by

$$\sigma_R(\pi^- + A \rightarrow K(Y) + X) = \frac{N_{K(Y)}}{\overline{N_{\text{inh}}}} \cdot N_{\text{targ}} \quad . \tag{2.15}$$

Chapter 3

Data Analysis

The aim of the S273 experiment is to measure the in-medium cross section of the reaction $\pi + N \rightarrow K^0 + \Lambda$. To count the number of neutral strange particles, their daughters have to be identified among the other particles in each event.

The possibility that those events contain also background can not be excluded. The background contamination is due to non-target reaction and double events (i.e. pile up). It is extremely important to discard those background events to measure the cross section properly.

In this chapter, the data analysis of the s273 experiment is explained in detail. Event selection, particle identification in the CDC and PLAWA methods are presented.

3.1 Event Selection

3.1.1 Rejection of non-target Reactions

Due to the large transverse dimension of the pion beam (i.e. the beam spot is about $2 \times 2\,\mathrm{cm}^2$ wide), it is possible that pions hit different parts of the detector without making a reaction in the target. Those events resulting from non-target reactions are considered as background. To reduce this kind of reactions, a trigger called "Good Beam" is applied. It relies on the signal from the start detector and halo detector as a veto (i.e. whenever the halo is hit by a pion, the event will be rejected). Even if beam particles fulfill these trigger conditions, it is possible that they react with detector materials in the space between the start counter and the target. For this reason, a small scintillator counter in front of the target is installed (i.e. at 30 cm far from it). This counter was used as an additional trigger input to the first one, and is called "Better Beam" trigger. To further suppress non-target events, the CDC event vertex was calculated. By definition, the space coordinates

of the CDC vertex (v_x, v_y, v_z) are the mean values of track intersections in space. A typical distribution of the vertex in the (x,y) plane is depicted in figure 3.1. There are no constrains on the vertex in the (x,y) plane because pions can hit the whole target surface (all targets have $4.5 \times 4.5\,\mathrm{cm}^2$ surface). The vertex along

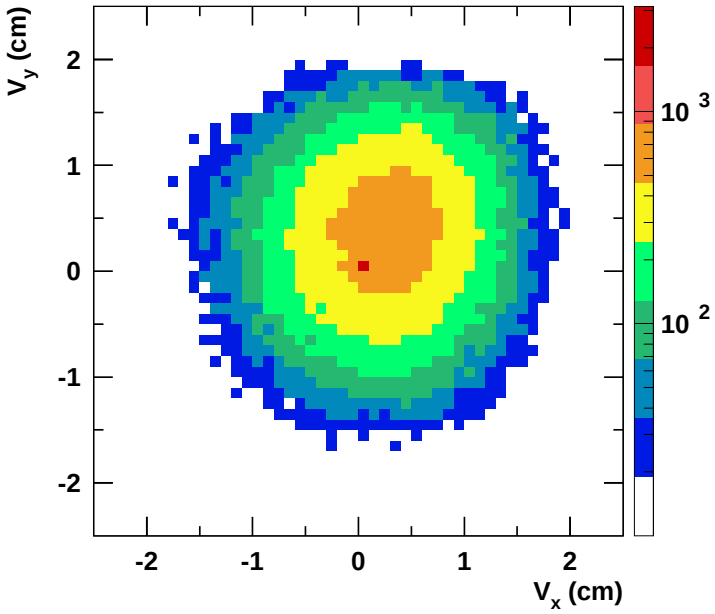

Figure 3.1: CDC Vertex distribution in the (x,y) plane. The beam spot has a circular surface which is not exactly centered at (0,0).

the z axis is plotted in figure 3.2: Two peaks can be clearly identified, one at the nominal target position 0 cm and the other one around -30 cm. The latter one is due to reactions of pions with the small counter. To discard those reactions, the v_z distribution is fitted with a Gaussian and only those in the range of $\pm 3\sigma$ around the nominal vertex (i.e. the resolution σ of the vertex in the z direction is about 4 cm)are selected.

The other possible source of background, are multiple events. If two pions arrive at the start counter in a time interval at less than 100 ns (the QDC has a gate of 100 ns), then they can not be distinguished as two independent events. The pion beam intensity was $3000 - 5000\,\pi^-$ per second, this means that on average each 200 μs one pion passes through the start counter and interacts with the target. Under those beam conditions it is almost impossible to have double interactions

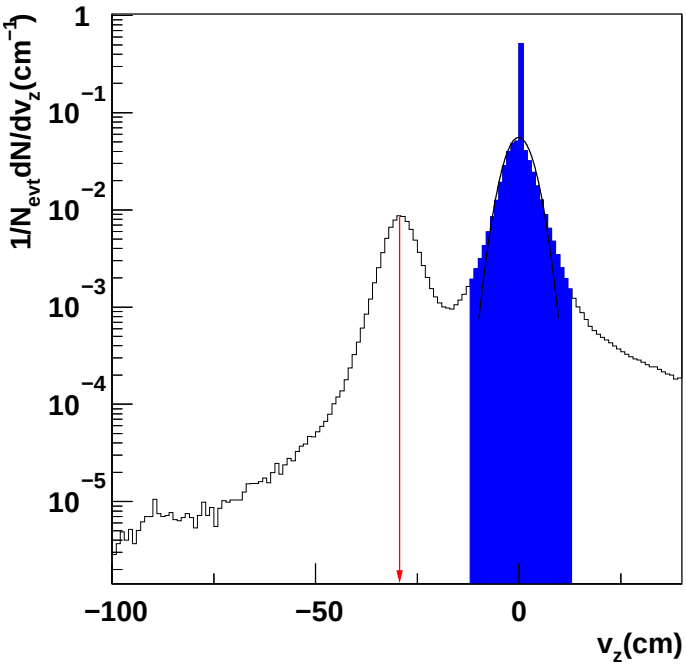

Figure 3.2: Distribution of the CDC Vertex along the z axis. The peak at -30 cm is due to the reactions of π^- beam particles with small counter (see text). The shaded area represents the accepted events in a range of $\pm 3\sigma$ around the nominal vertex.

in one event. Figure 3.3 shows the distribution of the deposited energy of pions passing through the start counter. The shape of the distribution is smooth and does not show a double-peak structure. The distribution of the reference time of the arrival pions on the start counter is shown in figure 3.4: it is centered around the channel 1000 (i.e one TDC channel is equivalent to 50 ps). To reject background, all events within $\pm 3\sigma$ are accepted, as it is indicated by the shaded area.
Under those selection criteria (i.e. cuts on the vertex v_z of the CDC and the time in the start counter), the number of remaining events for the five targets which were used are presented in table 3.1. The fraction of good events (i.e. with background level below 3%) to bad ones (i.e. events which contain background) is used to calculate the corresponding number of beam particles. Those numbers for each target are written in table 3.1.

3.2 Detector Acceptance

According to Tsushima et al. [67], the reaction $\pi + N \rightarrow K + Y$ (i.e K could be a K^+ or K^0 and Y is a hyperon it could be a Σ or a Λ) is not isotropic. They predict

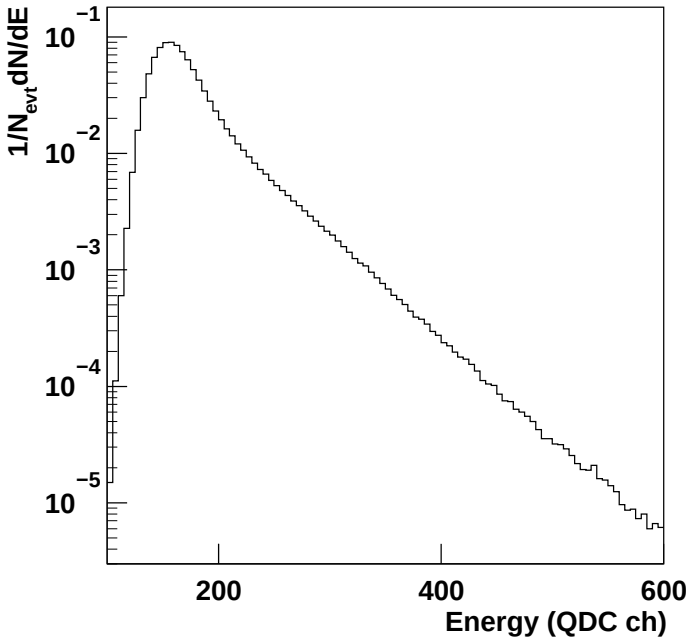

Figure 3.3: The distribution of the deposited energy of π^- beam particles in the start counter.

Target	Number of events before cut	Number of events after cut	Number of beam particles before cut	Number of beam particles after cut
C	10 004 002	8 701 144	415 186 213	361 212 005
Al	66 1097	559 327	65 452 062	54 979 733
Cu	1 048 495	938 453	59 595 181	53 039 712
Sn	1 443 854	1 244 588	59 735 244	51 372 310
Pb	12 011 336	10 653 130	368 214 310	327 710 736

Table 3.1: Number of events and beam particles before and after cutting on the time of the start counter and the vertex v_z of the CDC.

a preferential emission of the hyperon in the forward direction in the laboratory frame. For this reason, we look for daughters of strange particles in both parts of the FOPI detector, the CDC and the PLAWA. The Λ is reconstructed in the PLAWA and CDC, and the K^0 in the CDC.

Figure 3.5 shows phase space distribution of protons detected in the CDC and

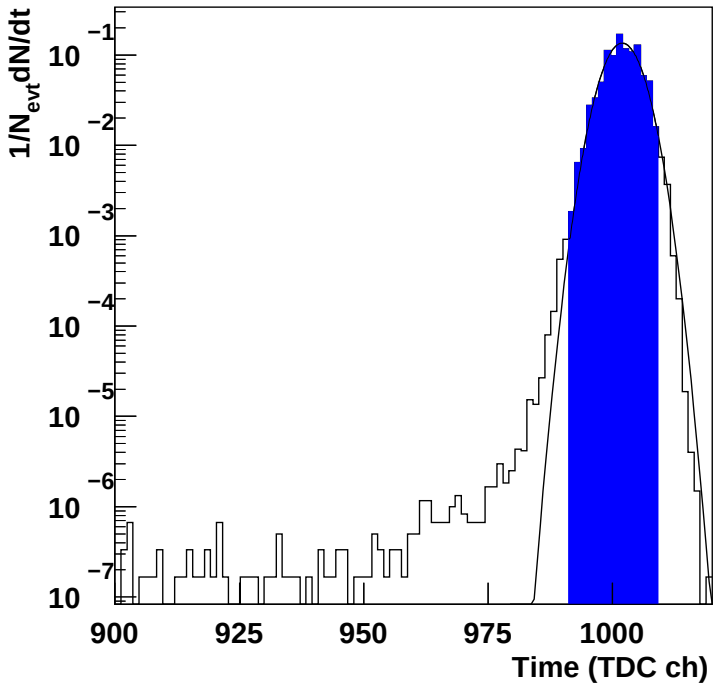

Figure 3.4: Distribution of arrival time in the start counter of π^- beam particles.

the PLAWA (i.e. the transverse momentum of protons p_t as function of their rapidity y (see appendix B) in the laboratory frame). The full lines in figure 3.5, show the geometrical acceptance of each sub-detector. The CDC occupies $2/3$ of the full space and the PLAWA roughly $1/3$ of it.

3.3 Particle Properties

In the CDC, particles are identified via their momentum and their energy loss. Figure 2.5 shows the energy loss of particles as function of their momenta. The mass of particles can be derived using the Bethe-Bloch parameterization with an iterative procedure (see appendix A). The obtained mass distribution of all particles detected in the CDC is shown in figure 3.6. The quality of the calibration is reflected in a good mass separation of particles. Heavy particles like deuterons can be seen and distinguished from protons in this experiment. Moreover, particles detected in the CDC are characterized by the transverse distance to the primary vertex in the (x,y) plane and also by the distance z_0 along the z axis. Panel a of figure 3.7 shows a sketch of a track in the (x,y) plane. Its radius of curvature r is connected to the transverse momentum via formula (2.3). d_0 is the transverse dis-

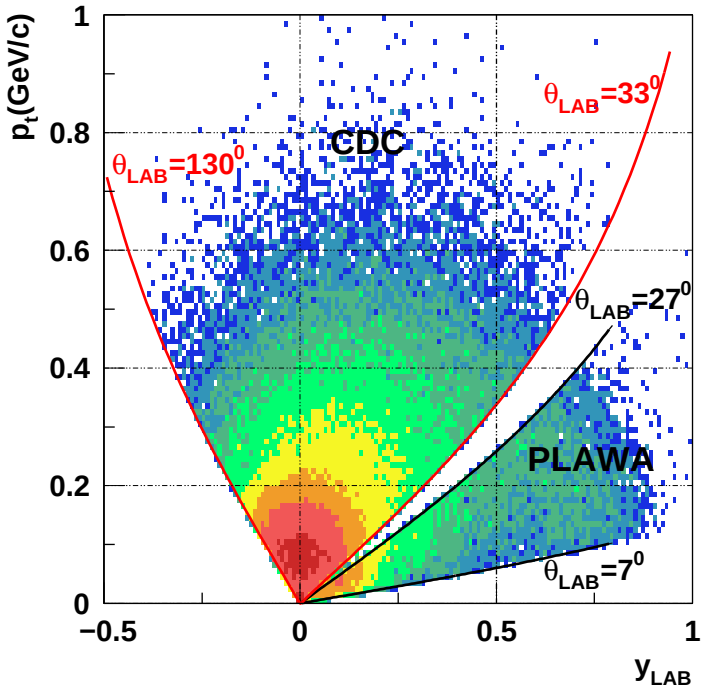

Figure 3.5: Geometrical acceptance of the FOPI detector.

tance to the primary vertex. The tracks of secondary particles (i.e. daughters of a decay of strange particles or resonances) do not point to the primary vertex, hence they have bigger values of d_0 as compared to primary particles. The azimuthal emission angle ϕ_0 of a particle in the (x,y) plane is also defined in panel *a*. Panel *b* of figure 3.7 shows how is defined the z_0 distance of a track to the primary vertex in the (r,z) plane (θ is the longitudinal angle between the track and the z axis).

In the PLAWA, particles are identified using their velocity v and their specific energy loss. Figure 3.8 shows the correlation matrix between the mean energy loss and the velocity of particles, the line indicates the parameterization according to the Beth-Bloch formula (see Appendix A). In π^- A reactions only particles with charge $Q = \pm 1$ are seen in the plastic wall. To distinguish between positive and negative charged particles, the matching between the Helitron and the PLAWA is needed. The curvature of particles passing trough the Helitron is employed, thus particles with negative charge have a negative curvature and positively charged particles have a positive curvature. Figure 2.12 demonstrates that with the matching, distinction between π^-, π^+ and protons is very good.

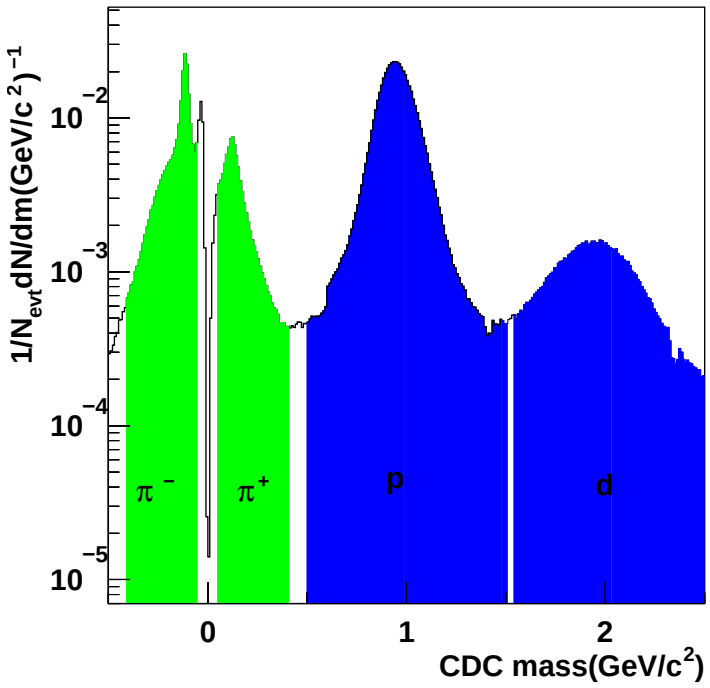

Figure 3.6: CDC mass spectrum from π^- Pb reactions, the spectrum is deduced from Beth-Bloch parameterization.

3.4 Reconstruction Methods of V^0

The name V^0 was assigned to the strange meson K^0 when it was discovered in a bubble chamber [102]. It was called V^0 because it is neutral and the charged daughters form a V shape at the decay point of the K^0. Charged daughters of the strange baryon Λ form also a V shape at the decay point of the particle. For the process of the strong interaction, the strangeness is conserved, thus in pion induced reactions, there must be an associated production of strange particles. Their decay mechanism is being different from their production, they decay relatively slow (i.e. typically about 10^{-10} s) by weak force.
Since FOPI detector can only identify charged particles, the K^0 and Λ must be identified through their charged decay channels. The Λ has a mean life time of $2 \cdot 10^{-10}$ s and decays with a branching ratio of 64% into π^- and proton. The K^0 is a mixed state of K^0_S and K^0_L. The K^0_L has a mean life time $c \cdot \tau$ of roughly 15 m, this means that it decays outside the FOPI detector. The K^0_S has a mean life time $c \cdot \tau$= 2.67 cm and it decays into π^- and π^+ with a branching ratio of 68%. Only this particle can be reconstructed with the FOPI detector.
Panel *a* of figure 3.9 shows a schematic view of the disintegration of a V^0 (Λ or

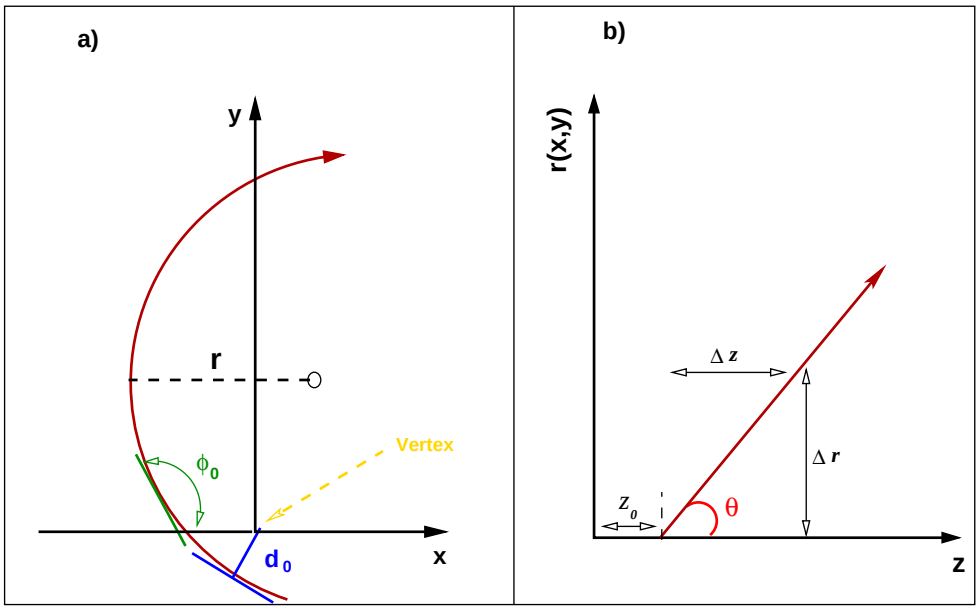

Figure 3.7: Quantities characterizing the position of particles inside the CDC.

K^0_S) in the (x,y) plane. The same picture in the (r,z) plane is shown in panel *b* . Those two pictures contain all geometrical and kinematical variables characterizing the decay. To calculate the secondary vertex coordinates (x_s,y_s) with respect to the primary one, we solve the equation of intersection of the two circles in the (x,y) plane. The trajectories of the two particles π^- and π^+ (proton) can intersect if the distance d_{21} between their circle centers m_1 and m_2 is less than the sum of their radii $r_1 + r_2$. Once this condition is fulfilled, the intersection of the circles can be parameterized with the angle α. In the (r,z) plane, tracks which have a relative distance $\mid z_1 - z_2 \mid$ with respect to the primary vertex less than Δz, are selected for reconstructing the secondary vertex in the (r,z) plane.

To identify neutral strange particles, one has to look to the invariant mass spectrum.

3.4.1 Invariant Mass Spectra of K^0_S and Λ

The method to obtain the invariant mass spectra of the neutral strange hadrons Λ and K^0_S reconstructed out of particles detected in the CDC acceptance is described here.

The invariant mass is given by

$$M_{\text{inv}} = \sqrt{(E_1 + E_2)^2 - (\vec{p}_1 + \vec{p}_2)^2} = \sqrt{E^2 - \vec{p}^2} \tag{3.1}$$

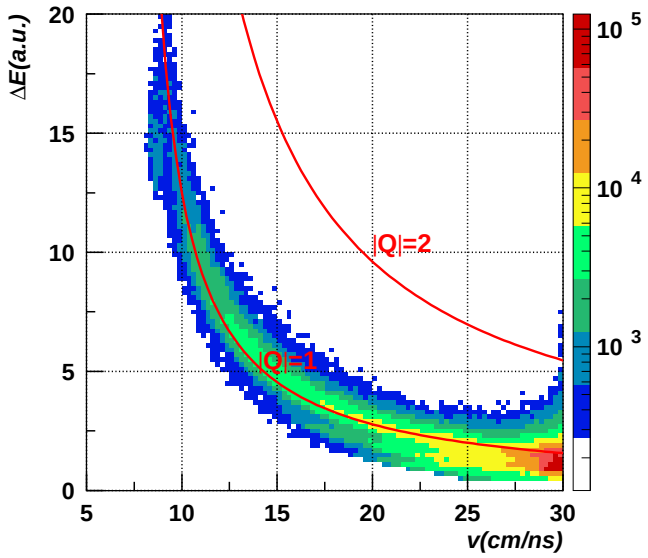

Figure 3.8: Energy loss of charged particles detected in the PLAWA as a function of their velocities. Only particles with charges ± 1 reach the PLAWA in π^- Pb reaction.

The subscripts 1 and 2 refer to a π^- and π^+ or proton respectively. E is the total energy and $\vec{p}$ is the momentum of a particle. In combining the four momentum of a π^- with the one of a π^+ (proton) to calculate the invariant mass spectrum of a K^0_S or Λ, the possibility to have a combinatorial background can not be excluded. Its origin is due to completely uncorrelated (π^-, π^+(proton)) pairs. To reduce the background, selection criteria are applied to the π^- and π^+(proton) kinematical and geometrical variables.
In table 3.2 all variables describing daughters of K^0_S and Λ and also the range of their variation are presented. For both particles π^- and π^+ a minimum transverse momentum of 80 MeV/c is required, to make sure that both particles reach the outer radius of the CDC. For the proton a corresponding minimum momentum of 100 MeV/c is required. This helps to reject particles curling inside the CDC. In first order the transverse distance to the vertex d_0, is not restricted, because for some events the vertex could not be calculated and therefore is taken at its nominal value. In reality daughter particles of K^0_S and Λ have a transverse distance d_0 different than zero. The mass is selected in a wide range, because at high momentum the CDC mass resolution is getting poor. The selected range of the hit multiplicity helps in choosing good tracks by avoiding broken ones.

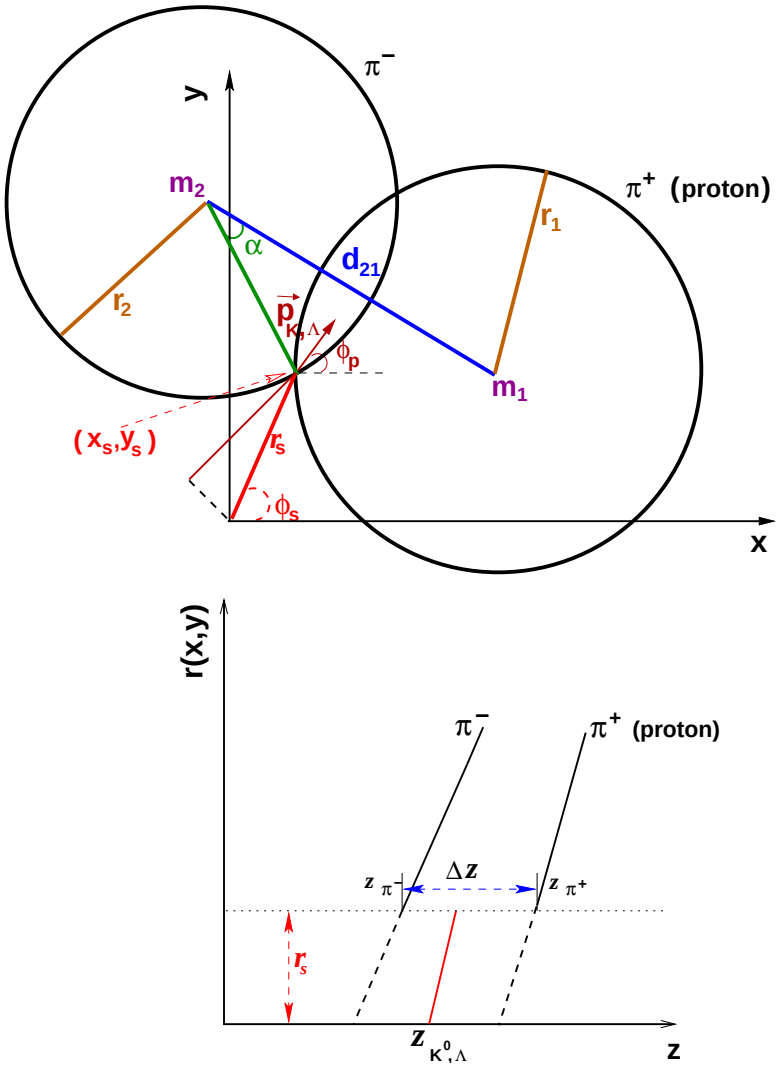

Figure 3.9: Sketch of the $K^0_S(\Lambda)$ decay in the (x,y) (upper plot) and in the (r,z) (lower plot) planes of the CDC. This plots schematize also the reconstruction method of strange particles (see text for explanation).

A pre-selection criteria of kinematical and geometrical variables of the K^0_S and Λ is also addopted while reconstructing their invariant mass spectra. The variables and their allowed variation range are listed in table 3.3. All variables are defined in figure 3.9.

Panel *a* of figure 3.10 depicts the combinatorial invariant mass spectrum of the K^0_S reconstructed in the lead target. It shows a peak around the nominal mass of the K^0_S above a continuous background. This background is called the "com-

	Daughters	
Mother particle: K^0_S	π^-	π^+
	$\mid d_0 \mid < 20.$ cm	$\mid d_0 \mid < 20.$ cm
	$0.05 <$ mass < 0.8 GeV/c^2	$0.05 <$ mass < 0.8 GeV/c^2
	$p_t > 80.$ MeV/c	$p_t > 80.$ MeV/c
	$N_{\text{hits}} > 24$	$N_{\text{hits}} > 24$
	Daughters	
Mother particle:Λ	π^-	*proton*
	$\mid d_0 \mid < 20.$ cm	$\mid d_0 \mid < 20.$ cm
	$0.05 <$ mass < 0.8 GeV/c^2	$0.5 <$ mass < 1.5 GeV/c^2
	$p_t > 80.$ MeV/c	$p_t > 100.$ MeV/c
	$N_{\text{hits}} > 24$	$N_{\text{hits}} > 24$

Table 3.2: Quantities used to characterize daughters of strange particles and their allowed ranges.

Mother particle	M_{inv} (GeV/c^2)	r_s (cm)	$\lvert\phi_s - \phi_p\rvert$ $(^\circ)$
K^0_S	$0.35 \ldots 0.8$	$0. \ldots 20.$	$\leq 360.$
Λ	$1. \ldots 1.5$	$0. \ldots 30.$	$\leq 360.$

Table 3.3: Alowed ranges of geometrical $(\phi_s - \phi_p)$ and kinematical (r_s) variables characterizing K^0 and Λ particles.

binatorial background". In order to know how much K^0_S are under the peak, one has to subtract the background. There are two different methods to describe the combinatorial background, the first one is to fit it with a polynomial or exponential function. This depends on the shape of the background itself. This method is used if on has a very good ratio of signal over background. The other method is called the "Event Mixing" method. In this analysis, we adopt this method. It consists of combining one π^- from one event with $n\pi^+$ (n protons), each one from a different event to produce another invariant mass spectrum (for more details about the method see [103, 104]). Panel *b* of figure 3.10 shows a spectrum of the event-mixing background. Before subtracting it from the combinatorial background, one has to normalize it. The spectrum is multiplied by a weighting factor which is evaluated from the ratio of the combinatorial background in the mass region

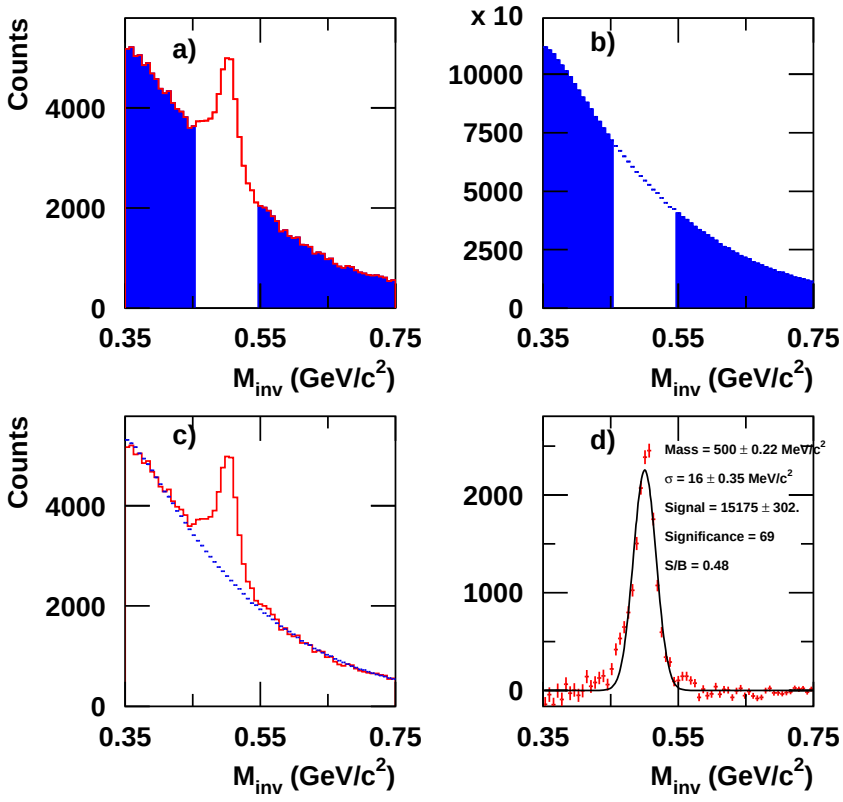

Figure 3.10: Invariant mass sepctra of K^0_S reconstructed in π^- Pb reactions. Shaded area in panel (a) and (b) show the invariant mass region where the event-mixing bacground is scaled. Panel (c) depicts the scaled event-mixing background in top of the combinatorics spectrum. Panel (d) shows the K^0_S invariant mass spectrum after background subtraction.

where there is no peak, to the event-mixing background in the same mass region (i.e shaded area in panels *a* and *b*). The combinatorial spectrum is shown in panel *c*, and on top of it the normalized event mixing spectrum is plotted. After subtracting the background, a peak remains centered at the nominal mass of the K^0_S as it is shown in panel *d*. This confirms that the event-mixing method describes the combinatorial background well. To derive the other quantities characterizing the K^0_S or Λ (momentum, rapidity, flight path, ...), the corresponding event-mixing background spectrum is multiplied by the weighting factor obtained from the invariant

mass evaluation. Afterwards, we subtruct it from the corresponding combinatorial spectrum.
To calculate the number of K^0_S under the peak of panel *d*, the spectrum is fitted with a Gaussian-type function. The mean of the fit is the nominal mass of the K^0_S and the variance σ is the mass width. The sume of all entries in a mass range of $\pm 2 \cdot \sigma$ is taken as the number of K^0_S under the peak. The peak is characterized by two quantities: the signal over background ratio and the "significance" defined as

$$\text{Significance} := \frac{S}{\sqrt{S+B}}, \tag{3.2}$$

where *S* and *B* are the signal and background counts respectively of K^0_S under the peak. A clear signal has typically a significance larger than 3 [103].
Panel *a* of figure 3.11 depicts the K^0_S invariant mass spectrum reconstructed in π^- C reactions. The histogram with the full line (in red) is the combinatorial K^0_S invariant mass spectrum, and the histogram with dashed line (in blue) is the event-mixing background. It can be seen in the mass region 0.35 up to $0.45\,\text{GeV}/c^2$ and 0.55 up to $0.65\,\text{GeV}/c^2$ that the event-mixing curve does not match with the combinatorial one. The event-mixing overestimates the background in the lower mass region and underestimates it in the mass region 0.55 up to $0.65\,\text{GeV}/c^2$. The obtained K^0_S invariant mass spectrum after subtraction is shown in panel *b*. To further understand the behaviour of the event mixing, one can reconstruct K^0_S invariant mass spectra in different (p_t, y) bins (i.e. different phase-space regions) (for the definition of the rapidity *y* see appendix B). The study is done in four bins of rapidity for all transverse momenta p_t. Figure 3.12 illustrates the reconstructed K^0_S invariant mass spectra in four different phase-space regions. The backward hemisphere is delimited by rapidities below -0.2, rapidities between -0.2 and $+0.2$ represent the target rapidity and the forward hemisphere is delimited by rapidities above 0.2. The upper left plot shows the invariant mass spectrum of a K^0_S in the phase-space region $0.2 < p_t < 0.3$ GeV/c and $y < -0.2$. It can be seen that after subtraction of the background some (π^-, π^+) correlations are remaining on both sides of the K^0_S peak which can not be handled by the event-mixing method. The same effect can be seen in the forward-hemisphere at transverse momenta $0.1 < p_t < 0.2$ GeV/c. Below $0.5\,\text{GeV}/c^2$ in mass the event-mixing method overestimates the background and above $0.55\,\text{GeV}/c^2$ up to $0.65\,\text{GeV}/c^2$ the event-mixing underestimates the background. The lower two plots show the reconstructed K^0_S invariant mass spectra in the forward hemisphere at momenta $0.3 < p_t < 0.4$ GeV/c. The same observations as before can be made. In the other phase-space regions which are not shown here, event-mixing spectra have the same behaviour as in figure 3.12. This behaviour can be explained by the fact that when combining π^- with π^+, it is not excluded that the selected π^+ particle is a misidentified proton, since the CDC mass cut is open for a π^+ up to $0.8\,\text{GeV}/c^2$.

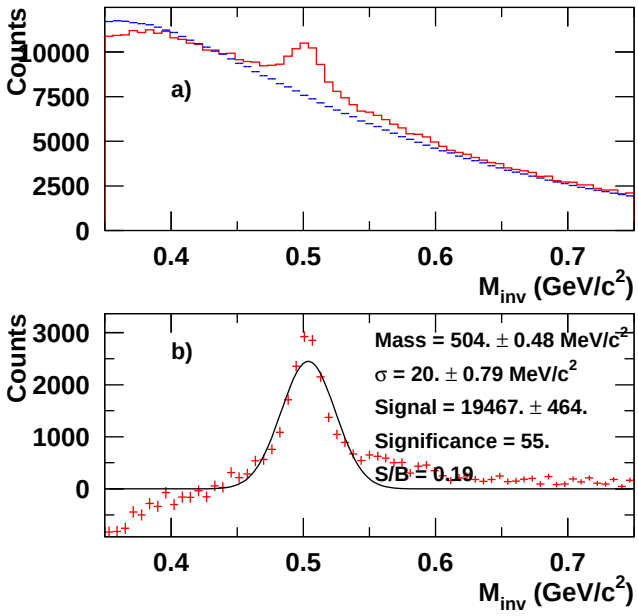

Figure 3.11: Invariant mass spectra of K^0_S reconstructed in π^-C reactions. Panel (a) shows the scaled event-mixing background (red) and on top of it the combinatorial spectrum. Panel (b) contains the signal after subtracting the background.

In this case, it is possible to have correlations in the K^0_S combinatorial background which originate from $\Sigma^0(\Lambda)$ particles (decays into π^- proton with 64% branching ratio) or from Δ and N^* resonances (decay into π N with different branching ratios). If such correlations exist in the combinatorial background, the event mixing method is not able to describe the combinatorial background properly. For the time being, it is not possible to study such effects, since the available transport models (HSD or IQMD) do neither contain the correlated kinematics of the associated strangeness production ($K^0 - \Sigma^0(\Lambda)$) in pion-induced reactions nor the K^0 production via multi-step processes (which happens via Δ and N^* resonances).

In this situation, the only way to match the event-mixing background with the combinatorial one, is to cut on appropriate variables. The cut will increase the signal over background and also the event-mixing background will match the combinatorial one quite well but a lost on the number of candidates is expected. Variables on which one can are:

- The transverse distance d_0 to vertex of daughter particles. Since those par-

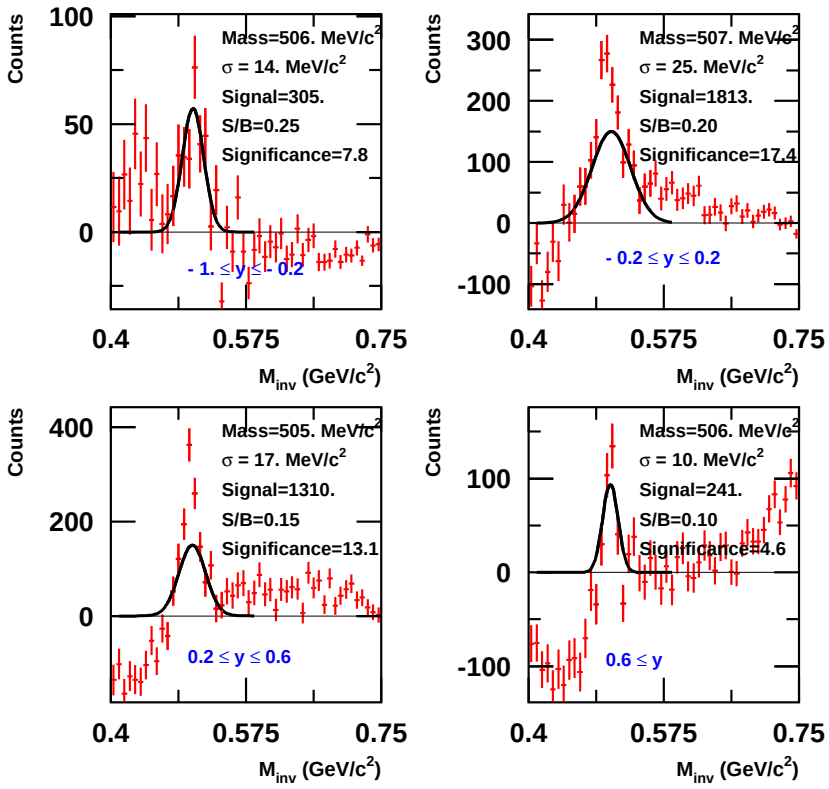

Figure 3.12: Invariant mass spectra of K^0_S reconstructed in π^-C reactions in different (p_t, y) bins. All pictures depict the corrected invariant mass spectrum. They are obtained in the same way described in figure 3.10.

ticles originate from a secondary vertex (i.e. decay point of the mother particle K^0_S), their absolute transverse distance to the primary vertex should be bigger than zero.

- The other variable is the pointing angle $\Delta\phi = \phi_p - \phi_s$ (it reflects the detector resolution), for a perfect detector it should be close to zero.

Figure 3.13 shows the reconstructed K^0_S invariant mass spectra in π^- C and π^- Pb reactions when using the set of cuts given in table 3.4. The signal-over-background ratio is improved by roughly three orders of magnitude in the case of

Cut quantities	$d_0(\pi^-)$ (cm)	$d_0(\pi^+)$ (cm)	$\Delta\phi$ (°)
Variation ranges	$\lvert d_0(\pi^-)\rvert \geq 1.5$	$\lvert d_0(\pi^+)\rvert \geq 1.5$	$\lvert\Delta\phi\rvert < 30°$

Table 3.4: Additional cut quantities used to describe the combinatorial background with event-mixing method.

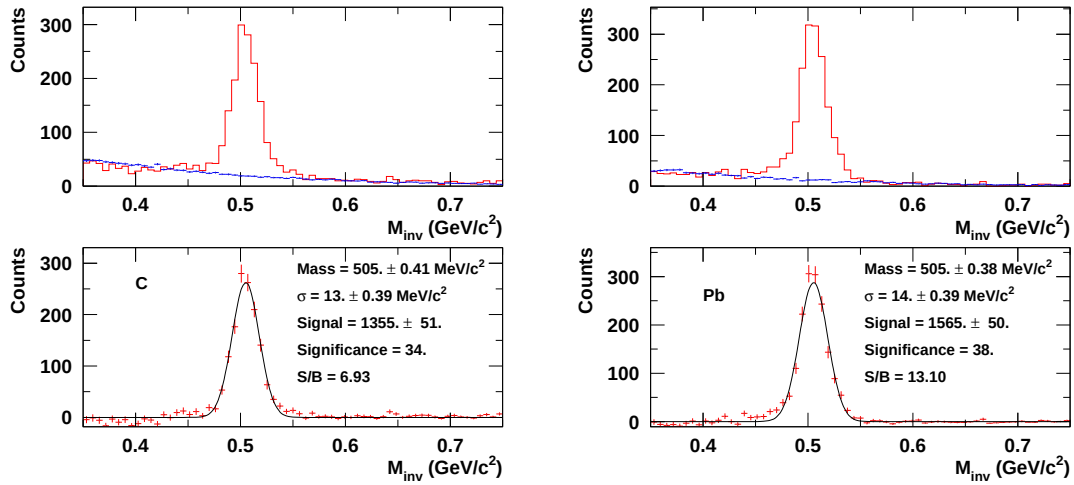

Figure 3.13: The obtained K^0_S invariant mass spectra in π^-+C (left) and in π^-+Pb (right) using set of cuts defined in table 3.4.

the Lead target. The signal-over- background ratio for the Carbon target improved by about factor 20. One can see that the event-mixing background matches perfectly with the combinatorial one, but one looses roughly one order of magnitude in the number of reconstructed K^0_S.

It is possible to use another set of cuts which leads to a good description of the combinatorial background with the event-mixing method. This set includes cuts on the same variables presented in table 3.4 but their variation ranges differ, in addition the opening angle $\Delta\phi_p = \phi_{\pi^-} - \phi_{\pi^+}$ between the daughter particles (π^-, π^+) in the transverse plane is used. Their allowed range of variation is presented in table 3.5.

To derive the Λ signal (where both particles $\pi^-$and proton are detected in the CDC) the same method is used as for the K^0_S. Also the same steps as in figure 3.10 are followed to count the number of Λ particles. The event-mixing method was used to evaluate the background. Since the cut on the CDC proton mass is open

Cut quantities	$d_0(\pi^-)$ (cm)	$d_0(\pi^+)$ (cm)	$\Delta\phi$ (°)	$\Delta\phi_p$ (°)
Variation ranges	$\|d_0(\pi^-)\| \geq 0.7$	$\|d_0(\pi^+)\| \geq 0.7$	$\|\Delta\phi\| < 60°$	$\|\Delta\phi_p\| > 90°$

Table 3.5: Second set of cut quantities used to describe the combinatorial background with event-mixing method.

(see table 3.2), it is not excluded to correlate a π^- with π^+ instead of proton to reconstruct the Λ invariant mass spectrum. Hence the same problem is faced as in the case of K^0_S, where the background can not be described properly by the event- mixing method. To have a reasonable description of the background using the event-mixing method a cut strategy is needed. In this work no absolute inclusive yield of the produced Λ in the CDC will be derived, therefore no further investigations of the event-mixing background method and cut strategy will be presented.

3.4.2 Λ^0 Reconstruction in the Forward Wall (PLAWA)

The reconstruction of the Λ in the PLAWA means to combine a proton detected in the PLAWA with a π^- detected in the CDC. This method has been developed for the first time in FOPI and is important for further applications when one aims at correlation a forward going Λ with other particles [105]. The π^- is selected adopting the same criteria as in the case of the K^0_S and Λ reconstruction in the CDC. Since the proton is detected in the PLAWA, it needs to be distinguished from a pion (π^- or π^+). In this case the role of the Helitron is crucial. Combining the curvature of particles from the Helitron and the velocity from the PLAWA, gives a clear separation between pions (π^- and π^+) and protons as is shown in figure 2.12.

The velocity of all particles with a charge $Q = \pm 1$ is depicted in figure 3.14. Two parts can be distinguished in the histogram, one starts at $\beta = 0.$ goes up to $\beta = 0.85$ and the other one starts at $\beta = 0.85$ and ends at $\beta = 0.99$. From the figure 2.12 it can be clearly seen that pions (π^- and π^+) are concentrated around $\beta = 0.99$ and the protons are located at about 0.85. To avoid the contamination (in the velocity spectra of the protons) by pions, protons in the PLAWA are chosen with velocity less than $\beta = 0.75$ (i.e. corresponding to $v = 22.5\,\mathrm{cm/ns}$). In table 3.6, the selection criteria for π^- and proton are summarized.

Figure 3.15 illustrates the Λ decay into a proton going to the PLAWA and a π^- going to the CDC, in the (x,y) and $(r(x,y),z)$ plane. In FOPI, particles detected in

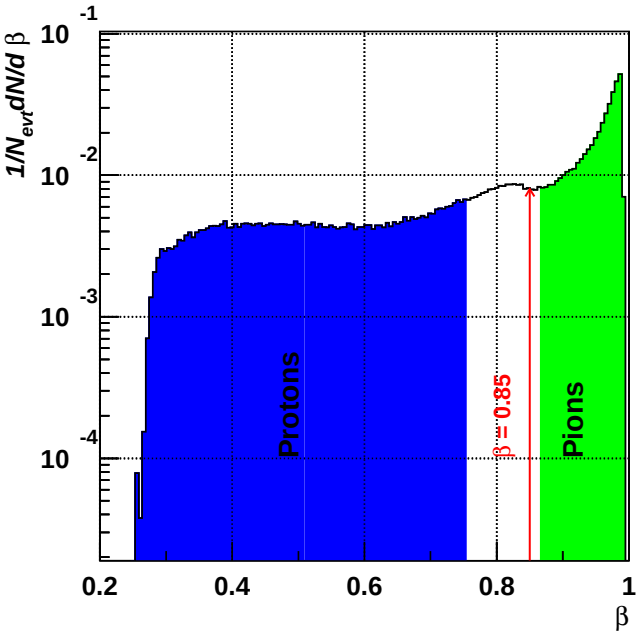

Figure 3.14: Velocity distribution of particles with charge $Q = \pm 1$ detected in the PLAWA.

	Daughters	
Mother particle:Λ	π^-	proton
	$\mid d_0 \mid < 20.$ cm	$\mid Q \mid = 1$
	$0.05 < mass < 0.8$ GeV/c^2	$v \leq 22.5$ cm/ns
	$p_t > 80.$ MeV/c	
	$N_{\text{hits}} > 24$	

Table 3.6: Quantities characterizing daughters of Λ particle and their variation ranges.

the PLAWA are assumed to come from a vertex situated at $(v_x, v_y, v_z) = (0,0,0)$ and due to the inhomogeneity of the magnetic field at the location of the Helitron, the azimuthal angle of particles has to be corrected (see formula (2.12)). When a Λ particle is decaying the largest part of its momentum is taken by the proton because they are close in mass (i.e. $\Delta m = 178\,\text{MeV/c}^2$). This means that the

momentum vector of the Λ and the proton are close to each other. As an approximation, we assume that the flight path of the Λ and the proton in the transverse plane, are the same as it is shown in the left panel of figure 3.15. To reconstruct the secondary vertex, the transverse distance $d_{\pi p}$ between the circle center of the π^- and the flight path of the proton have to be calculated. This distance should be always less than the radius of the circle. The decay of the Λ in the (r,z) plane is shown in the right panel. The difference between the z position of both particles is required to be less than Δz.

Once the secondary vertex is determined, we reconstruct the invariant mass of

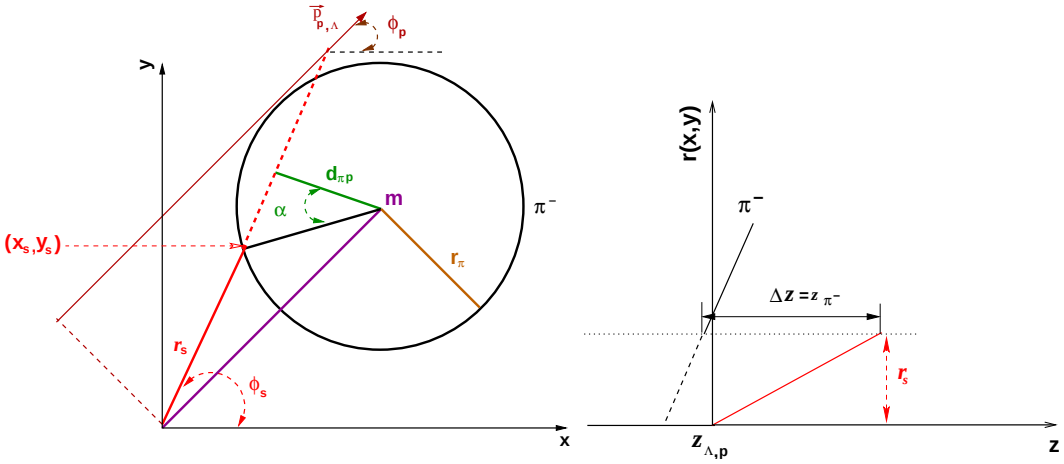

Figure 3.15: Schematic view of the Λ decay in the forward direction of the FOPI detector. The right panel illustrates the decay of Λ in the (x,y) plane of the CDC. The left panel shows its decay in the (r,z) plane.

the Λ. The pre-selection criteria for the variables describing the Λ properties are presented in table 3.7.

Pre-selected quantities	M_{inv} GeV/c^2	Δz (cm)	$\Delta\phi$ (°)	r_s (cm)
Variation ranges	1....1.5	≤ 20	$\leq$ 360	≤ 50

Table 3.7: Quantities characterizing the Λ particle used as a pre-selection criteria for invariant mass reconstruction.

Using formula (3.1), four momentum of π^- and proton which fulfill the conditions in table 3.6 are combined to reconstruct the invariant mass of the Λ. The

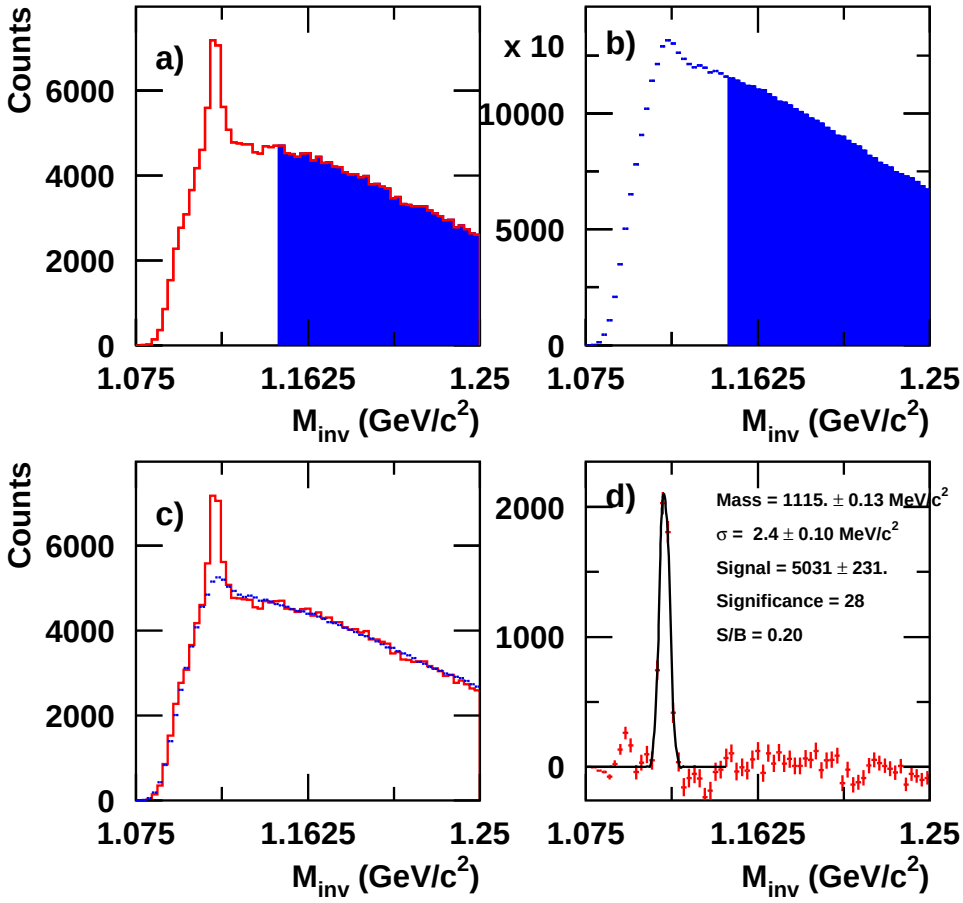

Figure 3.16: Illustration of the reconstruction method of the Λ invariant mass spectra in π^-+ Pb reactions. The same steps are followed as in figure 3.10.

combinatorial invariant mass spectrum is plotted in panel *a* of figure 3.16. It shows a peak centered at the nominal mass of the Λ. Panel *b* shows the event-mixing background, the shaded area in panels *a* and *b* show the range where the event-mixing background is normalized. Panel *c* demonstrates the event-mixing background in blue dashed lines on top of the histogram in red line originating from the combinatorics. One can see clearly that the event-mixing method describes the combinatorial background reasonably well. Panel *d* shows the remaining Λ peak in π^- Pb reactions after subtracting the background. Figure 3.17 shows

the Λ invariant mass spectrum reconstructed from π^- C reactions. The signal is

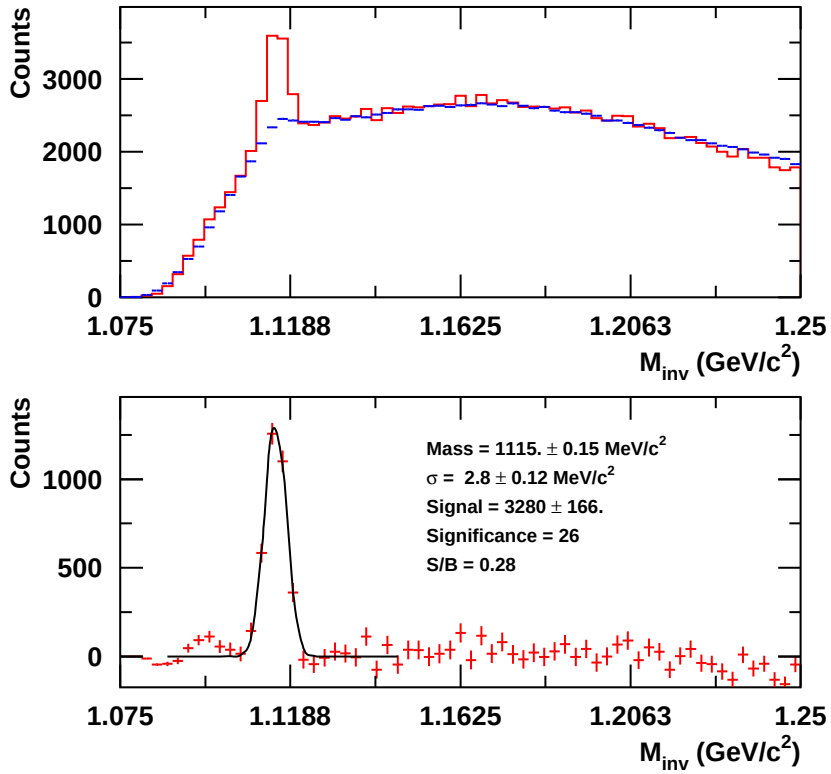

Figure 3.17: Λ invariant mass spectra reconstructed in $\pi^- +$ C reactions . The upper plot shows combinatorics spectrum (full line) and scaled event-mixing background on top of it, the lower plot shows the obtained Λ signal spectrum after subtraction.

characterized by a relatively low signal-over-background ($S/B \simeq 0.3$) and also a relatively small width of about $3\,\mathrm{MeV/c^2}$, this is due to the fact that the PLAWA has a good time resolution which is translated into a good momentum resolution of the proton.

Chapter 4

GEANT Simulation

A GEANT simulation of the detector is needed for efficiency estimations and is also used as a filter for models to compare them with experimental data, in order to see the effect of the detector response. Therefore, it is of great importance that the detector has to be described properly in GEANT. The first step is to implement properly the geometry of all sub-detectors, their volumes and their materials in GEANT, same holds for the target. This has been done during the upgrade of the FOPI detector in 1997. As a second step, the detector response has to be implemented in GEANT. It consists of the resolutions characterizing each sub-detector. In this our study is focused on the CDC sub-detector only. A short description of the CDC digitizer will be presented, then the implementation of the resolutions (i.e. spatial and energy resolution) will be explained. Comparisons of the CDC resolutions achieved in GEANT with DATA will be presented. Finally efficiency estimations for the S273 experiment are presented.

4.1 The CDC Digitizer

The role of a digitizer is to model detector response of deposited energy of a hit in the gas volume of the CDC and the propagation of the corresponding energy through the front-end electronic. Thereafter, these digitized charges are written into a file which have a similar format as experimental data file.
When tracking particles through matter with GEANT [106], the number of steps per track (i.e. distance between two hits is called step) inside the CDC volume of is calculated automatically by GEANT. While calculating the number of hits per track, all relevant physical processes like decay of the particle, electromagnetic interactions and hadronic interactions with the active volume have to be taken into account. The magnetic field has to be included for tracking particles inside the active volume of the CDC. After producing hits for each track inside the CDC,

the next step is to determine the equivalent charge for each hit. At each step the deposited energy is recorded inside the active volume of the CDC. In GEANT, the CDC electric drift field is replaced by an adjustable factor called the gain, the deposited energy per hit (which is the energy loss) in each drift cell (i.e. for each sense wire) is then multiplied by the gain factor. This is an easy way to simulate the effect of the potential voltage (see figure 2.6.
The distance between each hit and the closest drift cell in the (x,y) plane is calculated. Knowing the gas properties of the CDC and the applied electric drift field, the drift velocity can be derived. Thereafter the drift time of each hit is derived. After calculating the drift time and determining the relative hit position in (x,y) plane , it is necessary to have the fraction of energy of a hit left and right to the total energy, which has to be converted into charges. The fraction is given by the formula

$$\begin{aligned} R_L &= 0.5 \cdot \left(1 + 2 \cdot \frac{z_w - z_{\text{hit}}}{l_{\text{eff}}}\right) \equiv \frac{Q_L}{Q_L + Q_R} \\ R_R &= 0.5 \cdot \left(1 - 2 \cdot \frac{z_w - z_{\text{hit}}}{l_{\text{eff}}}\right) \equiv \frac{Q_R}{Q_L + Q_R}, \end{aligned} \tag{4.1}$$

where z_w is the middle of each wire, R_L and R_R are the fractions of charges left and right to the total charge and l_{eff} is the effective length of the wire. Both charges are converted into Gaussian-like signals given by

$$S_{L,R} = E \cdot R_{L,R} \left(\frac{1}{\sqrt{2\pi}\sigma} \cdot \exp\left(\frac{1}{2} \cdot \left(\frac{t_d - t_m}{\sigma}\right)^2\right)\right), \tag{4.2}$$

where $S_{L,R}$ are the collected signal from the left (L) and right (R) end of a wire which have to be digitized. t_d is the drift time corresponding to the distance between the hit and the drift cell, t_m is a mean drift time. σ is the width of the drift time distribution which is about 10 ns and E is the deposited energy per step for a hit. At this stage, one is able to digitize both charges using FADC with 100 MHz clock. The energy and spatial resolution are introduced at the level of the digitizer in the GEANT simulation. But before studying hit resolutions (spatial and energy resolutions), the relative distance of a hit to a drift cell has to be calculated. Also the gain factor has to be modeled properly to have the same effects which can be obtained with the potential wire voltage in the gas volume of the CDC.

4.2 Drift Path of a Hit

To study the track quality, it is important to have the proper drift distance of each hit in GEANT with respect to each drift cell. By definition a drift cell is a sense

wire surrounded by two potential wires both at a distance of 0.5 cm. Figure 4.1 shows a sketch of a drift cell in the (x,y) plane. Taking into account Lorentz angle α_L define the drift path in each drift cell is given by The drift path in each drift

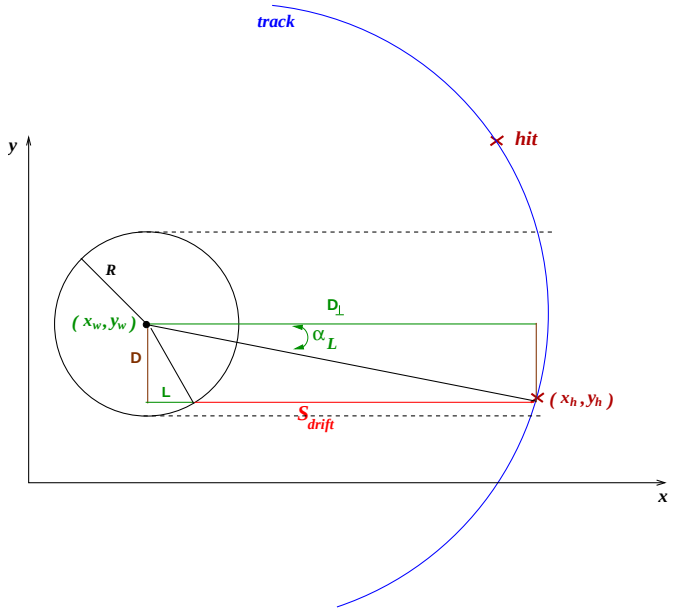

Figure 4.1: Sketch of the drift cell geometry.

cell is given by:

$$s_{\text{drift}} = D_{\perp} - L \tag{4.3}$$

The quantities s_{drift} , $D_{\perp}$ and L are shown in figure 4.1. $D_{\perp}$ is given by

$$D_{\perp} = \sqrt{(x_h - x_w)^2 + (y_h - y_w)^2} \cdot \cos\alpha_L \tag{4.4}$$

(x_h, y_h) is the hit position and x_w, y_w are the wire coordinate in the (x,y) plane. The distance L is given by

$$L = \sqrt{R^2 - D^2}, \tag{4.5}$$

and D is given by

$$D = \sqrt{(x_h - x_w)^2 + (y_h - y_w)^2} \cdot \sin\alpha_L \tag{4.6}$$

Thus if one knows the hit position, the wire position and the Lorentz angle, the drift path of each hit and the drift time can be derived properly.

4.3 Modeling of the Gain

It is a very complicated issue to simulate the transport of electrons inside a gas in a homogenous electric field. The situation becomes even more complicated if the electric field is inhomogeneous. As it was mentioned in the beginning, during the upgrade of the FOPI detector, CDC wires were exchanged from wires with 50 μm diameter to 25 μm diameter. The voltage divider chain responsible for producing an homogeneous electric drift field in each sector was also changed, which leads to an inhomogeneous electric field through the whole sectors. A schematic drawing of field cage of one CDC sector is shown in the right panel of figure 4.2 ([107]). The left panel illustrates the strength of the electric drift field at 3.7 cm far from the anode plane (i.e. the red crosses in the right panel represent the sense plane). It is no longer constant along the plane, it is growing as a function of the wire number and saturates close to the outer border of the sector. To be sure that we have a

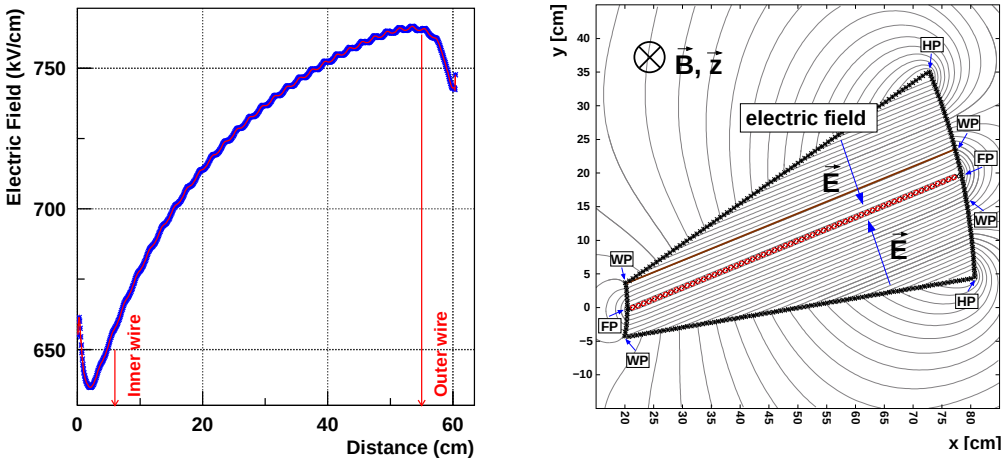

Figure 4.2: Left panel: Strength of electric drift field in one sector as a function of the radial distance. Right panel: Sketch of one sector where the field is calculated between two Warm Points (WP) connected by a line.

realistic description of the CDC with GEANT, one has to take into account this effect. As a first step, a linear dependence of the gain factor on the wire number was introduced for the wires $1-38$. It is given by

$$G_{\text{new}} = G_{\text{old}} \cdot (1 + (i_w - 19) \cdot 0.0245), \tag{4.7}$$

where G_{new} is the new Gain, G_{old} is the old Gain and i_w is the wire number.

After introducing this effect it is mandatory to adjust the detector response (i.e. the energy and spatial resolutions) in GEANT.

4.4 Energy and z Resolutions of a Hit

The energy deposited by a hit and its position along the z axis are correlated. The energy of the hit is the sum of the collected charges Q_L and Q_R given by the formula

$$E = Q_L + Q_R, \tag{4.8}$$

and its z position after digitization is given by

$$z = \frac{Q_L - Q_R}{Q_L + Q_R} \tag{4.9}$$

Therfore also the resolutions of those quantities are correlated. The aim of this simulation is to reproduce the detector resolutions achieved after the upgrade of the detector. The resolutions of the S261 experiment are shown in figure 4.3. The upper left panel depicts the energy resolution per track as a function of its deposited energy . For MIPs which correspond to $\Delta E \approx 1000$ the energy resolution is about 45 %. The upper right panel shows position resolution of hits along the z axis as a function of their deposited energy. For MIPs it has a resolution of $\sigma_z \approx 7\,\text{cm}$. The lower panels show the z and energy resolutions as functions of the azimuthal angle ϕ for pions at MIPs. One can see that those resolutions are constant over all sectors of the CDC.

Formula (4.10) shows the dependence of σ_z on $\sigma_{\Delta E}/\Delta E$

$$\sigma_z/z = \frac{2 \cdot Q_L}{|Q_L - Q_R|} \cdot \sigma_{\Delta E}/E \tag{4.10}$$

which means that if one introduce a smearing of the energy E around its nominal value, this will automatically introduce a smearing of the z coordinate.

We start by smearing the energy around its nominal value and try to reproduce the experimental data, taking into account the correlation mentioned above. The smearing was parameterized as follows

$$E_{\text{new}}(L,R) = (a+1) \cdot E_{\text{old}} + b(L,R) \cdot \sqrt{E_{\text{old}}}. \tag{4.11}$$

This parameterization has been introduced for each drift cell. $E_{\text{new}}(L,R)$ is the new energy signal obtained after smearing left and right on a wire. The adjustable parameter a is taken from a normal distribution with a mean at zero and with a standard deviation of 0.15. The other parameter b is also taken from a normal

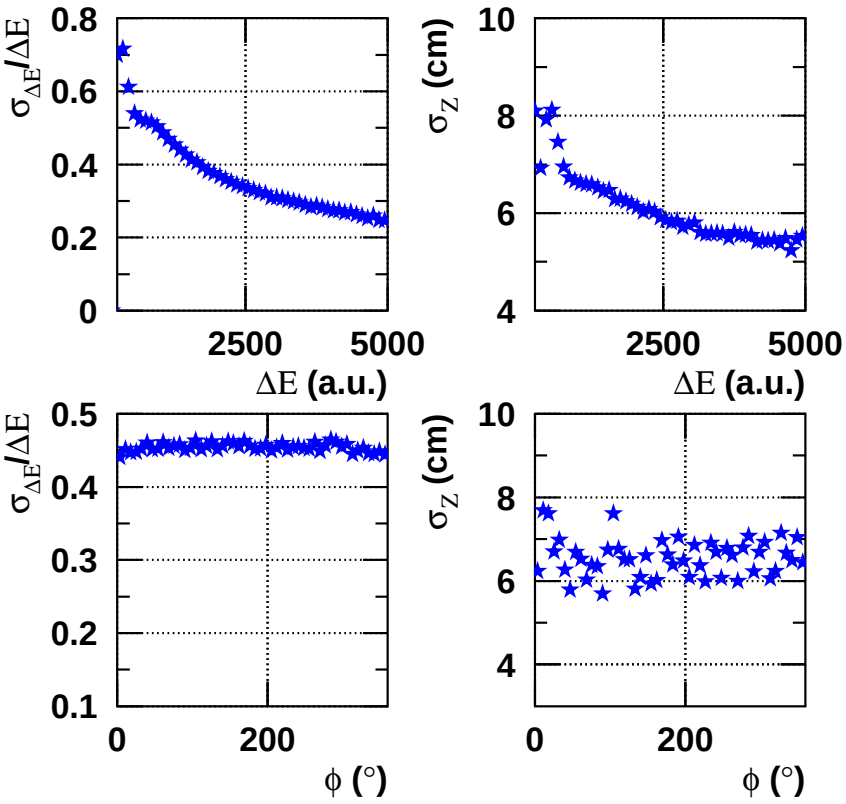

Figure 4.3: Upper plots: Energy and z resolutions of tracks in the CDC as a function of the deposited energy ΔE. Lower plots: Energy and z resolutions of pions at MIPs as a functions of their azimuthal angle ϕ.

distribution but with a standard deviation of 0.6, and has a left-right dependence with respect to the longitudinal center coordinate of each wire. The energy resolution is governed by the parameter a, because the energy is just the sum of the collected charges left and right after digitization. Contrary to that, the z resolution is governed by the b parameter because the z position of hit after digitization is proportional to the difference between charge left and right (see formula (4.9)). With this parameterization the energy resolution is given by

$$\Delta E/E = a + (b(L) + b(R)) \cdot \frac{1}{\sqrt{E_{\text{old}}}}, \tag{4.12}$$

and the z resolution $\sigma_z \equiv \Delta z$ is given by

$$\Delta z = \frac{2 \cdot Q_L \cdot a}{E_{\text{old}}} + 2 \cdot Q_L \cdot \frac{b(L) + b(R)}{E_{\text{old}}^{2/3}}. \tag{4.13}$$

In formula (4.2) the energy E is replaced now by $E_{\text{new}}(L,R)$, and this is the signal which will be digitized by the FADC.

The obtained results from simulation are plotted in red in the left panel of figure 4.4, the blue symbols denote the resolutions from data. The trend of $\sigma_{\Delta E}/\Delta E$ can not be reproduced fully. Only below $\Delta E = 2000$ it seems that the trend has the same behavior as in data, above 2000 the data still shows a decreasing of the energy resolution while in GEANT the resolution looks roughly constant with increasing energy. The right panel of figure 4.4 shows the energy resolution over all sectors. Data show a worse energy resolution than GEANT by factor 2.

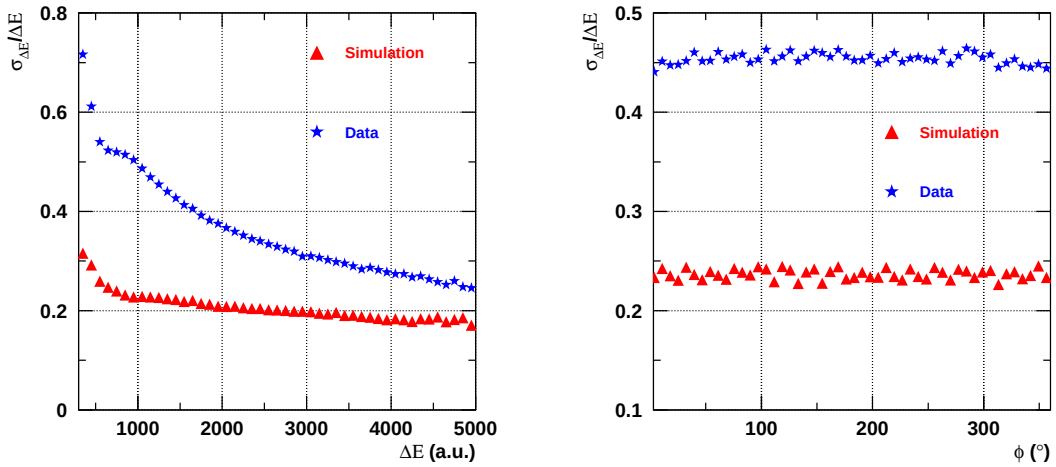

Figure 4.4: Comparison of the energy resolution between data (red stars) and GEANT (blue triangle). Left panel: The energy resolution $\sigma_{\Delta E}/\Delta E$ as a function of the deposited energy ΔE. Right panel: The $\sigma_{\Delta E}/\Delta E$ as a function of the azimuthal angle ϕ for pions at MIPs.

The trend of the z resolution is reproduced as in the data, left panel of figure 4.5 depicts the comparison between data and GEANT, the resolution is worse in GEANT by a factor of $20-25$ % as it is shown in the right panel. There are no clear reasons for the discrepancies between data and GEANT. One possibility is that the energy loss distributions of hits in a drift cell is not modeled properly in

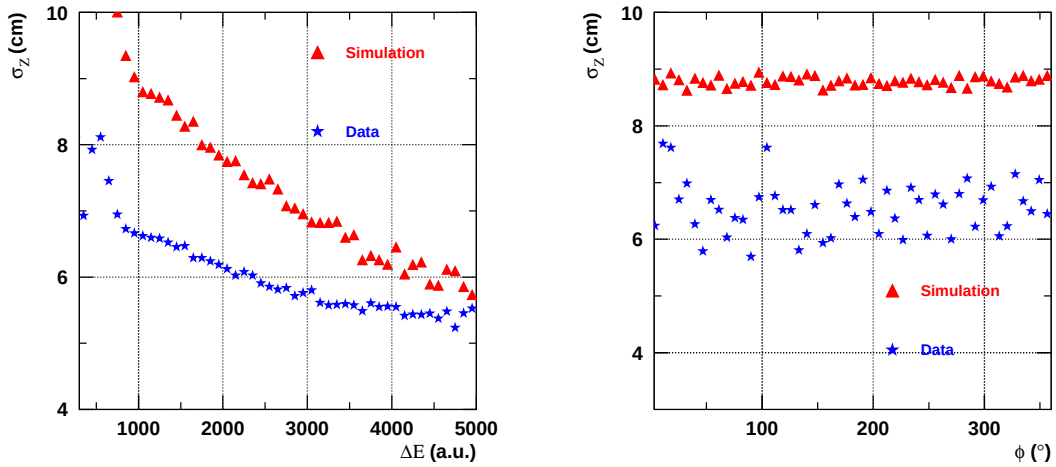

Figure 4.5: A comparison of the z resolution (σ_z in cm) between data (red stars) and GEANT (blue triangles) as function of the deposited energy ΔE and the azimuthal angle ϕ.

GEANT, the same may be true for the z resolution since the resolutions are correlated. Even though both resolutions in GEANT do not match with experimental ones, observables characterizing particles (like: their masses, hit multiplicity, distance to the primary vertex, mass resolution of reconstructed resonances) can be described reasonably by the simulation.

4.5 Position Resolution of Hits in the (x,y) Plane

In the (x,y) plane the position of a hit is given by equation (2.5). The resolution on the (x,y) position of the hit is mainly due to the time resolution of the electronics. A time resolution of 10 ns was introduced in GEANT while integrating charges left and right. With a drift velocity of $4\,\mathrm{cm}/\mu\mathrm{s}$ and a time resolution of $\sigma = 10\,\mathrm{ns}$ the obtained (x,y) resolution $\sigma_{xy} := v \cdot \sigma_t = 400\ \mu m$. The comparison between the obtained (x,y) resolution σ_{xy} in GEANT and experimental data is shown in figure 4.6. The left panel shows the comparison of σ_{xy} as function of the energy, the trend of the distribution in GEANT looks very similar as the one of the experimental data, right panel shows that the resolution is constant over all CDC sectors and it is about $400\,\mu\mathrm{m}$.

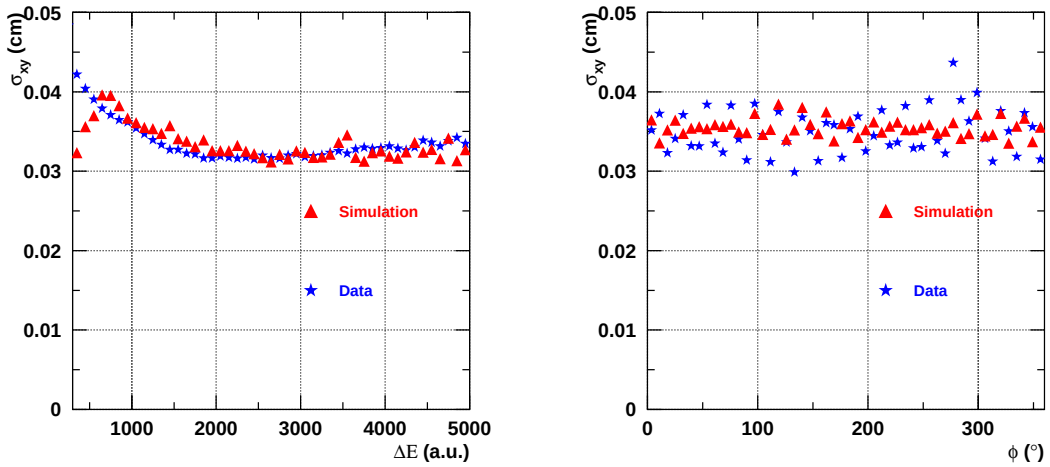

Figure 4.6: A comparison of the σ_{xy} resolution (in cm) between data (red stars) and GEANT (blue triangles) as function of the deposited energy ΔE (left panel) and as a function of the azimuthal angle (right panel).

4.6 Momentum Resolution

The total momentum of charged particles measured via their curvature in the CDC is given by

$$p = \frac{0.3 \cdot z \cdot B}{k \cdot \sin\theta}(GeV/c), \tag{4.14}$$

k is the inverse curvature radius of a track (in $1/m$), θ is the deflection angle in the (r,z) plane, z is the charge and B is the magnetic field in Tesla.

The error of the momentum p is arising from the errors of the measured quantities k and θ. The error of the curvature k, has two independent contributions, one coming from the multiple scattering $(\delta k)_{\text{ms}}$, the other one $(\delta k)_{\text{res}}$ is due to the track resolution in the (x,y) plane. The error of the curvature is then given by

$$(\delta k)^2 = (\delta k)^2_{\text{res}} + (\delta k)^2_{\text{ms}}. \tag{4.15}$$

If a track of N points equally distributed over a length L in the (x,y) plane is measured (assuming that all points have the same position resolution σ_{xy}), the momentum resolution is given by [98]

$$\frac{\sigma_{p_t}}{p_t} = \frac{\sigma_{xy} \cdot p_t}{0.3 \cdot B \cdot L^2} \cdot \sqrt{\frac{720}{N+4}}, \tag{4.16}$$

and the resolution due to multiple scattering is [108]

$$\frac{\sigma_{p_t}}{p_t} = \frac{0.05}{B \cdot L} \cdot \sqrt{\frac{1.43 \cdot L}{X_0}}, \tag{4.17}$$

where X_0 is the average radiation length (in m) of the material traversed by the particle.

Two errors contribute to the measurement of the polar angle, one is the error of the z-coordinates σ_z of N points measured along the track of a length L. The error is given by

$$(\sigma_\theta)_{\text{res}} = \frac{\sigma_z}{L} \cdot \sqrt{\frac{12(N-1)}{N(N+1)}}. \tag{4.18}$$

The other error comes from the multiple scattering and is given by

$$(\sigma_\theta)_{\text{ms}} = \frac{0.015}{\sqrt{3} \cdot p} \cdot \sqrt{\frac{L}{X_0}}, \tag{4.19}$$

where p is the momentum (in GeV/c).

The total momentum resolution is the sum of the two contributions (see equations (4.16, 4.17)), a constant one due to the multiple scattering and other one proportional to the momentum due to the track resolution in space. The transverse momentum resolution measured in the CDC is shown in figure 4.7 as a function of the transverse momentum of charged particles.

Below a transverse momenta of $0.2\,\text{GeV}/c$ the transverse momentum resolution is governed by the multiple scattering and the measured σ_{p_t}/p_t points scatter around 8%. Above p_t of $0.2\,\text{GeV}/c$ the momentum resolution is governed by the track position resolution in the (x,y) plane and it has a linear dependence on p_t (see formula (4.16) as it is shown by the fit of the points in figure 4.7.

4.7 Efficiency Evaluation

Since the spatial and energy resolutions are fixed in GEANT, the next step is to compare differential distributions of the cut quantities used for K^0_S and Λ invariant mass reconstructions. It is important to ensure that the obtained distributions describing particle properties (mass, momentum, distance to vertex ...) in GEANT agree to those of the experimental data.

4.7.1 Global Efficiency Estimation

The global efficiency will be used to derive the yields of K^0_S in five targets and hence to derive the K^0 production cross section. In order to evaluate the efficiency

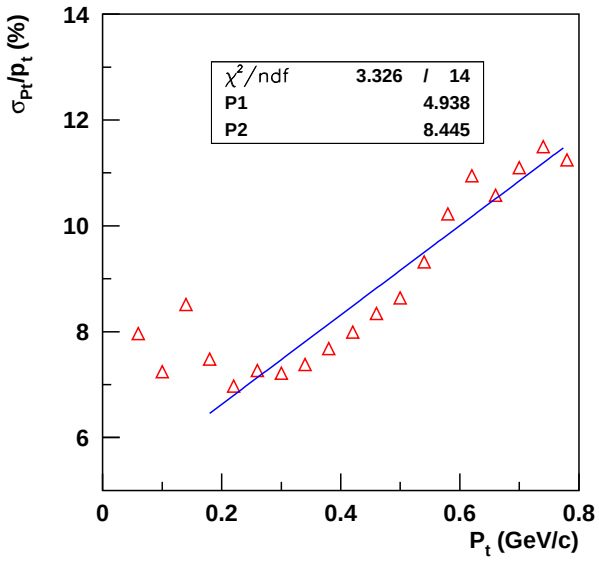

Figure 4.7: Transverse momentum resolution as a function of the transverse momentum. The blue line is the fit in the momentum range above $0.2\,\mathrm{GeV/c}$.

in this case, we are in a need of transport model calculations where reactions such as $\pi + N \rightarrow K + Y$ (i.e. K: K^+ or K^0 and Y: Σ or a Λ) inside the nuclear medium can be described properly. There are two transport models available which describe those reaction inside a nuclear medium at SIS energies. The first one is called "Isospin Quantum Molecular Dynamics" (IQMD) [109, 110] and the other one is called "Hadron String Dynamics" (HSD) [52, 46]. For global efficiency estimations the IQMD model is used in this work. We propagate the IQMD input events of the two reactions $\pi^- + Pb$ and $\pi^- + C$ through GEANT. Experimental conditions have to be taken into account, for example the spread of the π^- beam (see figure 3.1. The original vertex in the (x,y) plane of the IQMD input events was smeared like in the experimental data. Kinematical variables (four momentum), dynamical variables (production probability of particles) and vertices of particles are always saved in data base structure called the KINE bank while propagating the particles through the detector.

By definition, a global efficiency (i.e. reconstruction efficiency) is the number of detected or reconstructed particles in the detector acceptance divided by the original number stored in the KINE bank. To determine a realistic efficiency the kinematical variables (i.e. phase space distributions) of different particle species

should agree with the one from data under the same conditions. Before we compare the phase space distributions of the K_S^0 between data and simulation, we first do the comparison for the daughters (π^-,π^+) of the K_S^0 without using any cuts. We compare fundamental observables which characterize each particle. This comparison is shown in figure 4.8. Observables from the data are plotted in blue and the corresponding ones from simulation are plotted in red. The z_0 distributions for both particles differ slightly between simulation and data , there is a shift in the mean of the distributions and their width is larger than in the data. Fitting these distributions with a Gaussian will give a 24 % difference of the width between data and simulation. It is due to the z resolution which was worse in the simulation by $20-25$ % than in the data.

Nice agreement between data and simulation can be seen for the transverse momentum p_t distributions. For the π^+, the maximum of its p_t distribution in the simulation shows a higher yield than in the data. The mass distributions of π^- particles from the simulation agree well with the data, even the maxima of both distributions are at the same mass ($0.12\,\mathrm{GeV/c^2}$). The mass distribution of π^+ particles in the simulation is shifted to lower masses in comparison to the one of the data by about 25 %. The shift can be understood by the fact that the energy loss in the simulation is not modeled perfectly and also the resolution on the energy loss in the simulation is better. A good agreement can be seen for the d_0 distributions of both particles π^- and π^+ . This is due to the fact that there is good agreement of the (x,y) resolution between data and simulation. The hit multiplicity distribution for π^- particles from simulation agrees nicely with the data. Distributions of hit multiplicity for the π^+ particles show a good agreement up to a hit multiplicity of 50 where data show less hits per track than simulation which is about 56. This is due to a track finding inefficiencies in the experiment close to a sector border.

After those comparisons, it is clear that the quantities characterizing π^- and π^+ particles in the simulation have distributions which are close to the ones of the data. Therfore, it is safe to cut on variables that are well described in the simulation as in the data. Figure 4.9 shows the invariant mass spectra of reconstructed K_S^0 for the lead target in the right panel and from the carbon target in the left panel. Those spectra are obtained by applying the same method and steps as for the data (see section 3.4). The mass peak and its width are obtained using a Gaussian fit to the invariant mass spectrum. In table 4.1 is a comparison between data and simulation for the carbon and lead targets. Mass resolutions of the K_S^0 agree well between data and simulation as well as for the two different targets.

It is important to emphasize that under the cuts used for the evaluations of the invariant mass spectra, also the phase-space distributions of the K_S^0 particles in the simulation should be comparable to the one of data. Figure 4.10 illustrates

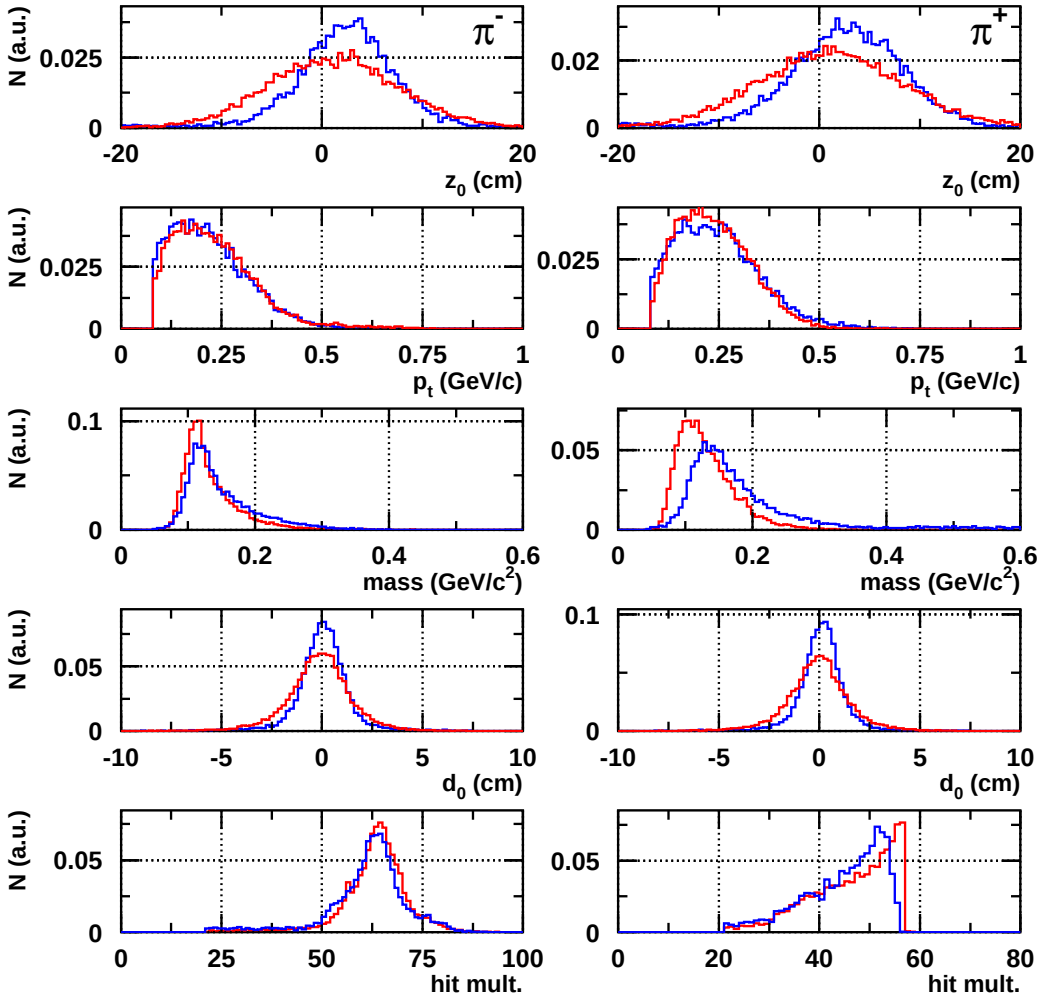

Figure 4.8: A comparison of observables characterizing π^- and π^+ (daughters of K^0_S) between data (blue) and simulation (red). All histograms are normalized to the number of entries.

a comparison between data and simulation for the kinematical quantities which describe the phase-space of K^0_S produced in the lead target. The upper left panel shows the transverse flight paths of the K^0_S, the red distribution is obtained from simulation, the blue one from data. Both distributions show a nice agreement, only at the lowest bin for r_s data show a slightly higher yield than simulation. The transverse momentum p_t spectrum is plotted in the upper right panel. At low momentum below $250\,\mathrm{MeV/c}$ the data show a higher yield than simulation and

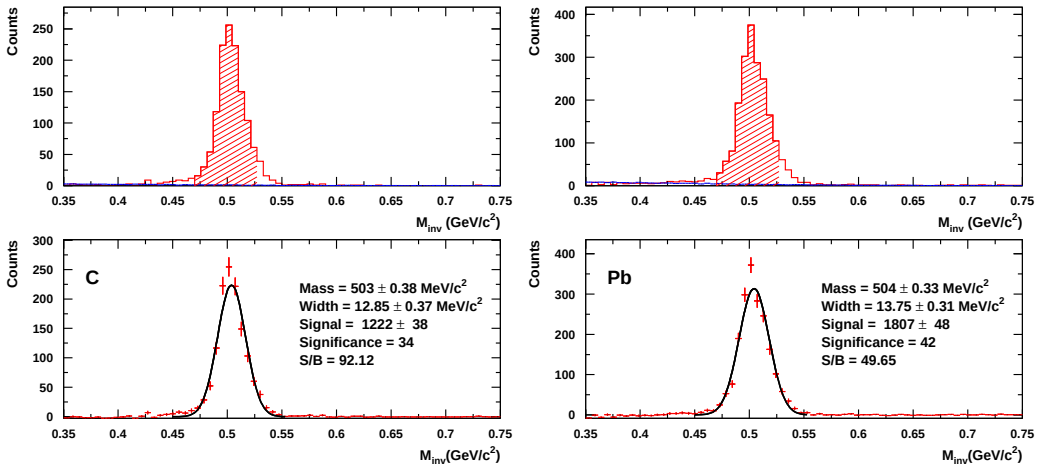

Figure 4.9: K^0_S invariant mass spectra obtained in π^- + C(left) and π^- + Pb (right) reactions, using IQMD.

Target	Mass $(\mathrm{MeV/c^2})$	$\sigma(\mathrm{MeV/c^2})$
C (data)	505 ± 0.40	12.80 ± 0.40
C (simulation)	503 ± 0.40	12.58 ± 0.40
Pb (data)	505 ± 0.04	13.50 ± 0.40
Pb (simulation)	504 ± 0.33	13.75 ± 0.31

Table 4.1: A comparison between the K^0_S masses and widths obtained in data and simulation.

above $250\,\mathrm{MeV/c}$ one can see the opposite. The lower plot shows the distributions of the rapidity y (see appendix B). There is a slight difference between the two distributions. In the forward hemisphere (i.e. target rapidity is at $y_{\mathrm{lab}} = 0$) at rapidity about 0.5 the data show less yield than in the simulation. The obtained global efficiencies from lead and carbon targets are listed in table 4.2. In the global efficiency evaluation, the branching ratio and also the fact that we can detect with FOPI detector only K^0_S are taken into account.

4.7.2 Local Efficiency Evaluation

To derive an inclusive differential cross section $\mathrm{d}\sigma/\mathrm{d}y$ of K^0 in 4π model independently, the inclusive invariant cross section $E \cdot \mathrm{d}^3\sigma/\mathrm{d}^3p$ in 4π has to be evaluated

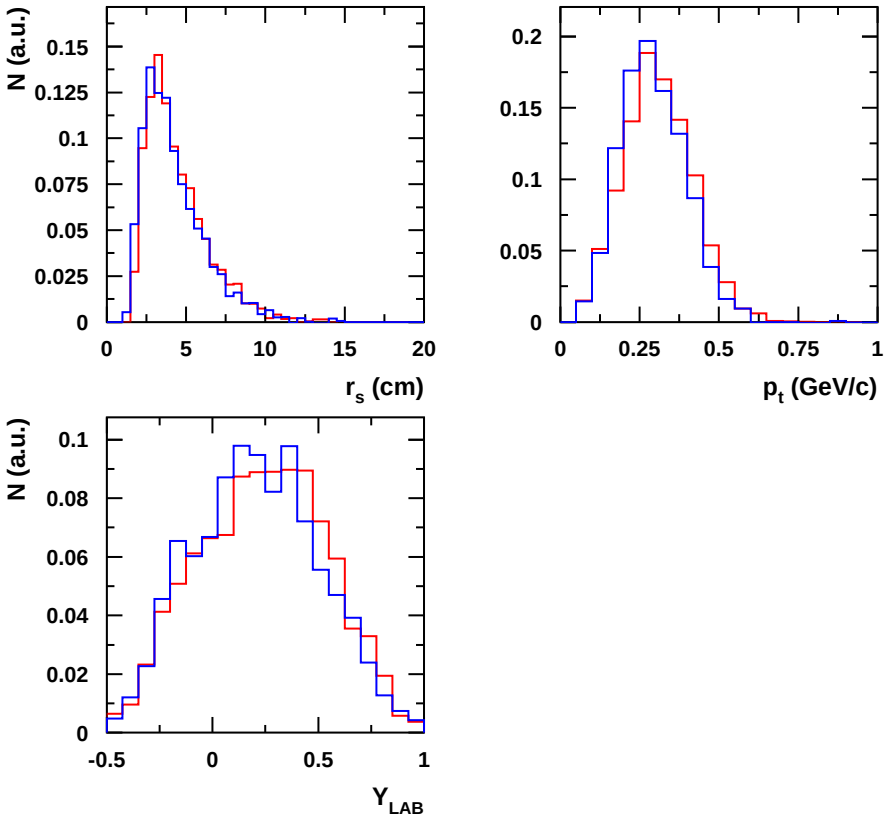

Figure 4.10: A comparison of the kinematical variables characterizing K_S^0 between data (blue) and simulation(red). All histograms are normalized to the number of entries.

Target	**Number of recons.** K_S^0	**Number of** K_S^0 **in KINE**	**Efficiency** in %
C	1150	61 820	0.93
Pb	1020	50 999	1.00

Table 4.2: The obtained efficiencies in % in Carbon and Lead targets.

model independently first (see appendix B). To obtain differential observables in 4π, the efficiency correction is applied which has to be differential also. Therefore, K_S^0 were generated randomly in phase space using GEANT simulation, with rapidities y varying between -1 and $+1$ and transverse momentum spectra from 0 to $1\,\mathrm{GeV/c}$. We derive the reconstructed K_S^0 in the CDC acceptance in 4 bins

of rapidity (y range from -0.6 to 1.0) as function of the transverse momentum p_t. Figure 4.11 illustrates the $d^2\sigma/(p_t \cdot dp_t \cdot dy)$ distribution of K^0_S for one bin of rapidity. The red symbols are the input K^0_S distribution in GEANT and the blue symbols represent the reconstructed distribution.

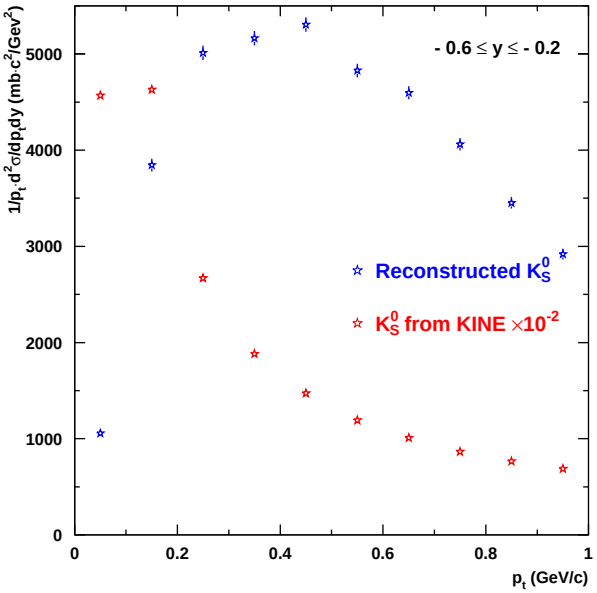

Figure 4.11: Comparison of the invariant K^0_S cross section between KINE and reconstructed data.

The differential efficiency is the ratio of the reconstructed distribution to the input one. The result for all rapidity bins is depicted in figure 4.12.

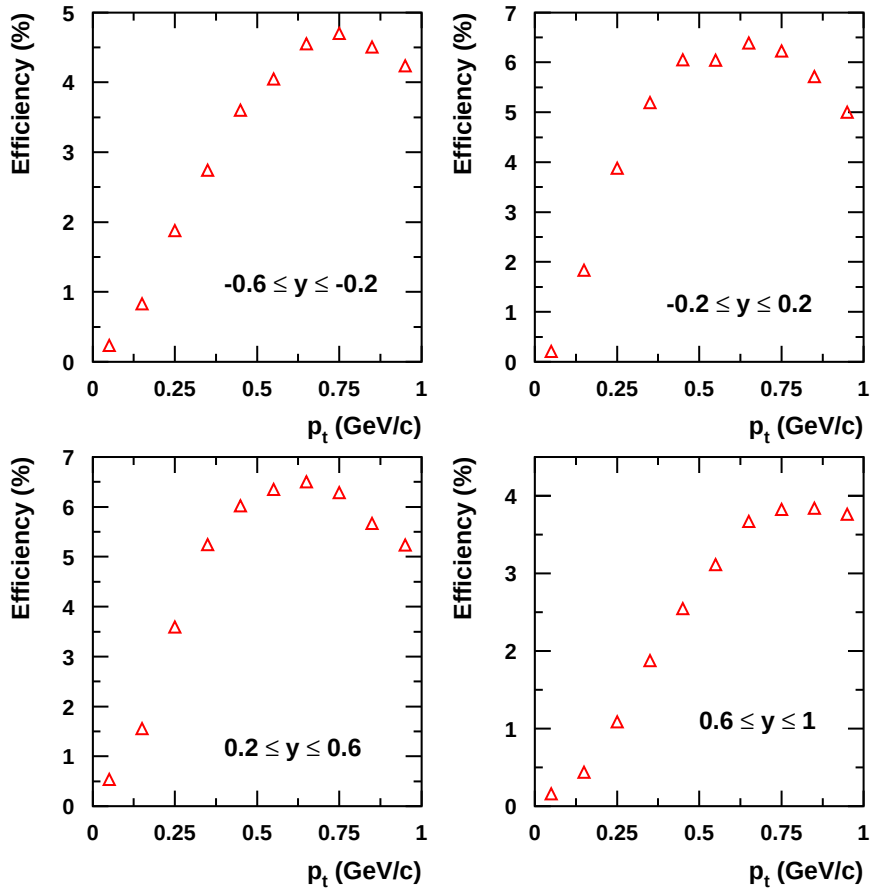

Figure 4.12: The obtained efficiency in % in different rapidity bins as function of p_t.

Chapter 5

Experimental results: Inclusive Spectra of K^0

This chapter summarizes inclusive K^0 phase-space distributions in the CDC acceptance. Since the number of reconstructed K^0_S is low for Copper, Aluminum and Tin, results will only be shown for the two systems πC and πPb. The application of local efficiency corrections to the spectra leads to the invariant cross section $\mathrm{d}^2\sigma/(2\pi p_t \mathrm{d}p_t \mathrm{d}y)$ as a function of p_t in different rapidity bins. Differential and absolute inclusive K^0 production cross sections will be presented as well as their dependence on the mass of the nucleus. Comparison of inclusive Λ phase space distributions produced in $\pi^- + Pb$ with the ones produced in $\pi^- + C$ are also presented.

5.1 K^0_S Phase-Space Distributions

As mentioned in chapter 3, the K^0_S were reconstructed in the CDC only. The study of the production mechanism of K^0 in pion-induced reactions depends on two physical variables: The amplitude (contains all dynamical variables, also called matrix element) and the available phase space (sometimes called the density of final states, contains only kinematical information).

Figure 5.1 illustrates the comparison between the phase space of K^0_S produced in $\pi^- + C$ and the one produced in $\pi^- + Pb$. In the upper plots, the transverse momentum of K^0_S is plotted versus the rapidity. The color code indicates the number of K^0_S per (p_t, y) bin. Full lines indicate the CDC geometrical acceptance. One can clearly see that roughly 15% of the K^0_S are reconstructed outside the CDC acceptance. This is due to the fact that the daughter particles (π^-, π^+) of the decaying K^0_S are detected inside the CDC. This effect can be seen in the backward and forward hemisphere of the FOPI detector.

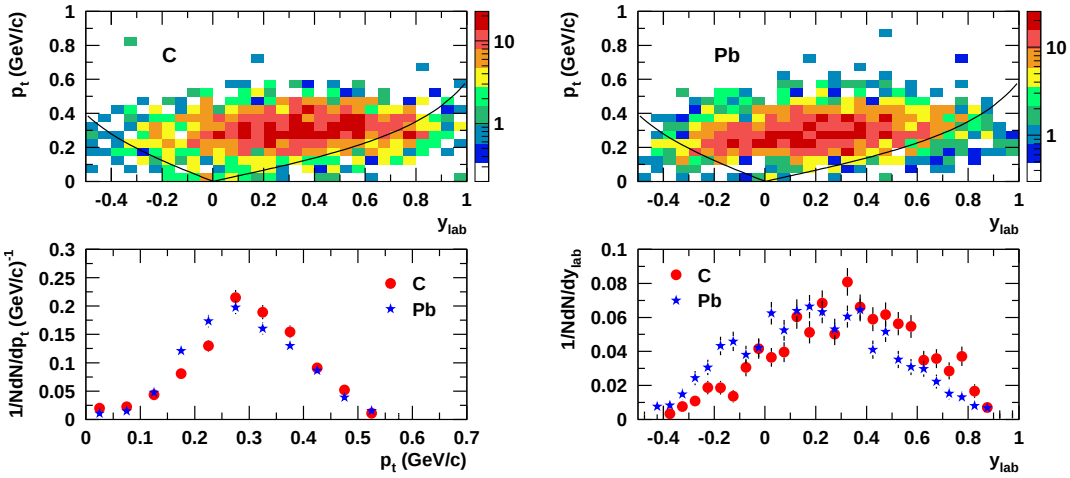

Figure 5.1: Upper panels: Comparison of the K^0_S phase-space (p_t and y_{lab}) distributions between C and Pb in the CDC acceptance. Black lines show the CDC's geometrical acceptance limits. Lower panels: Comparison of normalized p_t and y_{lab} distributions between Lead and Carbon in the CDC acceptance. All plots are not efficiency corrected. As a reference the rapidity of the (π^-, N) pair is 0.61.

Regarding the color code in case of the Carbon, it becomes clear that a substantial fraction of the K^0_S is produced at rapidities y beyond 0.5 (target rapidity is at $y = 0$). K^0_S produced in $\pi^- + Pb$ mainly populate the phase-space at rapidities below 0.4, in comparison to the ones produced in $\pi^- + C$. The lower panels of figure 5.1 show the p_t spectra and y_{lab} distributions of both systems. Red symbols (circles) denote Carbon data, blue symbols (stars) are for Lead. At p_t below 200 MeV/c, the K^0_S from Lead exhibit higher yield that those from carbon. At p_t above 200 MeV/c, the K^0_S yield for Carbon is slightly higher than the one for Lead. The lower right panel shows a comparison of the K^0_S rapidity distributions between from $\pi^- + Pb$ and $\pi^- + C$. At rapidities above 0.25, the number of K^0_S produced in $\pi^- + C$ is slightly higher than the one in $\pi^- + Pb$. The two distributions overlap around 0.2. Below 0.25, the K^0_S yield in $\pi^- + Pb$ becomes slightly higher than in the Carbon. One of the reasons for this behaviour is that the K^0_S produced in a Lead nucleus are confronted to more nucleons and thus will suffer more scattering compared to the ones produced in a Carbon nucleus.

5.2 K^0 Invariant Production Cross Section

The K^0 yield in different (p_t, y) bins can be described by the invariant production cross section $\mathrm{d}^2\sigma/(2\pi p_t \mathrm{d}p_t \mathrm{d}y)$ (see appendix B). To obtain this observable, p_t spectra of K^0_S in different rapidity bins for both targets (Carbon and Lead) have to be efficiency corrected (see figure 4.12 for the efficiency spectra) and normalized to the number of beam particles (see table 3.1).

The results are compiled in figure 5.2. It illustrates the invariant production cross section of K^0 as a function of p_t for four rapidity bins. The upper left panel, shows the K^0 invariant cross section in the rapidity range corresponding to the backward hemisphere. The upper right panel shows the same observable around target rapidity. The K^0 invariant cross section in the forward hemisphere is shown in the two lower panels. Red symbols (circles) represent K^0 produced in the Carbon target, blue ones (stars) are for the Lead target. Starting from the backward hemisphere, one can see that no K^0 are produced with p_t above 500 MeV/c in the case of the Carbon target due to kinematical limits. For the Lead target, it is possible to have K^0 with momenta above 500 MeV/c but due to the huge error bars on the invariant cross section (i.e. relative errors of 113%) this data point is not shown. Below 100 MeV/c the error bars on the K^0 invariant cross section are big (relative error is about 93 %) due to low statistics of K^0 in this part of the phase space (see figure 5.1). For the Carbon target the relative errors exceed 115 %, therefore this data point was removed as well.

Around target rapidity and up to $y \sim 0.6$, K^0 with momenta above 500 MeV/c are produced with both target with reasonable statistics. Both distributions become flat in comparison to the one in the previous plot. At rapidities above 0.6, no K^0 are produced in both targets at low momenta (i.e. below 100 MeV/c) and also above 500 MeV/c due to the kinematical limits. For momenta above 500 MeV/c no K^0 can be produced in this region of the phase space.

Concerning the yield of K^0, it is clear that the absolute number of K^0 produced in π^- Pb reactions is bigger than the one produced in $\pi^- + C$ reactions over all phase space. At rapidities below -0.2, the K^0 yield in the Lead is roughly one order of magnitude bigger than the one in Carbon. Around target rapidity the number of K^0 produced in Carbon is rising for all momenta. From backward to forward hemisphere the absolute number of K^0 in the Carbon is multiplied by roughly factor three at momenta below 300 MeV/c. The absolute number of K^0 produced in the Lead target is increasing, when going from the backward hemisphere to rapidities of 0.6. Above 0.6 the yield decreases for all momenta. While in Carbon target, the K^0 yield shows a constant increase from backward to forward hemisphere. This behaviour of the yield as a function of the system size can be assigned to the rescattering of kaons inside the nucleus.

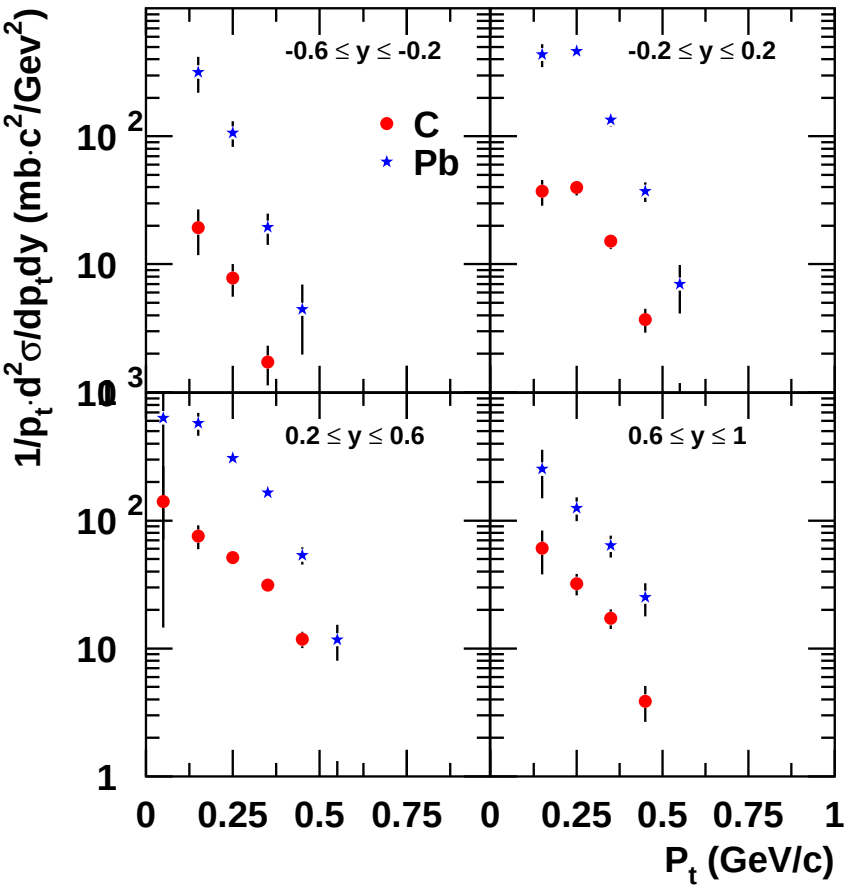

Figure 5.2: K^0 invariant cross section as function of p_t for four rapidity bins. Red circles and blue stars represent the K^0 invariant cross section produced in $\pi^- + C$ and $\pi^- + Pb$ reactions respectively

5.3 K^0 Rapidity Distributions

The additional variable which describe the K^0 phase-space description (in addition to the transverse momentum spectra) (see figure 5.2) is the rapidity distribution. It can be derived from the invariant cross section as follows

$$\frac{\mathrm{d}\sigma}{\mathrm{d}y} = \int_0^\infty \frac{\mathrm{d}^2\sigma}{2\pi p_t \mathrm{d}p_t \mathrm{d}y} \mathrm{d}p_t \quad . \tag{5.1}$$

In order to evaluate this integral one needs to know the analytical expression for $d^2\sigma/p_t dp_t\, dy$ as a function of p_t which is impossible. The other method is to derive the quantity $d^2N/dp_t dy$ as function of p_t for the four rapidity bins. Thereafter, the obtained spectra are corrected by the efficiency taking into account the normalization by the number of beam particles number. At the end the $d^2\sigma/dp_t dy$ distribution is integrated numerically in each rapidity bin for all p_t to obtain $d\sigma/dy$. The results are plotted in figure 5.3.

Kaons produced in elementary reactions ($\pi^- + p \rightarrow K^0 + \Sigma^0(\Lambda)$), have a $d\sigma/dy$ distribution limited to $y \sim 1$ in the forward hemisphere and to $y = 0$ in the backward hemisphere.
The left panel shows $d\sigma/dy$ for K^0 produced in the Carbon target as a function of their rapidity. One can see that the maximum of the distribution is reached at a rapidity around 0.4. The distribution shows a rise of the yield of K^0 going from negative to positive rapidities. This distribution illustrates that most of the K^0 are produced in the forward hemisphere. In the backward hemisphere, kaons with rapidities below 0 are also being produced, but if one extrapolates the distribution to lower rapidities, one can not go below -1.

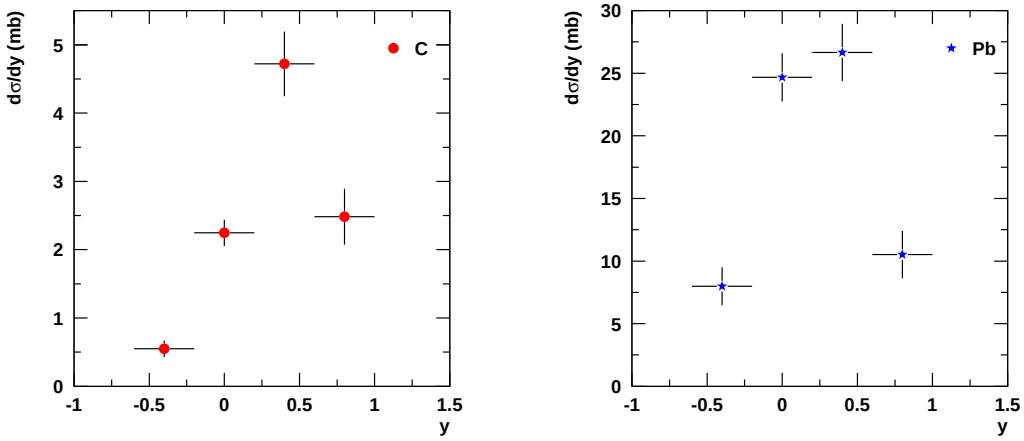

Figure 5.3: Rapidity distributions (in mb) of K^0 produced in Carbon (left panel) and Lead (right panel) targets.

The right panel depicts the $d\sigma/dy$ distribution for K^0 produced in Lead the target as a function of the rapidity. The distribution also has a maximum at rapidity $y \sim 0.4$. It is clear that more kaons are produced in the forward hemisphere than in the backward one. Below target rapidity, clearly more K^0 are produced in this region of the phase-space in comparison to the Carbon target. If one extrapoltaes to lower rapidities the $d\sigma/dy$ distribution does not exceed a rapidity of -1.

A comparison of the distributions $d\sigma/dy$ of K^0 between Lead and Carbon is shown in figure 5.4. Both distributions are normalized to the total sum of K^0 over all rapidity bins without extrapolating to the phase-space limits. The number of K^0 produced in Lead target is bigger than the one from Carbon in the backward hemisphere. Both distributions have a maximum at rapidity of 0.4 and the absolute number of K^0 from the Carbon target is bigger than the one from Lead in the forward hemisphere.

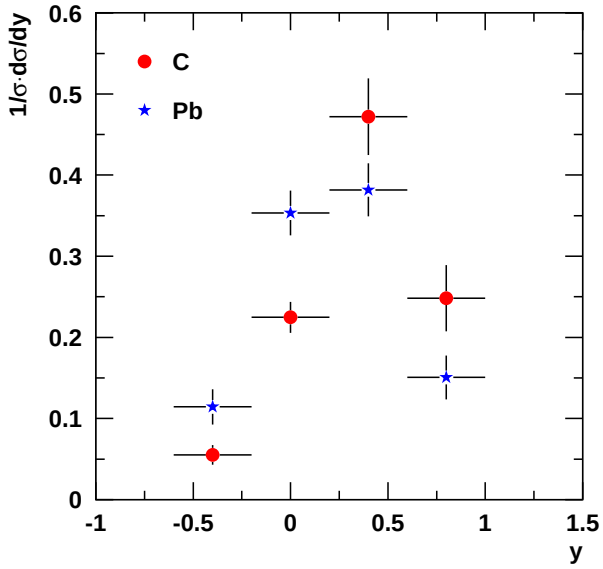

Figure 5.4: A comparison of the normalized rapidity distributions between K^0 produced in Lead (blue stars) and Carbon (red circles).

5.4 The K^0 Inclusive Cross Section

The main goal of this experiment is to measure the K^0 inclusive cross section in $\pi^- + A \rightarrow K^0 + X$ reaction in different nuclei. To study its behaviour as a function of the system size, five different targets are chosen with a nuclear mass varying from Carbon ($A = 12$) up to Lead ($A = 208$). In between Aluminum ($A = 27$), Copper ($A = 64$) and Tin ($A = 118$) targets are used.
The K^0 production cross section is given by (2.15), but to measure it in 4π one has to apply an efficiency correction. Therefore the K^0 production cross section can

be written as follows

$$\sigma_R(\pi^- + A \rightarrow K^0 + X) = \frac{N_{K^0}}{N_{\text{inh}} \cdot P \cdot \varepsilon} \quad , \tag{5.2}$$

where ε is the total efficiency. In the FOPI detector we are able to reconstruct K^0_S only (i.e. due to their small life time, they decay inside the FOPI detector, which is not the case for the K^0_L). Thus, the number of reconstructed K^0_S is multiplied by a factor two for all targets. This has been taken into account when evaluating the efficiency ε (see table 4.2). The number of reconstructed K^0_S in all targets is presented in table 5.1. Roughly the same number of reconstructed K^0_S is registered for both targets Carbon and Lead. For the other targets, about one order of magnitude K^0_S less can be reconstructed. Due to the lack of IQMD simulations, the

Target	**No. of reconstr.** K^0_S	σ_R **(mb)**	$\sigma'_R = \int \frac{d\sigma}{dy}$ **(mb)**
C	1303	4.14 ± 0.26	4.00 ± 0.26
Al	126	7.08 ± 0.88	
Cu	280	13.60 ± 1.29	
Sn	140	20.41 ± 2.44	
Pb	1495	27.25 ± 1.68	27.93 ± 1.53

Table 5.1: The number of reconstructed K^0_S for all targets and the corresponding cross sections σ_R. σ'_Rs are obtained by integrating numerically both distributions in figure 5.3. The error bars on σ_R and σ'_R are statistical only.

same efficiency correction for Al, Cu, and Sn was used as for Carbon to evaluate the K^0 inclusive cross section. Using the interaction probability P for each target from table 2.1 and the number of beam particles N_{inh} from table 3.1. The obtained K^0 inclusive cross sections for all targets using the formula (5.2) are presented in table 5.1. In the last column of table 5.1, K^0 inclusive cross sections obtained by integrating numerically both distributions in figure 5.3.

Studying the behaviour of the cross section as a function of the mass number gives a hint whether the K^0 are produced inside the nucleus or on the surface. Therefore, the cross section is plotted as a function of the mass number A (volume) or as a function of $A^{2/3}$ (surface). Figure 5.5 illustrates the behaviour of the K^0 inclusive cross section as a function of A (left panel) and as a function of $A^{2/3}$ (right panel). The error bars for each data point are statistical only (see table 5.1), the plotted lines on top data points are results of the fit.

From the fit (left panel), it is clear that the data points do not follow a straight line behaviour as a function of A. The quality of the fit (χ^2) which is about 25

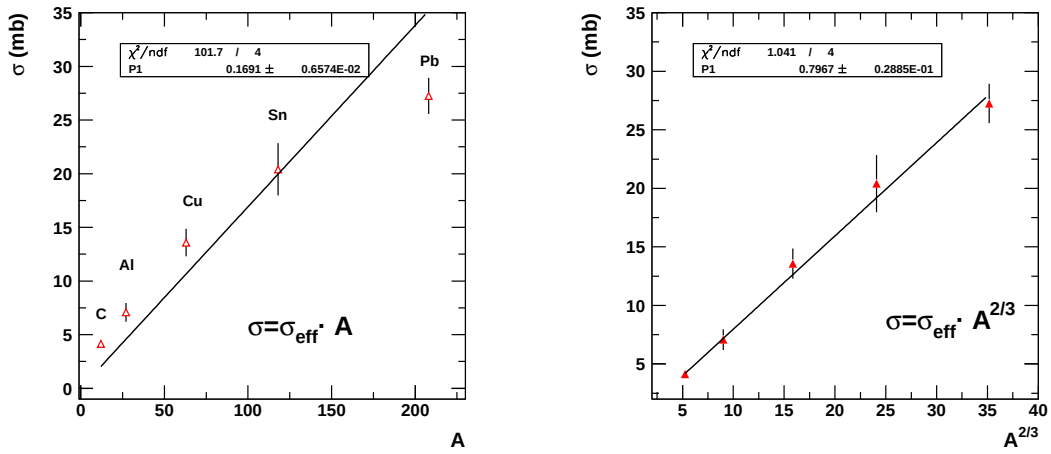

Figure 5.5: The behaviour of the K^0 production cross section as a function of the mass number A of nuclei (left panel) and as function of $A^{2/3}$ (right panel). The lines represent results of fits with a straight line in both panels.

proves that. The opposite can be seen in the right panel, the data points show a straight line behaviour as a function of $A^{2/3}$ (i.e. the surface of the nucleus is proportional to R^2 which is proportional to $A^{2/3}$). The (χ^2) has a value of about 0.25, which indicates that the K^0 inclusive cross section scales with the surface and not with the volume. One concludes that the K^0 are produced mainly on the surface of the nucleus and not in the volume.
To further check these results, the data points are fitted with a combined function including contributions from surface and volume terms, like

$$\sigma = \sigma_{\text{eff1}} \cdot A + \sigma_{\text{eff2}} \cdot A^{2/3} \quad . \tag{5.3}$$

The left panel of figure 5.6, shows the inclusive cross section as a function of the mass number A. The line is a result of the fit with the function given in (5.3). When comparing the contributions of the volume ($\sigma_{\text{eff1}} \sim -0.002$) and surface ($\sigma_{\text{eff2}} \sim 0.8$) parts in absolute numbers, one can see that the volume contribution is more than two orders of magnitude below the surface contribution. Within the statistical errors σ_{eff2} agrees with the value extracted from figure 5.5 which is about 0.8 mb.

Another independent check can be done fitting the data points with a power-law function

$$\sigma = \sigma_{\text{eff2}} \cdot A^{\alpha} \quad , \tag{5.4}$$

The parameter α determines the scaling behaviour of the cross section. If α is

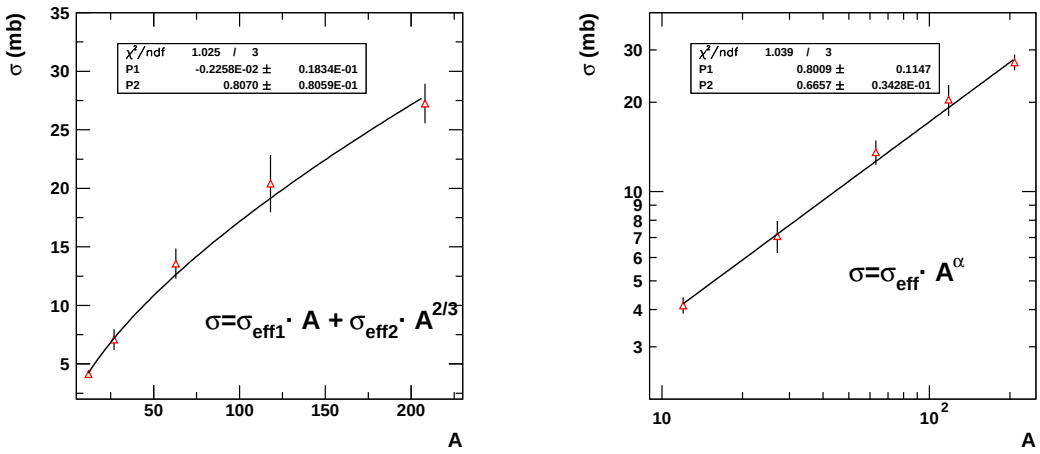

Figure 5.6: Behaviour of the K^0 inclusive cross section as a function of A. The line in the left panel is a result of the fit with a function which includes effects from surface and volume terms. The line in the right panel is a result of the fit with a power law function with an exponent α close to 0.66.

close to one, this means that the cross section scales volume-like, if it is close to $2/3$ then it scales surface-like. The right panel of figure 5.6 illustrates the fit of the data points with the power-law function (5.4) in a logarithmic scale. The fit has an χ^2 of the order of 0.35 and the α has a value of 0.66 which perfectly agrees with the case of the surface-like scaling law, with an effective cross section of 0.8 mb. From those two independent checks, one can conclude that the K^0 are produced on the surface of the nuclei with an effective cross section of 0.80 ± 0.11 mb.

5.5 Inclusive Momentum Spectra of K^0 in Pb and C

To learn about the dynamics of the K^0 production as a function of the system size, the momentum distributions of K^0 produced in π^- Pb and in π^- C reactions are compared. Furthermore the ratio of the momentum distributions between Lead and Carbon is presented.

Using the set of cuts given in table 3.4, the K^0_S invariant mass spectra is reconstructed and background corrected in bins of 50 MeV/c momentum. The same is done for the momentum spectra. Figure 5.7 illustrates in logarithmic scale the K^0 momentum spectra produced in Lead (blue stars) and in Carbon (red circles) in the CDC acceptance (error bars on the data points are statistical only).

The maximum of the momentum distribution in Lead is at about 250 MeV/c, and

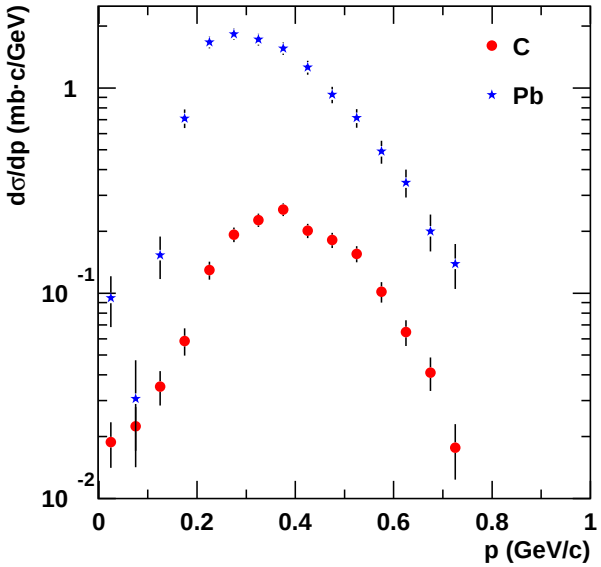

Figure 5.7: Differential momentum spectra of K^0 produced in Lead (blue stars) and in Carbon (red circles) in the CDC acceptance. Data points above 0.8 GeV/c were taken out due to the big statistical fluctuations. The error bars are only statistical.

is shifted towards lower momenta with respect to the one in Carbon which is at about $350\,\mathrm{MeV/c}$. This can be explained by the difference of the radial charge distributions for both targets (in case of the Carbon the distribution is Gaussian-like whereas the Lead nucleus has a Fermi function approximately with a surface thickness of about 2.4 fm [111]). In nuclear matter a pion with $1.15\,\mathrm{GeV/c}$ momentum has a mean free path of 1 fm (i.e. $\lambda = \frac{1}{n\cdot\sigma}$, where $\sigma \sim 60$ mb and $n \sim 0.17\,\mathrm{fm}^{-3}$). When hitting a nucleus, the K^0 are produced mainly on the surface of the nucleus. Due to the small number of nucleons in the Carbon nucleus with respect to the Lead nucleus, K^0 particles do not suffer too much rescattering with the nucleons. Whereas in the case of the Lead target the kaons they rescatter more and loose more energy than the ones in Carbon before escaping the nucleus.
At momenta below the maximum of the distribution, the K^0 produced in $\pi^- + Pb$ reactions show a steeper increase than the ones produced in $\pi^- + C$ reactions. Low momentum K^0 spend more time in the nuclear medium than those with higher momenta. Thus they are more sensitive to the nuclear potential. The steep increase at low momenta can be explained by the acceleration of the K^0 due to the repul-

sive nuclear potential. Therefore, K^0 produced in Lead, feel a stronger nuclear potential and will be pushed out more than the one produced in Carbon.

The ratio $R = \frac{(d\sigma/dp)_{\mathrm{Pb}}}{(d\sigma/dp)_C}$ as a function of the total momentum is shown in figure 5.8. At low momenta the ratio increases as a function of the momentum and reaches a maximum at about $200-250\,\mathrm{MeV/c}$. Above $250\,\mathrm{MeV/c}$ the ratio starts to decrease and above $400\,\mathrm{MeV/c}$ it shows a constant value of about 5.

The steep increase of the ratio from 50 to $250\,\mathrm{MeV/c}$ can be explained by the

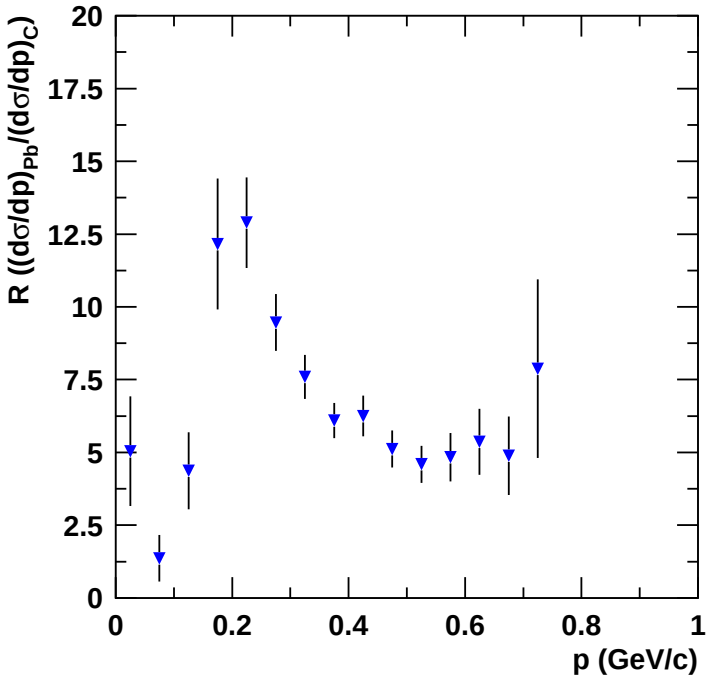

Figure 5.8: The ratio between K^0 momentum distributions in Lead and Carbon targets in the CDC acceptance. The error bars are statistical only.

acceleration of kaons which have low momenta by the repulsive nuclear potential. The decrease of the ratio from 250-400 $\mathrm{MeV/c}$ can be explained by a decrease on the number of K^0 in the Lead target whereas in Carbon the number of produced K^0 looks constant (i.e. like a plateau) at this momentum range. Above $400\,\mathrm{MeV/c}$, for both targets, the number of K^0 decreases as function of momentum with same amount (at this momentum range both spectra have roughly the same slope).

5.6 Systematic Error Evaluation

In this experiment there are three main sources for systematic errors:

1. The wide spot of the pion beam, which translates into an error on the efficiency evaluation.

2. The method used to extract the signal of strange particles (Λ and K^0).

3. The counting of beam particles for a given trigger

As it was mentioned in chapter 3, the pion-beam has a spot of the order of 4×4 cm ^{2} in the (x,y) plane (see figure 3.1). The silicon detectors were used to track the beam and extrapolate it to the target (i.e. to the interaction point). Thus, there are two possibilities to reconstruct the vertex, via the CDC and via the silicon detectors. Figure 5.9 shows a comparison of the reconstructed vertex obtained from the CDC (red curve) and silicons (blue curve) detectors in (x,y) plane. Both distributions (in the CDC and in the silicon) in (x,y) plane, have different spatial resolutions. The vertex resolution in the (x,y) plane has two contributions, one

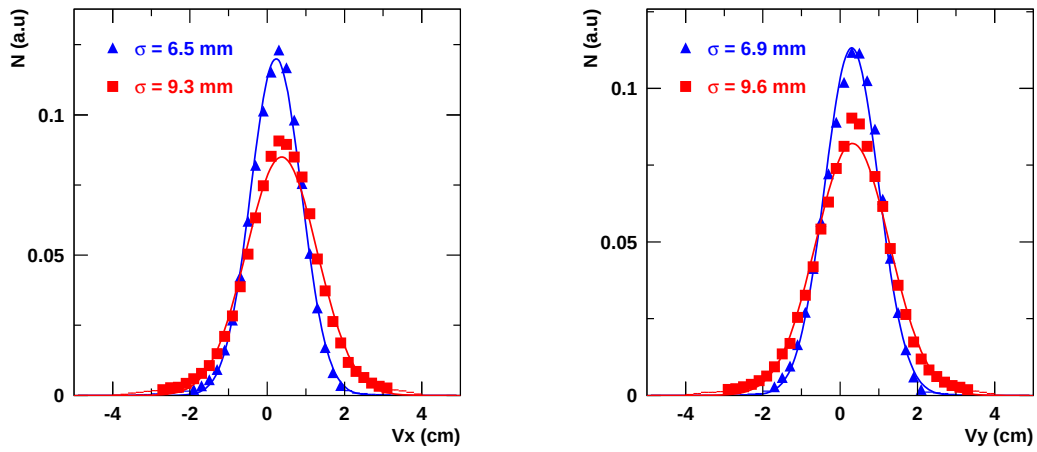

Figure 5.9: Vertex distributions obtained from the CDC and Silicon detectors. The left and right panels show the reconstructed vertex along the x and y axes respectively. Red curve represents the obtained vertex from the CDC and the blue one from the Silicon detector.

due to the size of the beam spot (σ_{beam}) and the other one due to the tracking

(σ_{tracking}) of particles to reconstruct a vertex. These two contributions are independent, therefore the total resolution $\sigma(x,y)$ is given by

$$\sigma(x,y) = \sqrt{\sigma^2_{\text{beam}}(x,y) + \sigma^2_{\text{tracking}}} \tag{5.5}$$

In the case of the silicon detector σ_{tracking} can be neglected since the beam particles have to pass 300 μm of silicon material and the only effect which particles can encounter is multiple scattering. The calculated deviation due to multiple scattering is one order of magnitude less than σ in the (x,y) plane. Therefore, in the case of the silicon detector $\sigma(x,y) = \sigma_{\text{beam}}(x,y)$.

In the case of the CDC, the separation between σ_{beam} and σ_{tracking} can not be done. σ_{tracking} contains all resolutions concerning track quality. Since not all distortions can be included in GEANT (see chapter 4), first the variation of the efficiency with the size of the beam spot (i.e. smearing the vertex) has to be checked. Afterwards, comparing the obtained efficiency when the vertex is smeared as in the silicons and in the CDC.

The vertex in the (x,y) plane (i.e $\sigma_{\text{inp}}(x,y)$) in the level of simulation input [106] is smeared. After tracking, The obtained $\sigma(x,y)$ is compared with the one from data σ_{data}. To obtain the proper efficiency, both, σ_{sim} (after tracking) and σ_{data} have to agree. Therefore, the σ_{inp} is adjusted until σ_{sim} and σ_{data} agree. The obtained efficiency for different values of σ_{sim} is shown in figure 5.10. σ_0 corresponds to the resolution σ_{sim} which agrees with data and ε is the corresponding efficiency.

The efficiency variation is nearly linear as a function of the resolution. This can be explained by the fact that the more the vertex is spread out in the input the more of K^0 with long flight paths with respect to the primary vertex can be found. This can be translated into the d_0 of the daughters. The upper left and right panels of figure 5.11 show d_0 distributions for π^- and π^+ for different widths of the vertex. Green triangles ($\sigma = 3 \cdot \sigma_0$) shows slightly higher yield at high d_0 in comparison to the distribution with $\sigma = 1 \cdot \sigma_0$ and $\sigma = 0 \cdot \sigma_0$. In the lower left panel the transverse flight path of K^0 for different widths of the vertex is plotted. Here is clear that the distribution with a width of $3 \cdot \sigma_0$ has a higher yield than other two distributions. The same remark can be made for the distributions concerning the pointing angle $\Delta\phi$. To quantify the variations of the efficiency due to the vertex smearing, we feed in GEANT the same resolution σ_{inp} as the one in data obtained from silicons. In this case there is no need to adjust σ_{sim} as before because in the case of silicons σ_{tracking} is negligible, therfore $\sigma_{\text{sim}} = \sigma_{\text{beam}}$. The obtained efficiency in this case is 1.1%. There is a 10% difference with respect to the efficiency obtained when using a σ_{sim} comparable to the one from the CDC.
One can conclude that a 10% systematic error is an upper limit for estimating the efficiency.

It was already explained in chapter 3 why we adopt a cut strategy to extract the K^0_S signal. There are two sets of cuts, one set (C1) is in table 3.4 and the other

		DATA				SIMULATION						
		S/B	sign.	N_{K^0}	σ (MeV/c^2)	S/B	sign.	N_{K^0}	σ (MeV/c^2)	ε	P ($\cdot 10^4$)	Error (%)
M1	C1	15.5	36	1350	13.6	64.0	31	1020	14.1	0.010	13.5	6.0
	C2	18.8	32	1076	13.0	69.0	27	760	13.2	0.0075	14.4	
M2	C1	4.1	53	3528	14.4	26.0	52	2877	14.2	0.028	12.6	8.4
	C2	4.1	45	2480	13.1	28.0	42	1852	13.1	0.018	13.7	
M3	C1	2.8	54	3966	14.5	18.0	55	3214	14.4	0.032	12.4	11.0
	C2	3.1	51	3462	13.7	21.0	48	2502	13.7	0.025	13.8	

Table 5.2: Evaluation of the systematic errors. M1, M2 and M3 contains different sets of cut: C1 and C2. Each set (i.e. C1 and C2) is chosen as such to have roughly to the same S/B. The same set is applied for simulation. Afterwards, within one set, the efficiency (ε) and the K^0 production probability (P) is evaluated. The relative difference in (P) between C1 and C2 is quoted as the error.

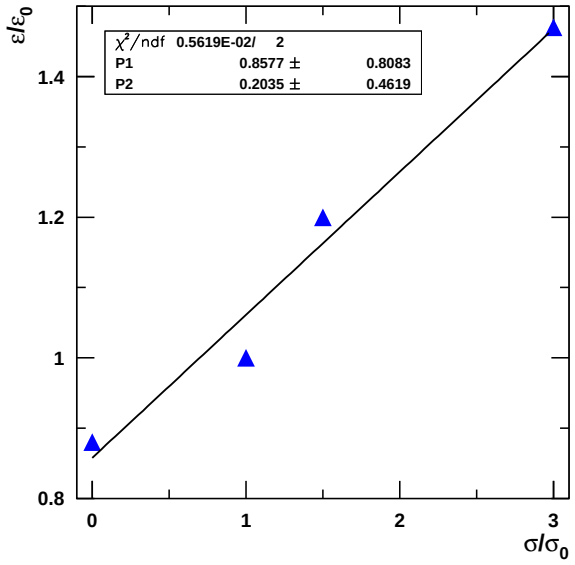

Figure 5.10: The Normalized efficiency as a function of the normalized vertex width. The line is a result of the fit with polynome of order one.

one (C2) is in table 3.5. Both sets give a different number of reconstructed K^0_S, but if one correct this number to 4π using the efficiency, both sets should give the same yield.

To evaluate the differences between those two cuts we vary C1 and C2 cuts in a way that one obtains roughly the same signal over background (this combination of C1 and C2 is called M1). Afterwards, we apply the same combination to the simulation to extract the efficiency. Table 5.2 presents three different combinations of C1 and C2. We compare the obtained significances and widths of the signal in data as well as in simulation. Afterwards, we evaluate the efficiency (ε) and then the yield of K^0 in 4π (P) for each combination of C1 and C2. At the end we evaluate the error between yields obtained from C1 and C2 cuts.
This error is a result of our choice of the method used to evaluate the number of reconstructed K^0. We obtain for M3 a maximum error of 11% which is our systematic error.

Two different scalers have been used to count the number of beam particles which pass the start counter (i.e. for a given trigger). The differences between the numbers of beam particles in both scalers are tiny and are in the order of 0.1%.

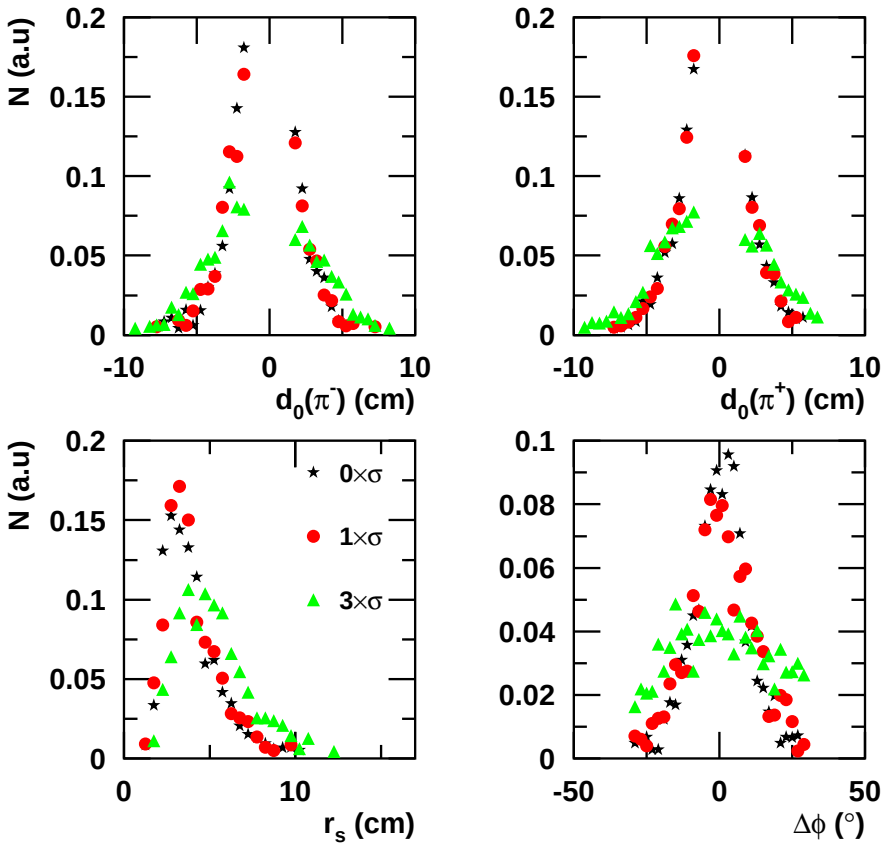

Figure 5.11: The upper plots: A comparison of observables ($d_0(\pi^-,\pi^+)$) characterizing daughters of K^0 for different widths of the vertex. The lower plots: A comparison of the observables characterizing $K0$ (flight path and pointing angle) for different widths of the vertex.

This study allows us to derive a systematic error for the efficiency evaluation which is 10%. A systematic error of 11% due to the set of cuts used to reconstruct K^0 is given. The error which occur due to the miscounting of the beam particles can be neglected in comparison to the previous systematic errors. Under those conditions the measured K^0 inclusive cross section in π^- A reactions is: $0.8 \pm 0.11(\text{Stat}) \pm 0.17(\text{Syst})$ mb.

Chapter 6

Model Comparisons

In the previous chapter, invariant and absolute cross sections of inclusive K^0 production in $\pi^- + A$ reactions were explained in terms of the system size dependence. In order to search for medium effects on the K^0 production in $\pi^- + A$ reactions, theoretical models are needed which can describe reaction dynamics event by event including all possible reaction mechanisms. Two of the models which are suited for SIS energies are IQMD [109, 110]and HSD [52, 46]. It was shown in chapter 4 that IQMD reproduces quite well the experimental K^0-phase-space distributions, however it does not take into account the difference between charged kaons and neutral kaons. Therefore, IQMD calculations were not used in the comparison to measured data. HSD is a more advanced model which takes into account the isospin difference between K^+ and K^0. HSD calculations are available for the two systems: $\pi^- + C$ and $\pi^- + Pb$. Two different versions of the HSD model were used. In both versions a minimum bias distribution for the pion is used with an impact parameter $b \leq 3.5$ fm for the $\pi^- + C$ reactions and $b \leq 6.5$ fm for $\pi^- + Pb$ reactions. A total number of 30 000 and 60 000 events were used in the case of the Carbon and Lead targets, respectively. The geometrical filter was not applied to those events. One version takes into account the *KN* potential in the final state interaction (labeled *with pot.*) with a depth of 20 MeV, while the other one does not take into account that potential (labeled *without pot.*). In both versions, the K^0 rescattering inside the nuclear matter is included.

In this chapter, the K^0 production cross section as well as its phase-space (rapidity and momentum) distributions are compared to the transport model HSD. The ratio of the measured K^0 momentum distribution between Lead and Carbon is compared to the HSD model and also to the K^+ measurements by ANKE [62]. At the end, the measured absolute K^0 inclusive cross section is compared to HSD predictions and to microscopic calculations of Tsushima et al. [67].

6.1 Invariant Cross Section

The comparison of the inclusive K^0 invariant cross section between model predictions and experimental results is shown in figure 6.1 for the case of the Carbon target (i.e. $\pi^- + C$). The comparison is done in four bins of rapidity from the backward hemisphere $y \leq -0.2$ to the forward hemisphere $y \geq 0.2$.
In general, the model calculations with and without potential seem to predict the same K^0 yield for almost all transverse momenta p_t and rapidities y. The only differences can be seen for two rapidity bins $y \leq 0.2$ and $y \geq 0.6$ at transverse momenta below $150\,\mathrm{MeV/C}$.

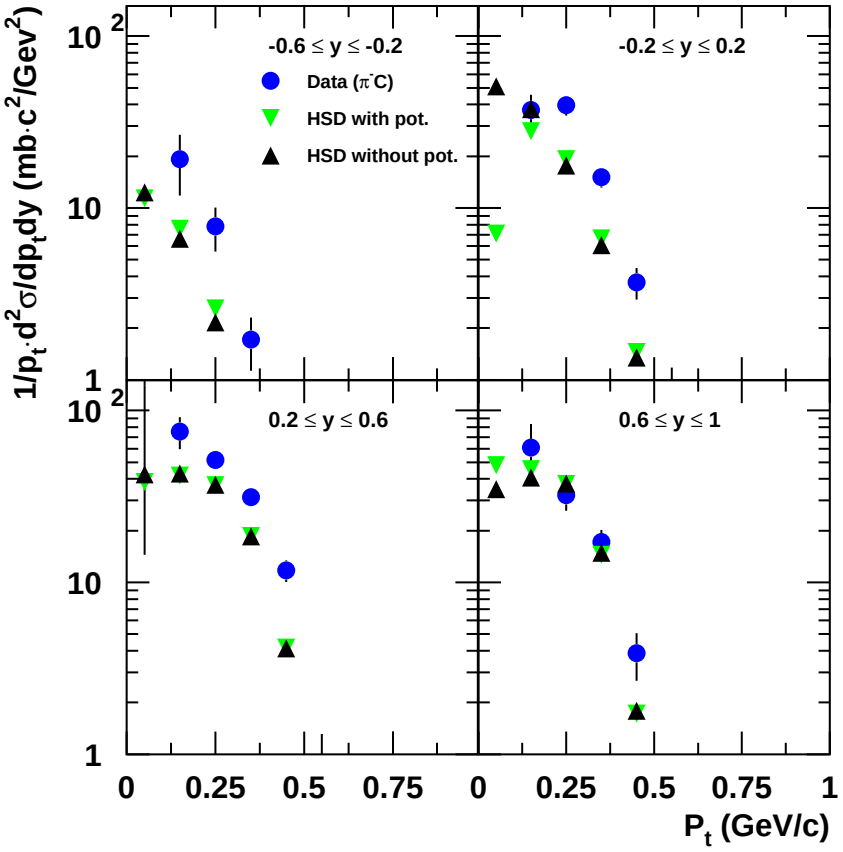

Figure 6.1: K^0 invariant cross section as function of p_t for four rapidity bins. Blue circles represent the measured K^0 invariant cross section in $\pi^- + C$ reactions. HSD calculations of the K^0 invariant cross section including the KN potential and without KN potential are represented by the green and black triangles, respectively.

Comparing model calculations to measured data, it becomes obvious that the trend of the measured K^0 yields can be reproduced by the model (with and without potential) over the whole rapidity range. The major difference between data and model lies in the K^0 yield. The measured yield lies above the HSD results by nearly a factor 4 for rapidities $y \leq 0.6$, above that a good agreement can be seen between HSD calculations and data.

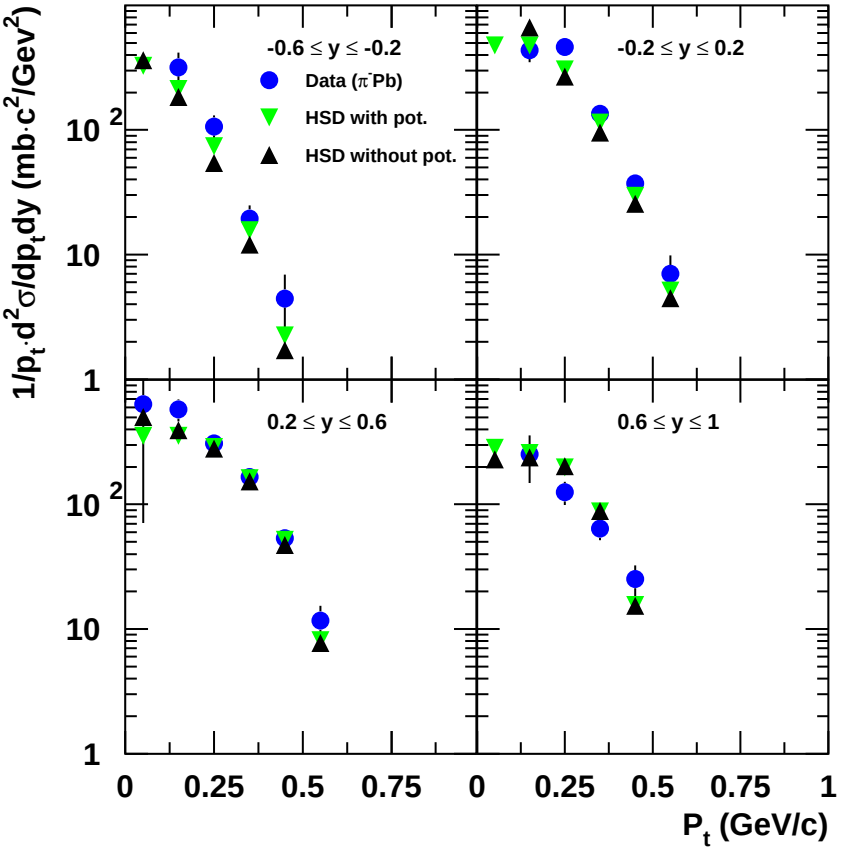

Figure 6.2: K^0 invariant cross section as function of p_t for four rapidity bins. Blue circles represent the measured K^0 invariant cross section in $\pi^- + Pb$ reactions. HSD calculations of the K^0 invariant cross section including the KN potential and without KN potential are represented by the green and black triangles, respectively.

Figure 6.2 shows the same comparison for $\pi^- + Pb$ reactions. The model calculations do not show a visible difference, between both assumptions (with and without potential). Generally, the trend of the measured yield is reproduced for all rapidity bins and the overall agreement of the yields is better than for $\pi^- +$

C. From the backward hemisphere up to rapidities $y \leq 0.6$, HSD calculations including the *KN* potential, show a better agreement with the data. At forward rapidities $y \geq 0.6$ the data points lie slightly below the model calculations in the case of Lead while in the case of Carbon the data points show a good agreement with calculations. This may be explained by the shadowing effect.

6.2 K^0 Rescattering in HSD

Before starting the comparison of the rapidity and momentum distributions between data and HSD calculations, it is important for the interpretation to see how the K^0 rescattering inside nuclear matter varies as a function of the system size. Figure 6.3 shows $\sigma^{-1} \cdot d\sigma/dy$ (left panel) and $N^{-1} \cdot dN/dp$ (right panel) distributions of K^0 produced in the Lead and Carbon targets obtained from HSD without in-medium *KN* potential.
The normalized rapidity distribution (left panel) for Lead has a maximum at $y \sim 0$, while the one for Carbon is peaked at $y \sim 0.4$. The two distributions overlap at a rapidity of 0.25. Below target rapidity $y \leq 0$, the K^0 yield is bigger in $\pi^- + Pb$ than in $\pi^- + C$, the opposite can be seen at $y \geq 0.25$.

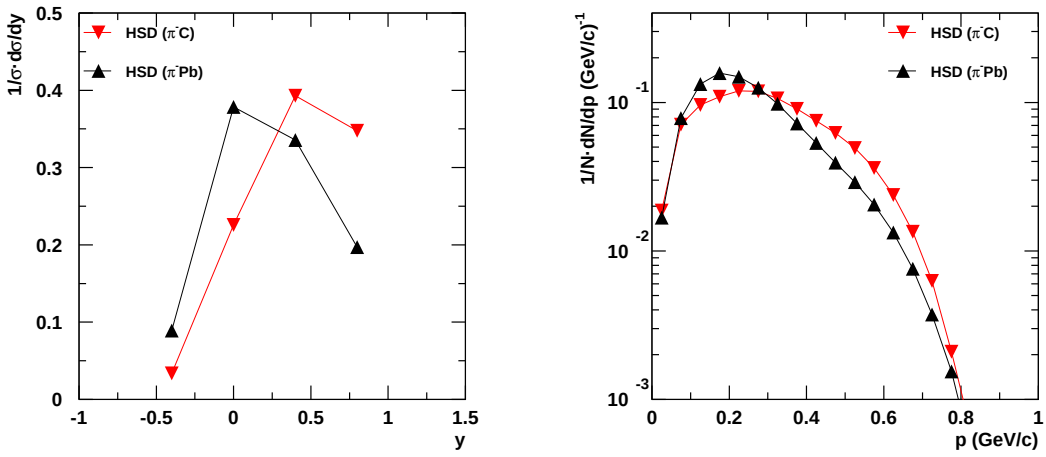

Figure 6.3: Left panel: HSD calculations (without potential) of the rapidity distribution of the K^0 produced in Lead (black triangles) and Carbon (red triangles). Right panel: HSD calculations (without potential) of the momentum distribution of the K^0 produced in Lead (black triangles) and Carbon (red triangles).

The momentum distribution (right panel) of K^0 produced in the Lead target has a maximum at $200\,\mathrm{MeV/c}$ whereas the distribution has its maximum at

250 MeV/c for the Carbon target. Below 300 MeV/c, the yield of K^0 produced in Lead is bigger than in Carbon, at momenta above 350 MeV/c the opposite behaviour can be seen.
The shift of the maximum of both, momentum and rapidity distributions, in Lead with respect to Carbon is due to rescattering of the K^0 inside the nuclear medium. It is clear that the rescattering of K^0 is more pronounced in the Lead than in the Carbon due to the bigger size of the Lead nucleus.

6.3 Rapidity Distributions

Experimental results and model calculations of the $d\sigma/dy$ distributions of K^0 produced in $\pi^- + C$ reactions are shown in the left panel of figure 6.4. Model calculations do not show a sensitivity to the *KN* potential. Data points, lie above model calculations at the target rapidity and at forward rapidity below 0.5. Within the error bars, the data agree with the model at forward and target rapidities. The

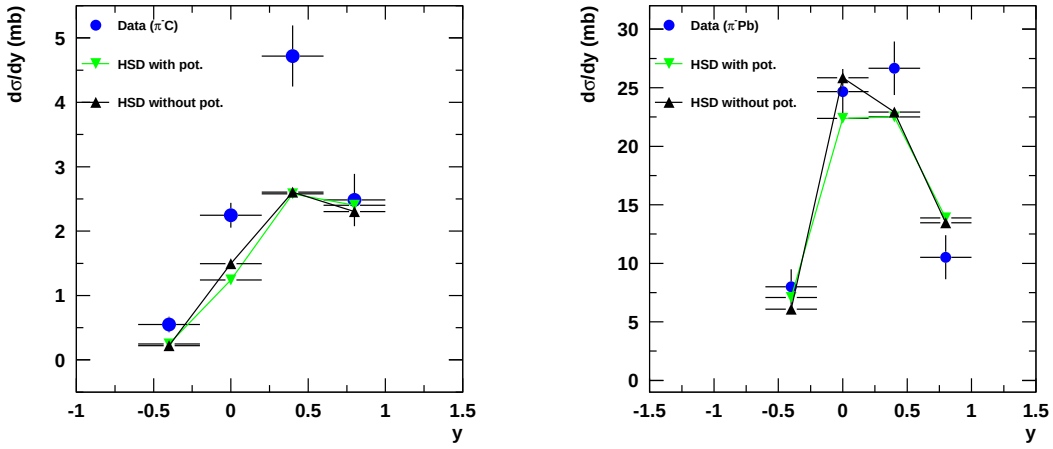

Figure 6.4: Left panel: A comparison of the K^0 rapidity distributions produced in $\pi^- + C$ between data (blue circles) and model calculations including the *KN* potential (green triangles) and without potential (black triangles). Right panel: A comparison of the K^0 rapidity distributions produced in $\pi^- + Pb$ between data (blue circles) and model calculations with potential (green triangles) and without potential (black triangles).

mean value of the $d\sigma/dy$ distribution is about 0.37 for the model prediction with potential, 0.35 for model without potential and 0.31 for the measured data. Distributions obtained from the model are peaked more forward than those from the data. First, the effect of the *KN* potential on the mean value of the $d\sigma/dy$ is about

5%. The shift of the model-calculated mean values of $d\sigma/dy$ with respect to the measured one, can be explained by the rescattering effect of the K^0 inside the nuclear medium.

The measured $d\sigma/dy$ distribution of K^0 produced in the Lead target as well as model predictions are plotted in the right panel of figure 6.4. As before, the model predictions with and without potential show a visible difference only at target rapidity, which is about 3.5 mb per rapidity unit. At rapidities below 0.4, the model calculations show an agreement with the measured data and at target rapidity the model calculation without potential is closer to the data point. The $d\sigma/dy$ distribution obtained from the model with and without potential have the same mean value of 0.22, while the measured distribution has a mean value of 0.20. The effect of the *KN* potential on the mean of the $d\sigma/dy$ distribution is absent if compared to the case of the Carbon target.

6.4 Momentum Spectra

The measured momentum distribution and the ones obtained from model calculations for K^0 produced in Carbon are shown in the left panel of figure 6.5. Model predictions as well as the data are normalized to the number of entries in each histogram. At momenta above 400 MeV/c, model calculations with and without potential do not show significant differences. Below 400 MeV/c a difference can be seen between the two versions of the model. Model calculations with potential lie above the ones without potential down to the maximum of the spectra which is at about 250 MeV/c. Below 200 MeV/c the model calculations with potential are slightly below the points corresponding to the calculations without potential.

The measured momentum spectrum shows a different behaviour than both model predictions. The maximum of the distribution is at about 350 MeV/c. Below 300 MeV/c, the measured distribution has a steeper slope in comparison to model calculations. The shifted maximum of the distributions obtained in the model with respect to the measured one indicates that the model predictions (with and without potential) contain more rescattering of the K^0 in nuclear matter.

The right panel of figure 6.5 depicts the measured momentum distributions of K^0 produced in Lead target in comparison to HSD calculations. Model calculations with and without potential show the same trend for all momenta. As for the Carbon target, above 400 MeV/c no difference can be seen between calculations with and without medium effects. The difference between both model calculations can be seen at momenta below 450 MeV/c, the maximum of the momentum distribution without potential is shifted by 50 MeV/c with respect to the one with potential.
The measured spectrum shows a different trend as compared to the model. As

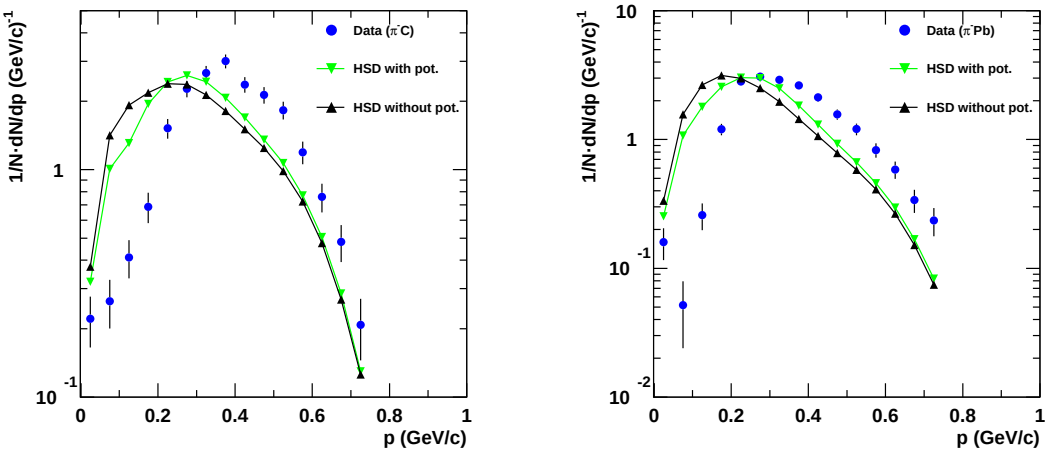

Figure 6.5: Left panel: Measured K^0 momentum distributions (blue circles) in the CDC acceptance from the Carbon target in comparison to HSD calculations with potential (green triangles) and without potential (black triangles). Right panel: Measured K^0 momentum distributions (blue circles) in the CDC acceptance from the Lead target in comparison to HSD calculations with potential (green triangles) and without potential (black triangles).

for the case of the Carbon, the slope of the measured spectrum is steeper than the ones from the model calculations below momenta of 250 MeV/c. The data points show a lower K^0 yield in comparison to the model at momenta below 250 MeV/c and above this value the opposite is found. The visible difference between data and model calculations in figure 6.5 is due to much more pronounced effects of the potential and rescattering in the data than in the model calculations.

6.5 Ratio of the Momentum Distributions

The target mass dependence of the meson cross section in elementary reactions (pion- or proton-induced reactions) contains informations on the production process and the propagation of mesons in nuclear matter. Using proton-induced reactions, the ANKE collaboration measured the mass dependence of forward K^+ production on different targets between 1.5 and 2.3 GeV [62]. The mass dependence of the K^+ production was studied on the basis of the ratio $R = (\mathrm{d}\sigma/\mathrm{d}p)_{\mathrm{Au}}/(\mathrm{d}\sigma/\mathrm{d}p)_{\mathrm{C}}$. A strong suppression of the ratio was observed for K^+ momenta below 250. MeV/c. This observation was interpreted in terms of a repulsion by the Coulomb and nuclear potentials in the K^+A system [62].

Since the K^+ and K^0 are isospin partners, their production dynamics (mechanisms) in the nuclear medium are the same. Figure 6.6 shows a comparison between ratios of K^+ produced in Gold to those from Carbon (full triangles) and the ratio of K^0 produced in Lead to those from Carbon. The differences between the two measurements are:

- in comparison to the K^+, the K^0 does not feel a Coulomb potential
- the K^+ spectra from ANKE [62] were measured at $\theta \leq 12^\circ$ (in the laboratory system) while the K^0 spectra here are measured for polar angles ranging from 27° to 116° (i.e. in the CDC acceptance)

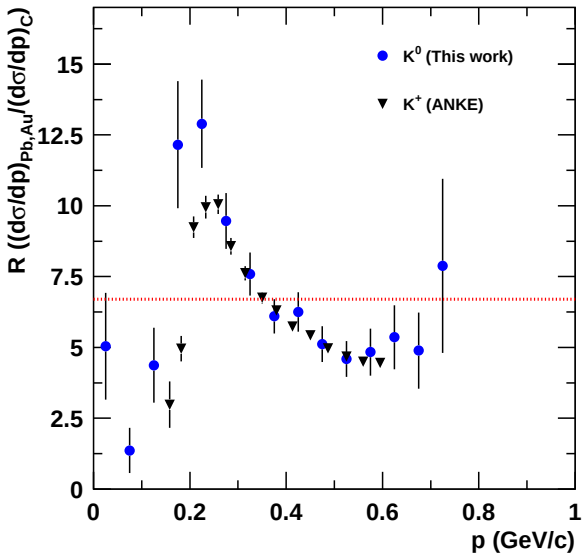

Figure 6.6: Comparison of the measured ratio $(\mathrm{d}\sigma/\mathrm{d}p)_{\mathrm{Au}}/(\mathrm{d}\sigma/\mathrm{d}p)_{\mathrm{C}}$ for the K^+ (black triangles, points are adapted from [112]) and the measured ratio $(\mathrm{d}\sigma/\mathrm{d}p)_{\mathrm{Pb}}/(\mathrm{d}\sigma/\mathrm{d}p)_{\mathrm{C}}$ for the K^0 (blue circles). The dashed line represents the geometrical ratio. Error bars on the blue circles are statistical only.

The shapes of both ratios (for K^+ and K^0) agree quite well for all momenta. At momenta above $300\,\mathrm{MeV/c}$ both ratios agree perfectly with each other which is an indication that effects which govern the shape of both ratios most likely has the same origin.
Below $300\,\mathrm{MeV/c}$, a lower ratio for the K^+ was measured with respect to the K^0.

The ratio distributions are peaked at slightly different momenta. For the K^0, the maximum is at momenta between 200-250 MeV/c and for the K^+ it occurs at momenta of about 260 MeV/c.
The shape of the K^+ ratio was explained on the basis of CBUU transport calculations [63, 62] (see figure 1.8). In a purely classical picture, K^+ produced at some radius "R" in a nucleus acquire an additional momentum of $p_{\min} = \sqrt{2m_k V_c(r)}$ due to the repulsive V_c Coulomb potential. For a Gold nucleus, this corresponds to a minimum momentum of 130 MeV/c. Thus, the ratio should drop to zero for smaller kaon momenta. A repulsive K^+ nuclear potential with a strength in the order of 20 MeV shifts the kaon momentum and thus the peak position [112, 62].

At high momenta (above 300 MeV/c) the decrease of the ratio for K^+ and K^0 below the geometrical value R_{geo} (i.e. the dashed line which corresponds to $R_{\text{geo}} = (\pi R^{2/3})_{\text{Pb}}/(\pi R^{2/3})_{\text{C}} \sim 6.7$) can be explained by the shadowing effect which is directly related to the nucleus size. Since the Lead (Gold) target has a radius of the order of 7 fm and the Carbon radius of the order of 3 fm, the number of kaons produced in Lead (Gold) is being reduced much more in comparison to the one in Carbon.
Low-momentum kaons spend more time inside the nuclear medium than those with high momenta. Therefore, those kaons are more sensitive to the nuclear potential. It can be seen that the measured ratio for K^0 does not drop to zero at 130 MeV/c but rather at momenta close to zero MeV/c, within the error bars. The difference between K^+ and K^0 production at low momentum inside the nuclear medium can be assigned to the Coulomb interaction.

To further understand the behaviour of the ratio as a function of the momentum, HSD predictions (with and without potential) are compared to the measured ratio in figure 6.7. Above 250 MeV/c the model calculations with and without potential do not show any significant difference and the model predicts a higher ratio than the measured one as well as the geometrical one. Below 250 MeV/c, the ratio including the *KN* potential goes to infinity at zero MeV/c, whereas the one that does not include the *KN* potential goes to a constant value close to 22 at 0 MeV/c. Contrary to the model predictions, the measured ratio shows a suppression below 200 MeV/c and goes down to zero at momenta close to zero MeV/c. The possible explanation for this failure, is that the dynamics which are responsible for the K^0 production in nuclear matter must be wrong in the model, this issue is not yet resolved. At this stage, where the model fails in reproducing the measurement, the only explanation for the behaviour of the measured ratio below 200 MeV/c is due to the *KN* potential which accelerates kaons with low momenta when leaving the nucleus.

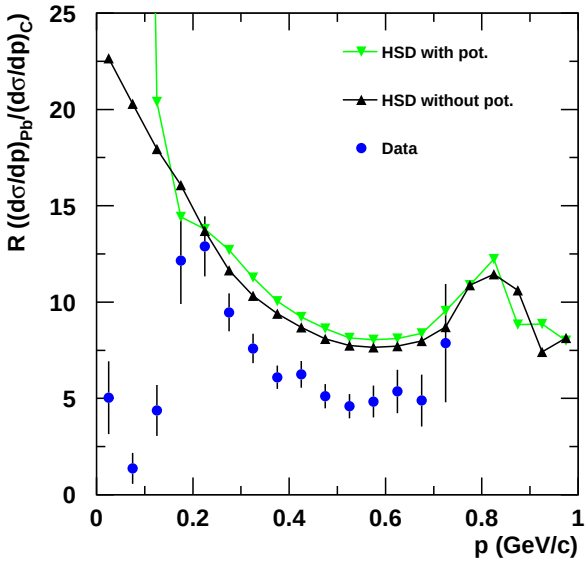

Figure 6.7: A comparison between HSD calculations with potential (green triangles), without potential (black triangle) and measurements (blue circles) for the ratio $(d\sigma/dp)_{Pb}/(d\sigma/dp)_C$.

6.6 K^0 Inclusive Cross Section

To understand the behaviour of kaon production cross section in the nuclear medium at $\rho = \rho_0$ in π-induced reactions, comparisons to transport and microscopic models are needed. Unfortunately, the existing data from the HSD transport model are for Carbon and Lead targets only. Calculations concerning other targets (Al, Cu and Sn) are being worked on, therfore at this moment it is not possible to have a complete systematics of K^0 inclusive cross sections. Nevertheless, the K^0 inclusive cross section in Lead and Carbon as calculated by HSD are compared to the measured K^0 inclusive cross sections in the left panel of figure 6.8. The model calculations with and without potential do not show any sensitivity to the *KN* potential.

As mentioned in chapter 5, the K^0 inclusive cross section has an $A^{2/3}$ dependence on the target mass. The line on top of the data points is the result of a fit. In the case of the Lead target, the model calculations agree quite well with the measured data. It can be seen that the calculated cross sections do not show the same behaviour as the data because in the case of the Carbon target the calcula-

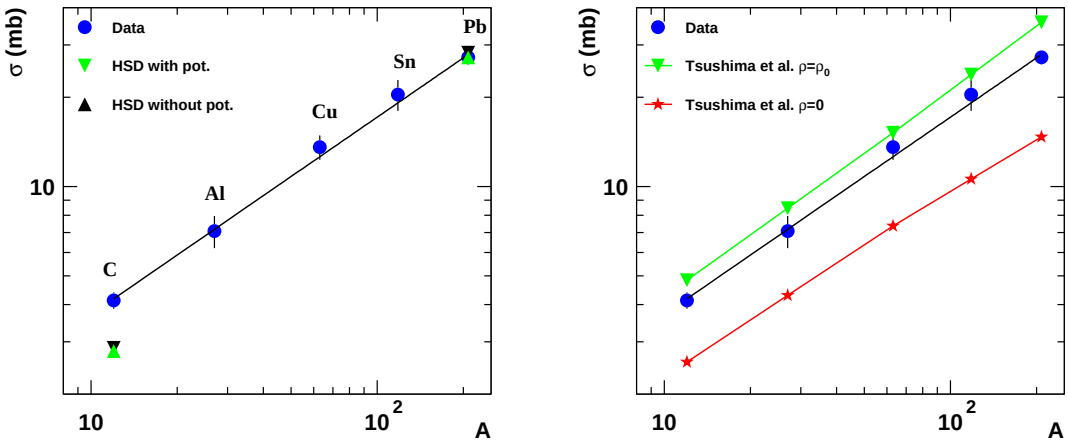

Figure 6.8: Left panel: The K^0 inclusive cross section in π^- +A reactions as a function of the target mass number. Measured K^0 inclusive cross sections are shown in blue circles. The green and black triangles represent HSD calculations with and without potential, respectively. The solid line is the result of a fit (see chapter 5). Right panel: Comparison of the measured K^0 inclusive cross section with microscopic calculations under the assumption that the cross section has an $A^{2/3}$ behaviour.

tions are off by a factor 1.5 from the measurement.

Target	$\sigma(\rho = \rho_0)$ (mb)	$\sigma(\rho = 0)$ (mb)
C	4.83	2.56
Al	8.45	4.30
Cu	15.20	7.35
Sn	23.80	10.60
Pb	35.75	14.70

Table 6.1: The obtained K^0 inclusive cross sections from microscopic calculations at $\rho = \rho_0$ and $\rho = 0$ assuming that the cross section has an $A^{2/3}$ behaviour.

The only available microscopic calculations of kaon production in nuclear matter are from Tsushima et al. [67]. Those calculations were performed for infinite nuclear matter. To be able to compare them with measured data, two assumptions are made:

- an effective cross section is derived from all channels participating in the K^0 production (i.e. $\pi^- p \to K^0\Lambda$, $\pi^- p \to K^0\Sigma^0$ and $\pi^- n \to K^0\Sigma^-$) as follows

$$\sigma_{\text{eff}} = \frac{Z}{A} \cdot \left(\sigma(\pi^- p \to K^0\Lambda) + \sigma(\pi^- p \to K^0\Sigma^0)\right) + \frac{N}{A} \cdot \sigma(\pi^- n \to K^0\Sigma^-) \tag{6.1}$$

- the calculated cross section is parameterized according to the behaviour of the measured cross section:

$$\sigma(\pi^- A \to K^0 X) = \sigma_{\text{eff}} \cdot A^{2/3} \tag{6.2}$$

The inclusive cross section for all targets, obtained at $\rho = \rho_0$ and $\rho = 0$, are presented in table 6.1. The obtained K^0 inclusive cross sections are compared to the measured ones in the right panel of figure 6.8. The model calculations at $\rho = 0$ are nearly a factor 2 below the data for all targets. At $\rho = \rho_0$, the difference is somewhat smaller. The relative differences between model and data range between 10% for Copper and 24% for Lead. These differences can by assigned to the fact that

- microscopic calculations have slightly a higher elementary cross sections at $\rho = \rho_0$.
- microscopic calculations are done in uniform nuclear matter where the shape of the nucleus is neglected completely, whereas with a π^- beam of $1.15\,\text{GeV/c}$ the surface of the nucleus is mostly probed and therefore the kaons are most likely produced at densities $\rho \leq \rho_0$.

Chapter 7

Summary and Outlook

Properties of kaons produced in dense nuclear matter have been studied by a variety of theoretical approaches. Effective kaon masses might change inside nuclear matter due to the partial restoration of the chiral symmetry of QCD. Recently, based on microscopic calculations, it has been demonstrated that the kaon production cross section in pion-nucleon interaction changes its value and behaviour in nuclear matter due to changes of the kaon properties.

In 2004, for the first time the GSI facility was able to provided a pion beam to Cave B with an intensity of 5000 pions per second with a momentum of 1.15 GeV/c. The FOPI collaboration performed a beam time in August 2004 and recorded data for five different targets (Carbon, Aluminum, Copper, Tin and Lead) during a time of 14 days. The main goal of this work was to study the inclusive K^0 production at normal nuclear matter density using a pion beam.

Several extensions and adaptations to the FOPI software were necessary and carried out in the framework of this thesis. In the first part of this work the behaviour of the CDC digitizer in GEANT was investigated and a smearing of the primary vertex to simulate the experimental environment properly was implemented. Energy and spatial resolutions of a track in the CDC were studied within the digitizer. The position resolution of tracks in the transverse plane was aligned to that of the data. A compromise was made between the energy resolution and position resolution along the beam axis to be able to reproduce experimental widths of reconstructed resonances.
A new method for reconstructing Λ^0 from a proton detected in the combined system of Plastic Wall and Helitron and from a pion detected in the CDC was developed. This method gives the possibility of studying the kinematical and dynamical properties of this particle reconstructed in this forward part of the phase space.

The reconstruction of the K^0 from reactions of pions with five targets, for the first time allowed to obtain the mass dependence of the K^0 inclusive cross section

in pion-induced reactions at SIS energies. It was shown that the cross section in pion-induced reactions has an $A^{2/3}$ dependence, which indicates that kaons are mainly produced in the surface of the nucleus.

K^0 differential spectra, i.e. transverse momentum, rapidity and momentum distributions were investigated in terms of the nucleus size. A detailed comparison of K^0 spectra between the Lead and Carbon targets gave the following results:

- The invariant cross sections of K^0 have the same trend over all phase-space in both targets, but they differ in terms of yield.
- The rapidity distribution shows that more more kaons are produced in the forward hemisphere in the case of $\pi^- + C$ than in $\pi^- + Pb$ reactions. At target rapidity and in the backward hemisphere, the opposite is found.
- The momentum distributions of K^0 show a similar trend at high momenta for both targets. At low momenta, both distributions exhibit different slopes: For Lead one observes it shows a steeper increase than for Carbon.

The ratio of the K^0 momentum distribution from Lead to that in Carbon shows a steep decrease down to zero at very low momenta and a decrease below the geometrical ratio at high momenta. Kaons with low momenta spend more time in the nuclear medium, therefore the nuclear potential tends to accelerate them, while kaons with high momenta most likely do not feel the nuclear potential. A detailed comparison of experimental measurements with HSD model predictions has been done. Two versions of HSD model calculations were used: One includes the KN potential in the final state interaction and the other one does not include it. Both versions include the rescattering of kaons in the nuclear medium.
In general, the model reasonably reproduces the trend of the K^0 invariant cross section for both systems (Lead and Carbon) over all phase-space. Some discrepancies have been observed where the model under predicts the yield of K^0 produced in $\pi^- + C$ reactions by about a factor 1.5 with respect to the data in the backward hemisphere and at target rapidity.
HSD model calculations of the K^0 inclusive cross section agree well with the measured value from $\pi^- + Pb$ reactions. For the Carbon target, a difference by a factor of 1.5 is found between model and data. The calculated ratio of the K^0 momentum distribution produced in Lead to that from Carbon at high momenta shows the same trend as in the data, while for low momenta, differences appear between data and model. Here, the calculated ratio increases, whereas in the data the ratio decreases.
Another comparison of the data with microscopic calculations was done. To be able to compare calculations in infinite nuclear matter, K^0 inclusive cross sections

were assumed to have an $A^{2/3}$ dependence as it was found in the data. Good agreement is observed between the microscopic calculations at normal nuclear matter density and the data with a relative difference of 20% at maximum.

A comparison to the data obtained with the ANKE spectrometer at COSY-Jülich in proton-induced reactions was done and an interesting dependence was found in the ratio of the K^+ production in Gold to that in Carbon. The comparison shows a very good agreement for the shape of both (K^0 and K^+) ratio distributions. At high momenta, both measurements predict the same ratio while at low momenta a difference is observed. The K^+ ratio shows a suppression at about 130 MeV/c, whereas the K^0 shows a suppression only at momenta close to zero MeV/c. Based on CBUU transport model calculations, this observation was assigned to the Coulomb potential which accelerates the K^+ in addition to the nuclear potential, while for the case of K^0, only the nuclear potential is felt by kaons which have low momenta.

The exclusive measurement of the production cross section of a K^0 in combination with a Λ^0 or a Σ^0 particle in the final state can be done with the FOPI detector in pion-induced reactions. In addition, this measurement gives the possibility to study the production mechanism of strange particles at $\rho = \rho_0$. In the present sample of data, the statistic was not large enough to measure the number of correlated (K^0, Λ^0) or (K^0, Σ^0) pairs. As a rough estimate, ten times more statistics is needed to be able to measure the correlated (K^0, Λ^0) and (K^0, Σ^0) pairs and also to be able to separate between Σ^0 and Λ^0 pairs. The FOPI collaboration is planning for another pion-beam run in the near future to collect more statistics which will certainly allow for measuring the K^0 exclusive cross section as well as studying its mass dependence at normal nuclear matter density.

The newly installed RPC Barrel which has a good time resolution and a larger acceptance for charged kaons will allow to study the exclusive K^+ cross section in the channel $\pi^- + p \rightarrow K^+ + \Sigma^-$.

Furthermore a proton-induced reaction experiment is also planed to be done with the FOPI detector. K^+ and K^- reaction cross sections will be measured as well as their phase-space distributions. Measurements of the mass dependence of the K^- inclusive cross section will give more insight into the nature of the K^-N interaction.

Appendix A

The Bethe-Bloch Formula

Charged particles passing through matter lose kinetic energy by excitation of bound electrons and ionization. The average energy loss dE per length dx for heavy particles ($m_0 \gg m_e$) is given by Bethe-Bloch formula [113, 114, 115, 116]

$$-\frac{\mathrm{d}E}{\mathrm{d}x} = 4\pi N_A r_e^2 m_e c^2 \rho \frac{Z}{A}\frac{z^2}{\beta^2}\left[\frac{1}{2}\ln\left(\frac{2m_e c^2\gamma^2\beta^2 W_{max}}{I^2}\right) - \beta^2 - \frac{\delta}{2}\right]. \qquad \text{(A.1)}$$

z	–	Charge of the incident particle in units of the elementary charge,
N_A	–	Avogadro number = $6.022 \cdot 10^{23}\,\mathrm{mol}^{-1}$,
Z, A	–	Atomic number and Atomic mass of the medium,
m_e	–	Electron mass,
r_e	–	Classical electron radius $\approx 2.818\,\mathrm{fm}$,
I	–	Ionization constant, characteristic of the absorber material which can be approximated by $I = 16 \cdot Z^{0.9}\mathrm{eV}$,
δ	–	Correction factor due to the density of the medium,
W_{max}	–	Maximum transferable kinetic energy to a free electron in a single collision.

The energy loss $-\mathrm{d}E/\mathrm{d}x$ is usually given in units of $\mathrm{MeV}/(\mathrm{g}/\mathrm{cm}^2)$. The energy loss does not depend on the mass of the ionizing particles, but on their velocity β. As a function of β, dE/dx at low velocities decreases as $1/\beta^2$, then reaches a minimum around $\beta\gamma \approx 4$ and increases for relativistic velocities with $\beta\gamma \to \infty$.

Measurement of the energy loss and velocity of charged particle in the CDC (Helitron) and Barrel (Plastic Wall), respectively, allows for paricle charge ideneti-

fication using

$$-\frac{\mathrm{d}E}{\mathrm{d}x} \propto \frac{z^2}{\beta^2} \quad . \tag{A.2}$$

In the case of the CDC, where the momentum of the particle is measured, its mass can be determined if one assumes its charge to be 1, 2 or higher using the formula

$$-\frac{\mathrm{d}E}{\mathrm{d}x} \propto z^2 + \frac{(m \cdot c)^2}{\left(\frac{p}{z}\right)^2} \quad . \tag{A.3}$$

Appendix B

Kinematical Variables and Invariant Cross Section

In relativistic heavy-ion collisions, it is more convenient to use kinematical variables (describing the phase space of a system) which can be transformed from one frame to another in simple way.

If a beam particle is moving along the z direction towards a fixed target, then one of the kinematical variables which can be used for the produced paricles is the transverse momentum p_t. The other variable is the longitudinal momentum which can be described by an equivalent variable called rapidity. It is a generalization of the velocity given by

$$y \equiv \text{ arctanh}(v_{\shortparallel}) \;=\; \text{arctanh}\left(\frac{p_{\shortparallel}}{E}\right) = \frac{1}{2}\ln\left(\frac{E+p_{\shortparallel}}{E-p_{\shortparallel}}\right), \tag{B.1}$$

where $p_{\shortparallel}$ is parallel to the direction of the beam $p_{\shortparallel} \equiv p_z$. For small velocities the rapidity y becomes: $y = v_{\shortparallel}$.
If one assumes a particle with rapidity y_1 in a frame K_1 and y_2 is the rapidity of the frame K_1 in the frame K_2, then the rapidity of the particle in the frame K_2 is $y = y_1 + y_2$.

The two variables (y, p_t) describing the phase space of a given particle with a mass m are related as follows

$$p_t = \frac{m \cdot \sin\theta}{\sqrt{\left(\frac{\exp(2y)+1}{\exp(2y)-1}\right)^2 \cdot \cos^2\theta - 1}}, \tag{B.2}$$

where θ is the polar angle in the laboratory frame. This formula shows the connection between the phase-space and the geometrical space.

B.1 Particle Decay

The transition rate for a given process is determined by the amplitude $\mathcal{M}$ (which is a Lorentz-invariant matrix) and the phase space factor according to Fermi's "Golden Rule" [117] and it is given by

$$\text{Transition rate} = \frac{2\pi}{\hbar}|\mathcal{M}|^2 \times (\text{phase-space factor}) \tag{B.3}$$

If one assumes that particle "1" decays into several other particles "2,3,4...n", its decay rate is given by the formula

$$\begin{aligned} d\Gamma = |\mathcal{M}|^2 \cdot \frac{S}{2\hbar m_1} \cdot \left[\left(\frac{c \cdot d^3\vec{p}_2}{(2\pi)^3 2 \cdot E_2}\right)\left(\frac{c \cdot d^3\vec{p}_3}{(2\pi)^3 2 \cdot E_3}\right) \ldots \left(\frac{c \cdot d^3\vec{p}_n}{(2\pi)^3 2 \cdot E_n}\right)\right] \\ \times (2\pi)^4 \delta^4 (p_1 - p_2 - p_3 \ldots - p_n) \quad , \end{aligned} \tag{B.4}$$

where $p_i = (E_i/c, \vec{p}_i)$ is the four-momentum of the i-th particle. S is a product of statistical factors which is $(1/j!)$ for each group of "j" identical particles in the final state. The integration of B.4 over all outgoing momenta, gives the decay rate Γ.

B.1.1 Golden Rule for Scattering

We assume that the particles "1" and "2" collide and after that collision particles "3,4,...,n" are produced $(1+2 \rightarrow 3+4+\ldots+n)$. The cross section for a such reaction is given by

$$\begin{aligned} d\sigma = |\mathcal{M}|^2 \cdot \frac{\hbar^2 S}{4\sqrt{(p_1 \cdot p_2)^2 - (m_1 m_2 c^2)^2}} \\ \times \left[\left(\frac{c \cdot d^3\vec{p}_3}{(2\pi)^3 2 \cdot E_3}\right)\left(\frac{c \cdot d^3\vec{p}_4}{(2\pi)^3 2 \cdot E_4}\right) \ldots \left(\frac{c \cdot d^3\vec{p}_n}{(2\pi)^3 2 \cdot E_n}\right)\right] \\ \times (2\pi)^4 \delta^4 (p_1 + p_2 - p_3 - p_4 \ldots - p_n) \end{aligned} \tag{B.5}$$

In inclusive reactions like $(1+2 \rightarrow 3+X)$, the cross section is given by

$$\begin{aligned} d\sigma = |\mathcal{M}|^2 \cdot \frac{\hbar c S}{8\pi(E_1+E_2) \cdot |\vec{p}_1|} \\ \times \frac{\delta(E_1+E_2) - \sqrt{m_3^2 c + \vec{p}_3{}^2} - \sqrt{m_X^2 + \vec{p}_3{}^2}}{\sqrt{m_3^2 c^2 + \vec{p}_3{}^2}\sqrt{m_X^2 c^2 + \vec{p}_3{}^2}} \cdot d^3 p_3 \end{aligned} \tag{B.6}$$

$|\mathcal{M}|^2$ depends on the direction of $\vec{p}_3$ as well as on its magnitude. Therefore, it is not possible to carry out the angular integration. One can write

$$\mathrm{d}^3\vec{p}_3 = p_3^2 \mathrm{d}p_3 \mathrm{d}\Omega \quad \text{and} \quad \mathrm{d}\Omega = \sin\theta \mathrm{d}\theta \mathrm{d}\phi$$

When integrating B.6 over p_3 from $0 \rightarrow \infty$, one obtains

$$\frac{\mathrm{d}\sigma}{\mathrm{d}\Omega} = \left(\frac{\hbar c}{8\pi}\right)^2 \cdot \frac{S|\mathcal{M}|^2}{(E_1+E_2)^2} \cdot \frac{|\vec{p}_f|}{|\vec{p}_i|} \quad , \tag{B.7}$$

where $|\vec{p}_f|$ is the magnitude of the momentum of the outgoing particle "3" or "X" and $|\vec{p}_i|$ is the magnitude of incoming particle "1" or "2".

The invariant cross section $E \cdot \mathrm{d}^3\sigma/\mathrm{d}p^3$ can be writen as follows (since we have a cylindrical symmetry)

$$E \cdot \frac{\mathrm{d}^3\sigma}{\mathrm{d}p^3} = E \cdot \frac{\mathrm{d}^3\sigma}{2\pi p_t \mathrm{d}p_t \mathrm{d}p_z} \tag{B.8}$$

From formula B.1 one can obtain the identy

$$\frac{\mathrm{d}y}{\mathrm{d}p_z} = \frac{1}{E}$$

therfore,

$$E \cdot \frac{\mathrm{d}^3\sigma}{\mathrm{d}p^3} = \frac{1}{2\pi} \frac{\mathrm{d}^2\sigma}{p_t \mathrm{d}p_t \mathrm{d}y} \tag{B.9}$$

Bibliography

[1] Peter Braun-Munzinger and Johanna Stachel. Dynamics of ultra-relativistic nuclear collisions with heavy beams: An experimental overview. *Nucl. Phys.*, A638:3–18, 1998.

[2] Johanna Stachel. Towards the quark-gluon plasma. *Nucl. Phys.*, A654:119c–135c, 1999.

[3] A. Andronic, P. Braun-Munzinger, and J. Stachel. Hadron production in central nucleus-nucleus collisions at chemical freeze-out. *Nucl. Phys.*, A772:167–199, 2006.

[4] J. Pochodzalla et al. Probing the nuclear liquid-gas phase transition. *Phys. Rev. Lett.*, 75:1040–1043, 1995.

[5] M. Pichon et al. Bimodality: a possible experimental signature of the liquid-gas phase transition of nuclear matter. *Nucl. Phys.*, A779:267–296, 2006.

[6] R. F. Sawyer. Condensed π^- phase in neutron star matter. *Phys. Rev. Lett.*, 29:382–385, 1972.

[7] A. B. Migdal. Stability of vacuum and limiting fields. *Zh. Eksp. Teor. Fiz.*, 61:2209–2224, 1971.

[8] D. B. Kaplan and A. E. Nelson. Strange goings on in dense nucleonic matter. *Phys. Lett.*, B175:57–63, 1986.

[9] G. E. Brown and H. Bethe. A Scenario for a large number of low mass black holes in the galaxy. *Astrophys. J.*, 423:659, 1994.

[10] J.W. Harris and B. Müller. The search for the quark-gluon plasma. *Annu. Rev. Nucl. Part. Sci.*, 46:71–107, 1996.

[11] H. Stöcker and W. Greiner. High-energy heavy ion collisions-probing the equation of state of highly excited hadronic matter. *Phys. Rept.*, 137:277–392, 1986.

[12] F. Rami et al. Isospin-tracing: A probe of non-equilibrium in central heavy-ion collisions. *Phys. Rev. Lett.*, 84:1120–1123, 2000.

[13] J. P. Blaizot. Nuclear compressibilities. *Phys. Rept.*, 64:171, 1980.

[14] D. H. Youngblood, H. L. Clark, and Y.-W. Lui. Incompressibility of nuclear matter from the giant monopole resonance. *Phys. Rev. Lett.*, 82(4):691–694, 1999.

[15] W. Reisdorf and H. G. Ritter. Collective Flow in Heavy-Ion Collisions. *Annual Review of Nuclear and Particle Science*, 47:663–709, 1997.

[16] N. Herrmann, J. P. Wessels, and T. Wienold. Collective Flow in Heavy-Ion Collisions. *Annual Review of Nuclear and Particle Science*, 49:581–632, 1999.

[17] Pawel Danielewicz, Roy Lacey, and William G. Lynch. Determination of the Equation of State of Dense Matter. *Science*, 298(5598):1592–1596, 2002.

[18] A. Andronic et al. Excitation function of elliptic flow in Au + Au collisions and the nuclear matter equation of state. *Phys. Lett.*, B612:173–180, 2005.

[19] T. Gaitanos, C. Fuchs, and H. H. Wolter. Asymmetric colliding nuclear matter approach in heavy ion collisions. *Nucl. Phys.*, A741:287–304, 2004.

[20] S. Schnetzer et al. Production of K^+ mesons in 2.1-GeV/nucleon nuclear collisions. *Phys. Rev. Lett.*, 49:989–992, 1982.

[21] S. Nagamiya. Role of mean free paths of product particles in high-energy nucleus-nucleus collisions. *Phys. Rev. Lett.*, 49:1383–1386, 1982.

[22] S. Nagamiya, J. Randrup, and T. J. M. Symons. Nuclear collisions at high-energies. *Ann. Rev. Nucl. Part. Sci.*, 34:155–187, 1984.

[23] J. Aichelin and C. M. Ko. Subthreshold kaon production as a probe of the nuclear equation of state. *Phys. Rev. Lett.*, 55:2661–2663, 1985.

[24] C. Sturm et al. Evidence for a soft nuclear equation of state from kaon production in heavy ion collisions. *Phys. Rev. Lett.*, 86:39–42, 2001.

[25] C. Fuchs, Amand Faessler, E. Zabrodin, and Yu-Ming Zheng. Probing the nuclear equation of state by K^+ production in heavy-ion collisions. *Phys. Rev. Lett.*, 86:1974–1977, 2001.

[26] W. Weise. Nuclear aspects of chiral symmetry. *Nucl. Phys.*, A553:59c–72c, 1993.

[27] C. Adami and G. E. Brown. Matter under extreme conditions. *Phys. Rept.*, 234:1–71, 1993.

[28] Michael C. Birse. Chiral symmetry in nuclei: Partial restoration and its consequences. *J. Phys.*, G20:1537–1576, 1994.

[29] Charles Alcock, Edward Farhi, and Angela Olinto. Strange stars. *Astrophys. J.*, 310:261–272, 1986.

[30] Kohsuke Yagi, Tetsuo Hatsuda, and Yasuo Miake. *Quark-Gluon Plasma*. Cambridge University Press, 2005.

[31] W. Weise. Hadrons in dense baryonic matter. *Nucl. Phys.*, A610:35c–48c, 1996.

[32] J. Gasser and H. Leutwyler. Quark masses. *Phys. Rept.*, 87:77–169, 1982.

[33] W. Weise. Hadrons in dense matter. *Nucl. Phys.*, A574:347c–363c, 1994.

[34] Che. Ming Ko et al. Properties of hadrons in the nuclear medium. *Annual Review of Nuclear and Particle Science*, 47(1):505–539, 1997.

[35] E. Shuryak and T Schafer. The QCD vacuum as an instanton liquid. *Annual Review of Nuclear and Particle Science*, 47(1):359–394, 1997.

[36] Murray Gell-Mann, R. J. Oakes, and B. Renner. Behavior of current divergences under SU(3) x SU(3). *Phys. Rev.*, 175:2195–2199, 1968.

[37] Barry R. Holstein. How large is f_π? *Phys. Lett.*, B244:83–87, 1990.

[38] Wolfram Weise. Chiral dynamics in nuclear systems. *Prog. Theor. Phys. Suppl.*, 149:1–19, 2003.

[39] Vesteinn Thorsson and Andreas Wirzba. S wave meson nucleon interactions and the meson mass in nuclear matter from chiral effective lagrangians. *Nucl. Phys.*, A589:633–648, 1995.

[40] K. Suzuki et al. Precision spectroscopy of pionic 1s states of sn nuclei and evidence for partial restoration of chiral symmetry in the nuclear medium. *Phys. Rev. Lett.*, 92:072302, 2004.

[41] X. S. Fang, C. M. Ko, Guo-Qiang Li, and Y. M. Zheng. The relativistic transport model description of subthreshold kaon production in heavy ion collisions. *Nucl. Phys.*, A575:766–790, 1994.

[42] M. Mang. *Produktion von K-Mesonen in Au+ Au Stössen bei 1 GeV/Nukleon*. PhD thesis, Johann Wolfgang Goethe-Universität Frankfurt/Main (D), 1997.

[43] Peter Senger. Strange mesons in dense nuclear matter. *Nucl. Phys.*, A685:312c–317c, 2001.

[44] R. Barth et al. Subthreshold production of kaons and anti-kaons in nucleus-nucleus collisions at equivalent beam energies. *Phys. Rev. Lett.*, 78:4007–4010, 1997.

[45] F. Laue et al. Medium effects in kaon and antikaon production in nuclear collisions at subthreshold beam energies. *Phys. Rev. Lett.*, 82:1640–1643, 1999.

[46] E. L. Bratkovskaya, W. Cassing, and U. Mosel. Analysis of kaon production at sis energies. *Nucl. Phys.*, A622:593–604, 1997.

[47] A. Sibirtsev. Internal nuclear momentum and subthreshold kaon production. *Phys. Lett.*, B359:29–32, 1995.

[48] C. Hartnack, H. Oeschler, and J. Aichelin. What determines the K^- multiplicity at energies around 1-AGeV to 2-AGeV? *Phys. Rev. Lett.*, 90:102302, 2003.

[49] Guo-Qiang Li, C. M. Ko, and Bao-An Li. Kaon flow as a probe of the kaon potential in nuclear medium. *Phys. Rev. Lett.*, 74:235–238, 1995.

[50] P. Crochet et al. Sideward flow of K^+ mesons in Ru + Ru and Ni + Ni reactions near threshold. *Phys. Lett.*, B486:6–12, 2000.

[51] Philippe Crochet. Etude des collisions d'ions lourds aux nergies du SIS et du LHC (these d'habilitation), 2005.

[52] W. Cassing and E.L. Bratkovskaya. Hadronic and electromagnetic probes of hot and dense nuclear matter. *Phys. Rept.*, 308:65–233, 1999.

[53] Y. Shin et al. Enhanced out-of-plane emission of K^+ mesons observed in Au+Au collisions at 1-AGeV. *Phys. Rev. Lett.*, 81:1576–1579, 1998.

[54] Guo-Qiang Li, C. M. Ko, and G. E. Brown. Kaon azimuthal distributions in heavy ion collisions. *Phys. Lett.*, B381:17–22, 1996.

[55] V. P. Koptev et al. Subthreshold K^+-meson production in protons-nucleus interactions. *Sov. Phys. JETP*, 67:2177–2184, 1988.

[56] N. A. Tarasov, V. P. Koptev, and M. M. Nesterov. Cascade mechanism for subthreshold production of K^+ mesons in proton nucleus interactions. *JETP Lett.*, 43:274–277, 1986.

[57] W. Cassing et al. Subthreshold K^+ production in proton nucleus reactions. *Phys. Lett.*, B238:25–30, 1990.

[58] A. A. Sibirtsev and Markus Buescher. Subthreshold K^+ production in proton-nucleus collisions. *Z. Phys.*, A347:191–202, 1994.

[59] M. Debowski et al. Subthreshold K^+ production in proton nucleus collisions. *Z. Phys.*, A356:313–325, 1996.

[60] V. Koptev et al. Forward K^+ production in subthreshold pa collisions at 1.0-gev. *Phys. Rev. Lett.*, 87:022301, 2001.

[61] E. Ya. Paryev. Subthreshold and near threshold K^+ meson production on light nuclei by protons. *Eur. Phys. J.*, A5:307–319, 1999.

[62] M. Nekipelov et al. Evidence of kaon nuclear and coulomb potential effects on soft K^+ production from nuclei. *Phys. Lett.*, B540:207–212, 2002.

[63] Z. Rudy, W. Cassing, L. Jarczyk, B. Kamys, and P. Kulessa. K^+ production in proton-nucleus reactions and the role of momentum-dependent potentials. *Eur. Phys. J.*, A15:303–314, 2002.

[64] E. Ferrari. Associated production in proton-proton collisions. *Phys. Rev.*, 120(3):988–992, 1960.

[65] Tsu Yao. Strange particle production in proton-proton collisions. *Phys. Rev.*, 125(3):1048–1054, 1962.

[66] K. Tsushima, S. W. Huang, and Amand Faessler. The role of the $\Delta(1929)$ resonance for kaon production in heavy ion collisions. *Phys. Lett.*, B337:245–253, 1994.

[67] K. Tsushima, A. Sibirtsev, and Anthony W. Thomas. Strangeness production from πN collisions in nuclear matter. *Phys. Rev.*, C62:064904, 2000.

[68] P. A. M. Guichon. A possible quark mechanism for the saturation of nuclear matter. *Phys. Lett.*, B200:235, 1988.

[69] K. Tsushima, A. Sibirtsev, and Anthony W. Thomas. Resonance model study of strangeness production in p p collisions. *Phys. Lett.*, B390:29–35, 1997.

[70] Pierre A. M. Guichon, Koichi Saito, Evgenii N. Rodionov, and Anthony W. Thomas. The role of nucleon structure in finite nuclei. *Nucl. Phys.*, A601:349–379, 1996.

[71] K. Saito, K. Tsushima, Ding-Hui Lu, and Anthony W. Thomas. Omega nucleus bound states in the Walecka model. *Phys. Rev.*, C59:1203–1206, 1999.

[72] A. Sibirtsev, K. Tsushima, W. Cassing, and Anthony W. Thomas. The role of the P(11)(1710) in the $NN \to N\Sigma K$ reaction. *Nucl. Phys.*, A646:427–443, 1999.

[73] A. Baldini, V. Flaminio, W.G. Moorhead, and D.R.O. Morrison. *Total Cross-Sections for Reactions of High Energy Particles*. Springer-Verlag, Berlin,., 1988.

[74] A. Gobbi et al. A highly segmented ΔE-time-of-flight wall as forward detector of the 4π-system for charged particles at the SIS/ESR accelerator. *Nucl. Instrum. Meth.*, A324:156–176, 1993.

[75] J. Ritman. The FOPI Detector at SIS/GSI. *Nucl. Phys. Proc. Suppl.*, 44:708–715, 1995.

[76] D. Pelte et al. Charged pions from Ni on Ni collisions between 1 AGeV and 2 AGeV. *Z. Phys.*, A359:55–65, 1997.

[77] D. Best et al. K^+ production in the reaction ^{58}Ni+^{58}Ni at incident energies from 1 AGeV to 2 AGeV. *Nucl. Phys.*, A625:307–324, 1997.

[78] D. Pelte et al. Charged pion production in Au on Au collisions at 1 AGeV. *Z. Phys.*, A357:215–234, 1997.

[79] J. L. Ritman et al. On the transverse momentum distribution of strange hadrons produced in relativistic heavy ion collisions. *Z. Phys.*, A352:355–357, 1995.

[80] Philippe Crochet. *Effets collectifs dans les collisions semi-central Au(100-800 AMeV)+Au*. PhD thesis, Universite de Luis Pasteur de Strasbourg, 1996.

[81] M. Eskef et al. Identification of baryon resonances in central heavy-ion collisions at energies between 1AGeV and 2 AGeV. *Eur. Phys. J.*, A3:335–349, 1998.

[82] N. Herrmann. Particle production and flow at SIS energies. *Nucl. Phys.*, A610:49c–62c, 1996.

[83] Ralf Kutsche. *Untersuchungen der In-Medium-Eigenschaften von K^0_S-Mesonen und Λ-Hyperonen an der Produktionsschwelle*. PhD thesis, Technische Universität Darmstadt, 2000.

[84] A. Mangiarotti et al. Sub-threshold Phi-meson yield in central ^{58}Ni+^{58}Ni collisions. *Nucl. Phys.*, A714:89–123, 2003.

[85] Markus Merschmeyer. *Production and Flow of neutral strange particles in Ni+Ni at 1.93 AGeV*. PhD thesis, Universität Heidelberg, 2004.

[86] Xavier Lopez. *Production d'étrangeté dans les collisions Ni+Ni a 1.93 AGeV*. PhD thesis, L.P.C. Clermont-Ferrand, 2004.

[87] R. S. Simon et al. Secondary pion beams at GSI. *Prog. Part. Nucl. Phys.*, 42:247–256, 1999.

[88] J. Diaz et al. Design and commissioning of the GSI pion beam. *Nucl. Instrum. Meth.*, A478:511–526, 2002.

[89] B. W. Allardyce et al. Pion reaction cross-sections and nuclear sizes. *Nucl. Phys.*, A209:1–51, 1973.

[90] W. Bartel et al. Experimental study of jets in electron - positron annihilation. *Phys. Lett.*, B101:129, 1981.

[91] H. Drumm et al. Experience with the jet chamber of the jade detector at petra. (talk). *Nucl. Instrum. Meth.*, 176:333–344, 1980.

[92] H. M. Fischer et al. The opal jet chamber full scale prototype. *Nucl. Instrum. Meth.*, A252:331–342, 1986.

[93] H. M. Fischer et al. The opal jet chamber. *Nucl. Instrum. Meth.*, A283:492–501, 1989.

[94] A. Breskin et al. Further results on the operation of high accuracy drift chambers. *Nucl. Instr. Meth.*, 119:9, 1974.

[95] G. Goebels. *Untersuchung der Bose-Einstein-Korrelationen geladener Pionen in relativistischen Schwerionenkollisionen der Systeme Au+Au und Ni+Ni im Energiebereich von 1 AGeV bis 2 AGeV*. PhD thesis, Universität Heidelberg, 1995.

[96] Christopher H. Pinkenburg. *Flußeffekte geladener Pionen im System Au+Au bei $E_p = 1$ AGeV*. PhD thesis, Universität Heidelberg, 1995.

[97] H. Foeth et al. On the localization of the position of the particle along the wire of a Multiwire Proportional Chamber. *Nucl. Instr. Meth.*, 109:521, 1973.

[98] Claus Grupen. *Particle Detectors*. Cambridge University Press, 1996.

[99] Christof Plettner. *Strangenesspoduktion bei kleinen transversalen Impulsen und mittleren Rapiditäten in der Reaktion $^{96}Ru+^{96}Ru$ @ 1.69 A.GeV*. PhD thesis, Technische Universität Dresden, 1999.

[100] W.R. Leo. *Techniques for Nuclear and Particle Physics Experiments*. Springer-Verlag, 1987.

[101] B. Hyams et al. A silicon counter telescope to study shortlived particles in high-energy hadronic interactions. *Nucl. Instr. Meth.*, 205:99, 1983.

[102] G. D Rochester and C.C Butler. Evidence for the existence of new unstable elementary particles. *Nature*, 160:855, 1947.

[103] D. Drijard, H.G. Fischer, and T. Nakada. Study of event mixing and its application to the extraction of resonance signals. *Nucl. Instrum. Meth.*, 225:367–377, 1984.

[104] D. LHôte. About resonance signal extraction from multiparticle data: Combinatorics and event-mixing methods. *Nucl. Instrum. Meth.*, A337:544–556, 1994.

[105] A. Andronic et al. Proposal: Measurement of strange baryons and kaonic nuclear clusters with FOPI. 2004.

[106] GEANT Team. *GEANT - Detector Description and Simulation Tool*. CERN, http://consult.cern.ch/writeup/geant, 1995.

[107] Astrid Chantelauze. Investigations on the central drift chamber of the fopi experiment at gsi (master recherche physique), June, 2005.

[108] R.L. Glueckstern. Uncertainties in track momentum and direction due to multiple scattering and measurement errors. *Nucl. Instr. Meth.*, 24:381, 1963.

[109] J. Aichelin. "Quantum" Molecular Dynamics – A dynamical microscopic *n*-Body Approach to investigate Fragment Formation and the nuclear Equation of State in Heavy-Ion Collisions. *Phys. Rept.*, 202:233–360, 1991.

[110] C. Hartnack et al. Modelling the many-body dynamics of heavy-ion collisions: Present status and future perspective. *Eur. Phys. J.*, A1:151–169, 1998.

[111] B. Povh, S. Rith, C. Scholz, and F. Zetsche. *Particles and Nuclei:an introduction to physical concepts*. Springer-Verlag, 2003.

[112] Markus Buescher et al. Inclusive K^+ meson production in proton nucleus interactions. *Eur. Phys. J.*, A22:301–317, 2004.

[113] D.E. Groom et al. Particle Data Group, Review of Particle Physics. *Eur. Phys. J*, C15:1, 2000.

[114] H.A. Bethe. Theorie des Durchgangs schneller Korpuskularstrahlen durch Materie. *Ann. d. Phys*, 5:325, 1930.

[115] F. Bloch. Bremsvermögen von Atomen mit mehreren Elektronen. *Z. Phys*, 81:363, 1933.

[116] E.A. Uehling. Penetration of Heavy Charged Particles in Matter. *Ann. Rev. Nucl. Part. Sci*, 4:315, 1954.

[117] David Griffiths. *Introduction to elementary particles*. John Wiley and Sons, Inc., 1987.

Acknowledgments

First, I express my gratitude to Prof. Dr. Norbert Herrmann for giving me the chance to work with the FOPI collaboration, for his support and for fruitful discussions.

I want to thank Prof. Dr. Johanna Stachel for accepting to be a second referee of this thesis.

I would like to thank Prof. Dr. Matthias Bartelmann and Prof. Dr. Hans Jürgner Pirner to accept to be a member of the examination committee.

I am grateful to Dr. Elena Bratkovskaya and Dr. Christoph Hartnack for providing their transport model codes. I would like to thank Dr. Yvonne Leifels for running these codes and providing results presented in this work.

I wish to thank cordially all FOPI members, especially Dr. Joszef Kecskemeti, Dr. Milorad Karolija and Dr. Krzyzstof Wisniewski for the exchange of ideas.

I want to thank: all my colleagues in the KP group Heidelberg, people with whom I shared and still share the office, Everard Cordier, Dr. Alessio Mangiarotti with whom I have fruitful discussions, Dr. Markus Merschmeyer not only for the pleasant working atmosphere but in particular for proof-reading the manuscript carefully and the constructive discussions. I wish to thank Korinna Zapp for her help in the corrections of the manuscript.

Je tiens a remercier mon oncle El Hadi pour son soutien moral. Merci a vous freres et soeurs, pour etre toujours la quand j'avais besoins de votre aide. Merci Amina d'etre patiente durant cette periode.

Enfin, merci mes chers parents pour vos sacrifices et pour le constant soutien materiel et moral.